



DEMOCRITOS
DEmocritos MOdeling Center for
Research In aTOMistic Simulation **INFN**

Computer Simulation of Thermally Activated Processes

Theory, Algorithms, and a Few Case Applications to
Surface Chemistry

Thesis submitted for the degree of
“Doctor Philosophiæ”

Candidate
Carlo Sbraccia

Supervisors
Prof. Stefano Baroni
Dr. Pier Luigi Silvestrelli

February 2005

Ai miei genitori

Contents

Introduction	v
1 Thermally activated processes	1
1.1 Transition-State Theory	4
1.2 Transition probability from the Langevin equation	9
2 Numerical methods	13
2.1 The Nudged Elastic Band method	15
2.1.1 Variable-elastic-constants NEB	17
2.1.2 Climbing Image NEB	18
2.1.3 Improved tangent estimate	19
2.2 The String Method	20
2.2.1 Fourier representation	21
2.3 Quick-min optimisation scheme	24
2.4 Implementation	26
3 Acetylene chemisorption on Si(111)-(7×7)	29
3.1 Theoretical model	31
3.2 Semi-empirical calculations: chemisorption sites of C ₂ H ₂ on Si(111)-(7×7)	33
3.3 Ab initio calculations: chemisorption sites of C ₂ H ₂ on Si(111)- (2×2)	37
3.4 Reaction pathways and energy barriers	42
4 Deconstruction kinetics of the Rh(110)-1×2 missing row sur- face	45
4.1 Properties of the Rh(110) and Rh(110)-1×2 surfaces	46
4.2 Lattice-gas Hamiltonian	48
4.3 Deconstruction process	50

5	Early stages of graphitisation of the Ni(111) surface	57
5.1	Nickel (111) surface	59
5.2	Carbon adsorption: the carbidic phase	59
5.3	Graphene nucleation: the graphitic phase	64
5.4	Perspectives	66
6	Overview of other works from the author	71
7	Conclusions	75
A	Computational tools	79
B	Discrete Fourier Transform	83
	Bibliography	86
	Acknowledgements	91

Introduction

Perhaps the most useful mental construction in all the physical chemistry is the representation of the atomic dynamics, the complex simultaneous motion of several atoms that compose the system, by the rolling or the sliding of a single particle on a many-dimensional surface. This concept is brought to life through our everyday experience with gravitational potential energy. Words and phrases such as hills, valleys, mountain passes and plateaus are pervasive in discussions involving potential energy surfaces. Many important dynamical concepts can be illustrated, or at least can be imagined, using the two dimensions of the gravitational potential energy construct.

M. L. McKee and M. Page

The study of the chemical reactions that occur at the surfaces of semiconductors and transition metals is a topic of extraordinary importance because of the technological relevance that such reactions have, and will continue to have, for our society. Processes such as epitaxy, chemical vapour deposition, etching, oxidation, passivation, which are used routinely in the industry, involve chemical and physical phenomena occurring at the surface of the semiconductor wafers. The growth of thin films of silicon carbide (SiC) under controlled conditions represents an example of an industrial process that would take advantage from a deeper insight on surface phenomena. Indeed, defect-free single crystals of SiC cannot be produced with the traditional techniques used for silicon because the low solubility of carbon in silicon favours the precipitation of graphitic crystals. Epitaxial growth is the only technique presently available for producing samples of SiC suitable for electronic applications. On the basis of the observation that the solubility of carbon at the silicon surface is many orders of magnitude higher than in the bulk, it is possible to produce thin films of SiC with a limited amount of defects by the controlled deposition of organic molecules. A deeper understanding of such processes will lead to a reduction of the production costs and to an increase of the quality of the SiC produced.

Another field in which surface phenomena are of key importance is that of the heterogeneous catalysis. Many industrial chemical processes as, for instance, the synthesis of ammonia, would not be possible in the absence of solid state catalysts that increase by orders of magnitude the rate of the chemical reactions involved. The efficiency and the selectivity of the production process strongly depends on the specific properties of the catalyst. In many cases the catalyst consists of transition-metal nanoparticles deposited on metal-oxides and the reactions occur at the surfaces of these nanoparticles. It is clear that a deeper understanding of the interactions between the reactants and transition-metal surfaces would allow for the optimisation of the industrial production of many chemicals. For instance, the possibility of tuning the relative reaction rates of the different steps of methane dehydrogenation would permit a more efficient design of important chemical processes such as the production of hydrogen from methane or the conversion of the latter to methanol.

The progresses achieved in the last twenty years in the field of computer modelling of matter at the nanoscale have opened new ways of investigating chemical reactions with atomic resolution, realising what can be considered a *virtual laboratory*. Of particular importance has been the introduction of density functional theory (DFT) for the description of the electronic structure of matter. Within this framework it is now possible to use quantum mechanics for studying the properties of systems composed by tens, hundreds and even thousands of atoms, achieving a reliable description of the inter-atomic interactions. Studies based on this method are generally referred to as *first-principles calculations*. Ideally, in the virtual laboratory one would like to simulate, step by step, the time evolution of the chemical reaction tuning, for instance, the system's temperature and pressure. This has started to become possible since the seminal work of Car and Parrinello in 1985 [1], who have combined the predictive power of first-principles calculations based on DFT with the possibility of following the time evolution of the system using the molecular dynamics technique. First-principles molecular dynamics has been employed in the years to investigate the kinetics and the equilibrium properties of a number of different systems, gaining insight into phenomena that occur on time scales comparable with the characteristic time scale of the microscopic dynamics (some picoseconds). This is the situation whenever the relevant kinetics is determined by energy barriers that are low compared to the typical thermal fluctuations. When this is not the case the system spends most of its time within stable states, so that interesting transitions occur only rarely.

Since the work of Van't-Hoff and Arrhenius in the late nineteenth century, it is known that the probability of overcoming an energy barrier becomes ex-

ponentially small by reducing the temperature of the system. Indicating with τ_{fast} the time scale appropriate for the microscopic dynamics, the transition between the stable states occurs on a time scale which is approximatively given by $\tau_{slow} \sim \tau_{fast} e^{\frac{E_A}{k_B T}}$, where E_A indicates the barrier height. It is clear that, as soon as the temperature is reduced below E_A , the transition becomes a *rare event* and the process can no longer be studied within the molecular dynamics framework. This because the time scales involved can easily become several orders of magnitude longer than those that can be afforded in a molecular dynamics simulation. This sets a fundamental limitation to the kind of processes that can be studied within molecular dynamics because, however fast our computers might be, there will always be interesting phenomena occurring on time scales inaccessible to it.

For this reason the development of computational methods suited for studying complex systems whose dynamics is driven by rare events has become the subject of intense research. The study of these phenomena is, in many cases, based on the identification of the *transition state*, the configuration that represents the bottleneck for the reaction. In the simplest approximation the transition state can be identified with the saddle point that separates the two minima corresponding to the stable states. The potential energy at the saddle point gives the energy barrier that has to be overcome, and the transition rate can be estimated using the harmonic transition-state theory (TST). This approach is justified for those systems in which the potential energy surface (PES) describing the inter-atomic interactions is smooth and for temperatures low enough to allow for the description of entropic effects within the harmonic approximation. In these systems most of the information on the transition is obtained from saddle points. Unfortunately, saddle points are much more difficult to locate than minima because the methods based only on the first derivatives of the PES (the forces) do not converge to unstable stationary points. The access to the second derivatives of the PES (the Hessian matrix) would permit the use of the Newton-Raphson algorithm which is locally convergent to stationary points, saddles included. However, this method is rather cumbersome and the evaluation of second derivatives makes it unsuited to be used in first-principles calculations. Elber and Karplus [2] have suggested an innovative approach. Rather than starting from the initial state and looking for a transition state, they consider a path that connects the initial and the final states. The method is appealing since it focuses on the global character of the path rather than on local properties of the PES. The nudged elastic band method (NEB) [3] and the recently proposed string method [4] constitute a refinement of this approach, in which the minimum energy path (MEP) that connects the stable

states is identified. The MEP is a path in the configuration space defined by the property that the components of the forces orthogonal to it are zero. This implies that the MEP's tangent is everywhere parallel to the force vector; as a consequence, the MEP crosses the saddle point which is easily identified as the configuration of highest energy along this path. Moreover, it can be shown that, within the framework of a stochastic description of the systems' dynamics, the MEP is, in the low temperature limit, the most probable path that connects two minima of the PES. The MEP can thus be used to define a reaction coordinate for the transition between two stable states. Once a reliable reaction coordinate is available, the transition rate can be obtained by computing the free-energy profile by using standard thermodynamics integration [5]. This approach is more accurate than the one based on the harmonic approximation described above and permits good estimates also when the kinetics is dominated by entropic effects.

In a complex system the potential energy surface can be very rugged and exhibit many stationary points. In such a case there exists a multitude of MEPs connecting the stable states and the very concept of transition state as a saddle point in the PES is called into question. Chandler and collaborators [6] have proposed a method for statistically sampling all the dynamical paths that take the system from one stable state to the other. This method is a significant step towards the study of rare events in complex systems, as it does not require the assumption of transition state theory nor even the existence of a single well defined transition state. Its only prerequisite is the knowledge of at least one reactive dynamical trajectory. However, determining the initial trajectory is often difficult. A general, but computationally demanding, strategy suggested by Chandler and collaborators consists in performing a simulated annealing in the space of the reactive trajectories. Alternatively, Passerone and Parrinello [7] have proposed a method to identify the dynamical trajectory that connects two preassigned configurations, based on the Hamilton's least-action principle.

All the methods presented here require the knowledge of the initial and final states of the reaction. This makes the problem simpler because one has to consider, among all the possible trajectories, only those that connect the two stable states. Recently, Laio and Parrinello [8] have formulated a novel coarse-grained molecular dynamics approach (called by them metadynamics) to explore the free-energy surface (FES). This method, inspired by earlier work by Gear, Kevrekidis, and Theodoropoulos [9], uses a conveniently defined fictitious dynamics in a coarse-grained space of reduced dimensionality to bias the microscopic dynamics of the system so that it can escape from free-energy minima. Because of the bias, dynamical information is lost, but a quantitative determination of the FES is obtained as a valuable by-product

of the simulation. The coarse-grained dynamics involves few collective coordinates that control transitions among different basins on the FES. There is no general recipe for choosing the order parameters: they are problem dependent and not unique. Reasonable choices are based on chemical/physical intuition.

In this thesis I shall focus on the study of thermally activated processes that occur on the surfaces of semiconductors and transition metals. The PES of these systems is rather smooth and characterised by a small number of relevant minima and saddle points. As explained before, in this situation the MEP is a good indicator of the reaction mechanism and the transition rate can be estimated using transition-state theory. The entropic contribution to the transition rate is taken into account through the harmonic approximation. The NEB method and the recently proposed string method probably represent the best choice for a first-principles calculation of the reaction mechanism because their computational cost is only few times larger than that of standard structural optimisations. I have developed one of the first implementations of the NEB and of the string methods within the framework of first-principles calculations and I have used them for the study of surface processes.

The thesis is organised as follows. In the first chapter I present the difficulties that are encountered in the study of thermally activated processes, which are characterised by multiple time scales. I describe the limits of molecular dynamics simulations in the study of such events and outline some alternative theoretical approaches. In the second chapter I describe two techniques, the nudged elastic band method (H. Jónsson, G. Mills, K. W. Jacobsen, G. Henkelman and B. P. Uberuaga [3, 10, 11]) and the string method (W. E, W. Ren and E. Vanden-Eijnden [4]), that are currently used to identify the MEP connecting stable states of the potential energy surface. I also describe some extensions to these approaches that I have developed with the aim of improving their performance and usability. In the third chapter I present a first application of the techniques described in chapter 2. The problem considered here is the study of the interaction of acetylene with the Si(111)-(7×7) surface; a traditional *ab initio* investigation of the many possible chemisorption configurations is supplemented by the identification of low energy reaction pathways leading to such structures. In the fourth chapter I present the results of the study of the deconstruction process' dynamics of the Rh(110)-1×2 missing row surface. This work was motivated by a collaboration with an experimental group working at ELETTRA (Trieste). In the fifth chapter I present some preliminary results of the study of the adsorption and diffusion of carbon atoms and small clusters on the Ni(111) surface. This work is still in progress. In the sixth chapter I present a short description of all the other

works, that I have contributed, in which the various implementations of the NEB method presented in Chapter 2 have been used.

Chapter 1

Thermally activated processes

In this chapter I present the peculiarities of thermally activated processes which, being characterised by multiple time scales, represent a challenging problem for the computational physics. I describe the limits of molecular dynamics simulations in the study of such events and outline some alternative theoretical approaches.

Let's consider a system of N atoms, whose generalised coordinates are indicated by q^{3N} . The potential energy surface (hereafter indicated as PES or $V(q^{3N})$) is the function that describes how the potential energy changes as the nuclei move relative to one another. In classical mechanics the PES determines the structure, the dynamics, and the thermodynamics of any system:¹

- stable configurations occur at the minima of V , defining the possible structures of the system;
- the gradient of V gives (the negative of) the forces acting on the system, which determine the equations of motion;
- the partition function, \mathcal{Z} , which determines the thermodynamics, is also a functional of V .

The dynamics of any system described by the Newton's equations of motion can be visualised as the exploration of this potential-energy landscape. One of the basic assumptions of classical statistical mechanics is that the time

¹Analogous statements can be made in quantum mechanics within the Born-Oppenheimer approximation, where the potential energy surface is the solution of the Schrödinger equation at frozen nuclear positions.

spent in the neighbourhood of any point of the configuration space q^{3N} is proportional to the Boltzmann factor $e^{-\frac{V(q^{3N})}{k_B T}}$. This implies that the system preferentially stays nearby the minima of the PES, but thermal fluctuations allow it to explore also configuration of higher energy.

Since the seminal paper of Alder and Wainwright in 1957, molecular dynamics (MD) simulations have been fruitfully used to explore the potential energy surface of classical many-body systems, thus probing their time evolution and equilibrium properties in the most direct way. Nowadays, the time scale accessible to this approach ranges between 10^{-13} and 10^{-8} seconds, depending on the system size and on the approach used to compute the forces acting on the atoms. This time window is adequate to study many structural and dynamical properties, provided that the relevant fluctuations decay on a time scale that is appreciably shorter than the longest simulation we can afford. The maximum length of a molecular dynamics simulation is limited by the computational power at our disposal and by the time step used to integrate numerically the equations of motion. The former limit is, day after day, pushed forward and, on the basis of the Moore law,² the computational power is expected to increase by a factor two every 18 months, so that the length of MD simulations can increase of the same factor. On the contrary, the latter limit is dictated by the physics of the system under study. Indeed, an accurate integration of the equation of motion must be able to follow the fastest frequency that characterises the system. Since typical vibrational frequencies are in the order of tens of terahertz, the time step must be chosen in the range of femtoseconds (10^{-15} sec). It is thus clear that, however large the computational power at our disposal might be, interesting problems in which the relevant time scales are longer than the longest simulation we can afford there will also be.³

Molecular dynamics is unsuited to describe the time evolution of systems that present multiple time scales, where important fluctuations decay slowly. To understand what the nature of this problem is and why MD simulations are not suited to study systems that exhibit such a behaviour, I consider here a system of particles of mass m that move on the potential

²Gordon Moore made his famous observation in 1965, just four years after the first planar integrated circuit was discovered. The press called it "Moore's Law" and the name has stuck. In his original paper, Moore observed an exponential growth in the number of transistors per integrated circuit and predicted that this trend would continue.

³For instance, our everyday experience indicates that chemical reactions of biological interest span the full range of time scales going from those that occur in few picoseconds to protein folding that can require several milliseconds. In all these cases the time step is dictated by the microscopic dynamics, so that the number of MD steps required to study these processes can be order of magnitudes larger than we can afford.

energy surface described in Figure 1.1. This PES is characterised by two minima, which represent the stable configurations and are hereafter referred as *reactants* and *products*, separated by an energy barrier whose height (as seen from the reactants side) is indicated by E_A . The time evolution of this system is characterised by oscillations around the two minima with typical frequencies determined by the curvature of the PES. The time scale of this process is approximatively given by $\tau_{fast} \sim \sqrt{\frac{m}{V''(q_{min})}}$, and it is independent from temperature. The system can also jump from a minimum to the other, overcoming the saddle point that separates reactants and products (indicated as *transition state* in Figure 1.1). The time scale characteristic of these jumps (τ_{slow}) depend on the ratio between the probability of being at the transition state and that of being in one of the two minima (for instance in the reactants' configuration). In contrast to τ_{fast} , τ_{slow} strongly depends on temperature, being approximatively given by $\tau_{slow} \sim \tau_{fast} e^{\frac{E_A}{K_B T}}$. This implies that, when $E_A \gg K_B T$, the time scales corresponding to vibrations and jumps are exponentially separated; by rising the temperature, the difference between τ_{slow} and τ_{fast} becomes smaller and smaller. The transition from

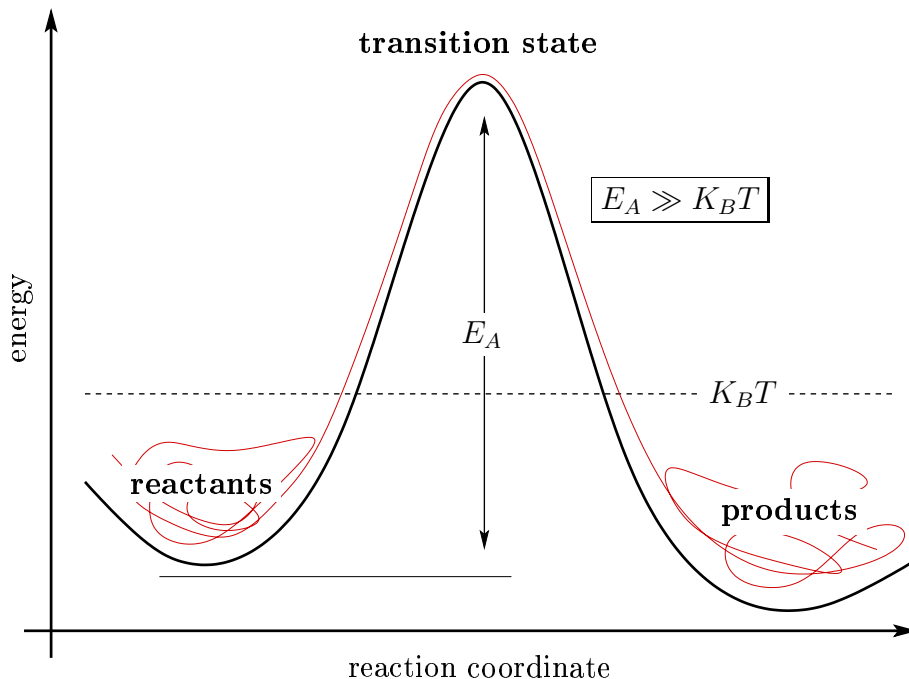


Figure 1.1: One dimensional cartoon of a thermally activated process: when the thermal energy is much lower than the energy barrier separating reactants and products, the system spends most of the time around the two minima and the transition is a rare event.

reactants to products (and vice versa) is therefore macroscopically perceived as a process that becomes exponentially slow as the temperature is lowered. The reason for this behaviour is not that the microscopic dynamics is slow, but that it is determined by a process (the barrier overcoming) that is a rare event. This is schematised in Figure 1.2, where the position of the system is depicted as a function of time. It is clear that the appropriate fluctuation is unlikely but, once it occurs, the transition proceeds quite quickly, on a time scale comparable with τ_{fast} . These phenomena are generally referred to as

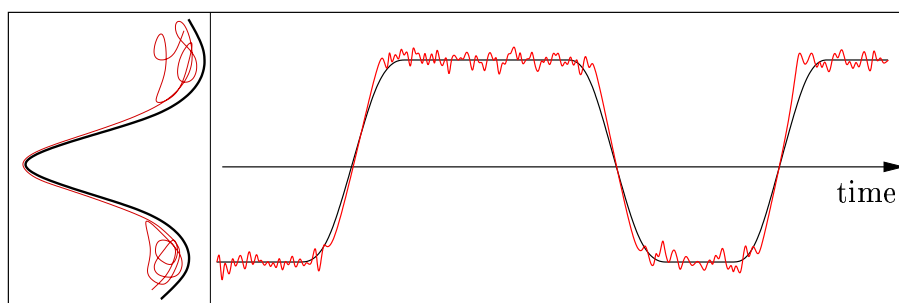


Figure 1.2: Time evolution of the system depicted in Figure 1.1.

thermally activated processes.

In the following I shall show that is possible to overcome the limitations of molecular dynamics by adopting an approach which provides directly the transition rate of the reaction.

1.1 Transition-State Theory

The fact that activated processes are rare events makes it possible to obtain accurate estimates of transition rates using a purely statistical approach, the *transition-state theory* (TST).

Again I focus on the bistable PES described in Figure 1.1 and I consider an ensemble of systems initially prepared in the reactants state. Each one of these systems can overcome the energy barrier and reach the products state so that the reaction can be schematised as:



I indicate with N_R and N_P the populations of the two end states. Since the transitions from one state to the other are infrequent, it can be assumed that they are decorrelated so that the two populations evolve following first-order

differential equations. As the global population $N_R + N_P$ is constant, the evolution of N_R and N_P is given by the following kinetic equations:

$$\dot{N}_R = -k^+ N_R + k^- N_P \quad (1.1)$$

$$\dot{N}_P = k^+ N_R - k^- N_P. \quad (1.2)$$

The existence of a steady state ($k^+ N_R = k^- N_P$) together with the Boltzmann distribution law implies, in terms of the equilibrium constant K , the detailed balance condition:

$$\frac{N_R}{N_P} = e^{-\beta(E_R - E_P)} = \frac{k^-}{k^+} = K. \quad (1.3)$$

The value of K , as well as any other equilibrium property, only depends on the energies of the two minima, without any reference to the energy barrier. The goal of the transition-state theory is to address the problem of the time evolution of N_R and N_P , obtaining an estimate for k^- and k^+ . This theory is based on two key assumptions:

1. *Strong-coupling*: thermodynamic equilibrium must prevail throughout the entire system for all the degrees of freedom. All effects that result from a deviation from the thermal equilibrium distribution are neglected.
2. *Point of no return*: a dividing surface separating reactants from products, referred as the transition state, can be identified. Any orbit crossing the dividing surface will not recross it.

The first assumption is necessary to ensure that reactants and products are distributed among their states according to the Maxwell-Boltzmann distribution. This implies that, after the occurrence of an exothermic reaction, the kinetic energy is redistributed among all the degrees of freedom before the occurrence of the next reaction. The second assumption states that the passage through the transition state without subsequent return is a “moment of decision” for the reacting system. By means of it $k^- = 0$, so that the time evolution of the reactants’ population is decoupled from the time evolution of products. Setting $k^+ = k$ we have for the reactants:

$$\dot{N}_R = -k N_R. \quad (1.4)$$

The TST rate is thus given by the total flux of classical trajectories from reactants to the products side of the dividing surface. From Figure 1.1 it is clear that the barrier is crossed whenever the transition state is reached with

a positive velocity. Indicating with q^* the coordinate of the transition state, the rate constant is given by the following thermal expectation value:

$$\begin{aligned}
 k &= \frac{\langle \frac{p}{m} \theta(p) \delta(q - q^*) \rangle}{\langle \theta(q - q^*) \rangle} \\
 &= \frac{1}{\langle \theta(q - q^*) \rangle} \int_{-\infty}^{+\infty} dp dq e^{-\beta \left(\frac{p^2}{2m} + V(q) \right)} \frac{p}{m} \theta(p) \delta(q - q^*) \\
 &= \frac{1}{\langle \theta(q - q^*) \rangle} e^{-\beta V(q^*)} \int_0^{+\infty} dp e^{-\beta \frac{p^2}{2m}} \frac{p}{m} \\
 &= \frac{1}{\langle \theta(q - q^*) \rangle} \frac{e^{-\beta V(q^*)}}{\beta},
 \end{aligned} \tag{1.5}$$

where we have performed the following integration:

$$\int_0^{+\infty} dp e^{-\beta \frac{p^2}{2m}} \frac{p}{m} = -\frac{1}{\beta} e^{-\beta \frac{p^2}{2m}} \Big|_0^{+\infty} = \frac{1}{\beta}. \tag{1.6}$$

At this point we restrict our discussion to those systems that can be described with reasonable accuracy within the harmonic approximation. For the one dimensional PES considered here this approximation has to be valid in the neighbourhood of the reactants' minimum. In the general $3N$ dimensional case the harmonic approximation is assumed to be valid for all the $3N$ degrees of freedom in the neighbourhood of reactants and for the $3N - 1$ degrees of freedom lying on the dividing surface around the transition state. This is typically the case of diffusion and reactions in crystals and at crystal surfaces, where atoms are usually tightly packed and the typical temperature of interest is low compared with the melting temperature. Of course this also imposes a constraint on the temperature range that can be considered within this framework: not only T must be much smaller than the activation energy E_A , but it must also be considerably smaller than the melting temperature. In this approximation $\langle \theta(q - q^*) \rangle$ can be computed expanding the potential energy function around q_0 , the coordinate of the minimum associated to the reactants, obtaining:

$$\begin{aligned}
 \langle \theta(q - q^*) \rangle &= \int_{-\infty}^{+\infty} dp dq e^{-\beta \left(\frac{p^2}{2m} + V(q_0) + \frac{1}{2} V''(q_0) q^2 \right)} \\
 &= e^{-\beta V(q_0)} \int_{-\infty}^{+\infty} dp dq e^{-\frac{\beta m}{2} \left(\frac{p^2}{m^2} + \omega^2 q^2 \right)} \\
 &= \dots \\
 &= \frac{2\pi}{\beta \omega(q_0)} e^{-\beta V(q_0)},
 \end{aligned} \tag{1.7}$$

where we have defined $\omega^2 = \frac{V''(q_0)}{m}$. The rate constant is thus given by:

$$k = \frac{1}{2\pi} \omega(q_0) e^{-\beta(V(q^*)-V(q_0))} = \frac{1}{2\pi} \omega(q_0) e^{-\beta E_A}. \quad (1.8)$$

This relation was first proposed by Jacobus Van't Hoff (1884) and Svante Arrhenius (1889) who gave an extensive discussion of various experimental reaction-rate data, observing that the rate constant, as a function of the inverse temperature $\beta = (K_B T)^{-1}$, varies on a logarithmic scale:

$$k = \mathcal{A} \cdot e^{-\frac{E_A}{K_B T}}. \quad (1.9)$$

This is known as the Van't Hoff-Arrhenius law. \mathcal{A} is a temperature independent *prefactor* with the dimension of a frequency. The dependency of the rate constant from the temperature and from the energy barrier is exclusively contained in the exponential term.

In the general $3N$ dimensional case the derivation of the Van't Hoff-Arrhenius expression requires further approximations. We start observing that two minima of a PES are always separated by, at least, one saddle point, i.e. a stationary point with a single imaginary normal-mode frequency. In what follows, the saddle point will be assumed to be the bottleneck for the reaction. The $3N - 1$ dimensional surface which divides reactants and products will be assumed to be orthogonal to the normal mode with imaginary frequency at the saddle point. With this definition for the dividing surface, the saddle point results to be a local minimum of the potential energy on such a surface.⁴

Within these approximations, the Van't Hoff-Arrhenius expression for the rate constant can be obtained by expanding the potential energy in normal modes. The integral that gives the reactive flux is performed by expanding the potential energy around the saddle point q^* , whereas the integral that gives the normalisation is done by expanding the potential energy around the reactants minimum q_0 . Following what has been done in the one dimensional case we obtain:

$$k = \frac{1}{2\pi} \frac{\prod_{i=1}^{3N} \omega(q_0)_i}{\prod_{i=1}^{3N-1} \omega(q^*)_i} e^{-\beta E_A}. \quad (1.10)$$

⁴Following the Newton's dynamics we know that the trajectories conserve the total energy $E(q_0, p_0)$ so that a system with total energy lower than the potential energy of the saddle point, $V(q^*)$, will never reach the products. The minimum energy required to jump is given by $V(q^*)$ and this corresponds to crossing the energy barrier at the saddle point. Since the phase space volume (and thus the probability) associated to each Newton's trajectory is proportional to its Boltzmann factor $e^{-\beta E(q_0, p_0)}$, those which cross the energy barrier at the saddle point are more probable.

A notable feature of this expression is that all the quantities involved can be evaluated from the potential energy surface, at zero temperature, thus not requiring the evaluation of the much more complicated free-energy landscape. Nevertheless entropic effects are also included in an approximate way in the rate constant through the expression of the prefactor.

The most important part of this calculation is the search for the relevant saddle points. Powerful methods have been developed for climbing up the potential energy surface from minima to saddle points, but they generally require the evaluation and the inversion of the Hessian matrix at each point along the search. Given their high computational cost, these methods are preferentially used when an analytical expression for the Hessian matrix is available (for instance in the case of empirical potentials). They are also used in quantum-chemistry calculations when only the minimum corresponding to the starting point of the reaction (reactants) is known and no information is available on the arrival point (products).

When both reactants and products are known, other techniques, requiring only first derivatives of the potential energy surface, can be employed to identify the saddle points. These methods derive from the observation that, when the temperature is low compared to the energy barrier, the transitions from reactants to products occur preferentially along a particular configuration-space path, called reaction pathway. This pathway, known as the *minimum energy path* (MEP), is characterised by being everywhere parallel to the gradient of the potential energy surface. It is formed by two branches which correspond to the two steepest-descent trajectories⁵ that depart from the saddle point, $q(s^*)$, separating reactants and products along the two directions of the imaginary frequency normal mode. The MEP can thus be written as:

$$\frac{dq(s)}{ds} = \begin{cases} \nabla V(q(s)) & \text{if } s < s^* \\ -\nabla V(q(s)) & \text{if } s > s^*, \end{cases} \quad (1.11)$$

where s no longer represents the time, being nothing but an arbitrary parametrisation of the path.

In the next chapter I shall describe two powerful techniques developed to identify the MEP which, requiring only first derivatives of the PES, result to be more efficient than those used to locate directly the saddle point. Moreover, in the next section it will be shown that, when the evolution of the system can be described by a first order Langevin equation, the MEP plays the role of the most probable reaction path.

⁵The steepest descent trajectory is defined as the one satisfying the following differential equation: $\frac{dq(s)}{ds} = -\frac{\nabla V(q(s))}{|\nabla V(q(s))|}$.

1.2 Transition probability from the Langevin equation

In principle an expression for the transition rate could be obtained in the framework of Newton's dynamics. In practice this results to be rather cumbersome because one has to work in the phase space of the whole system.

An alternative approach is based on the assumption that the whole phase space can be partitioned in two subsets, the former containing all the degrees of freedom relevant to describe the evolution of the system from reactants to products, the latter playing the role of a thermal bath. The coordinate $x(t)$ describes the dynamics in the first subspace and, as a consequence of this "coarse graining" procedure, is coupled to the thermal bath which can either donate or remove energy. The mathematics of such reduction has been worked out in full generality by Zwanzig [12] and Mori [13] within the framework of statistical mechanics, using the technique of projection operators. In the simplest description the reaction can be thought as a discrete stochastic process without any memory effect, whose evolution is described by a first-order Langevin equation:⁶

$$x_{i+1} = x_i - \varepsilon \nabla V(x_i) + \xi_i, \quad (1.12)$$

where ξ_i is a *Wiener* process:

$$\begin{aligned} \langle \xi_i \rangle &= 0 \\ \langle \xi_i \xi_j \rangle &= \sigma^2 \\ &= 2\varepsilon \delta_{i,j} K_B T. \end{aligned} \quad (1.13)$$

The above expression is obtained discretising the time $t \in [t_1, t_2]$ by N equispaced steps: $t_2 - t_1 = \varepsilon N$; the trajectory is thus given by $x(\varepsilon \cdot i) = x_i$, where $i = 0, \dots, N$. Since ξ_i are all Gaussian stochastic variables and are all decorrelated, the probability density for the entire process $(\xi_0, \dots, \xi_{N-1})$ is given by:

$$\mathcal{P}(\xi_0, \dots, \xi_{N-1}) = \frac{1}{(2\pi\sigma^2)^{\frac{N}{2}}} \cdot e^{-\sum_{i=0}^{N-1} \frac{(\xi_i)^2}{2\sigma^2}}. \quad (1.14)$$

With the change of variables $\xi_i = x_{i+1} - x_i + \varepsilon \nabla V(x_i)$ the probability density becomes:

$$\mathcal{P}(x_0, \dots, x_N) = \frac{\|J\|}{(2\pi\sigma^2)^{\frac{N}{2}}} \cdot e^{-\sum_{i=0}^{N-1} \frac{|x_{i+1} - x_i + \varepsilon \nabla V(x_i)|^2}{2\sigma^2}}, \quad (1.15)$$

⁶The problem of how close does the first order Langevin dynamics approximate the Newton dynamics is not easily answered. What is generally verified is that the long-time properties of the system are reasonably well described by a first-order Langevin dynamics.

where $\|J\|$ is the Jacobian determinant of the transformation. This Jacobian can be easily calculated:

$$\begin{aligned}\|J\| &= \det \left[\frac{\partial (x_i - x_{i-1} + \varepsilon \nabla V(x_{i-1}))}{\partial x_j} \right] \\ &= \det \left[\delta_{i,j} - \delta_{i,j+1} \cdot \left(1 + \varepsilon \frac{\partial}{\partial x_j} \nabla V(x_{i-1}) \right) \right] \\ &= 1.\end{aligned}\tag{1.16}$$

The probability density is thus given by:

$$\mathcal{P}(x_0, \dots, x_N) = \frac{1}{(4\pi\varepsilon K_B T)^{\frac{N}{2}}} \cdot e^{-\sum_{i=0}^{N-1} \frac{|x_{i+1} - x_i + \varepsilon \nabla V(x_i)|^2}{4\varepsilon K_B T}}.\tag{1.17}$$

Integrating all the intermediate variables we obtain an expression for the transition probability

$$w(x_0, t_1 | x_N, t_2) = \int \frac{dx_1 \cdots dx_{N-1}}{(4\pi\varepsilon K_B T)^{\frac{N}{2}}} \cdot e^{-\frac{\beta}{4} \sum_{i=0}^{N-1} \frac{1}{\varepsilon} |x_{i+1} - x_i + \varepsilon \nabla V(x_i)|^2},\tag{1.18}$$

that, in the continuous limit, becomes:

$$w(x(t_1) | x(t_2)) \sim \int \mathcal{D}[x(t)] e^{-\frac{\beta}{4} \int_{t_1}^{t_2} |\dot{x}(t) + \nabla V(x(t))|^2 dt}.\tag{1.19}$$

The time integral $S[t_1, t_2, x(t)]$ appearing in the above expression

$$S[t_1, t_2, x(t)] = \int_{t_1}^{t_2} |\dot{x}(t) + \nabla V(x(t))|^2 dt,\tag{1.20}$$

is a functional of the path $x(t)$ and is called Langevin action. The path that gives the largest contribution to the transition probability is the one that minimise the Langevin action. Instead of considering the transition between the stable states in finite time, I shall look for the optimal switching path which also minimise the action in t_1 and t_2 . Let $x(t)$, $t \in [t_1, t_2]$, be an arbitrary path satisfying the constraints $x(t_1) = \text{reactants}$ and $x(t_2) = \text{products}$. Indicating with $x(t^*)$ the configuration along the path where the potential energy is maximised, it can be shown that [14]:

$$S[t_1, t_2, x(t)] \geq 2[V(x(t^*)) - V(x(0))]\tag{1.21}$$

On the other hand, there exists a special curve, the MEP defined in the previous section by equation (1.11), that satisfies the lower bound of (1.21)

for $t_1 \rightarrow -\infty$ and $t_2 \rightarrow +\infty$. The Langevin action computed on the MEP is given by:

$$\begin{aligned} \int_{t_1}^{t_2} |\dot{x}(t) + \nabla V(x(t))|^2 dt &= 4 \int_{t_1}^{t^*} |\nabla V(x(t))|^2 dt \\ &= 4 \int_{t_1}^{t^*} \dot{x}(t) \cdot \nabla V(x(t)) dt \\ &= 4 [V(x(t^*)) - V(x(t_1))], \end{aligned} \quad (1.22)$$

so that, at the lowest order in β , the transition probability results to be proportional to the barrier height:

$$w(x(t_1)|x(t_2)) \sim e^{-\beta[V(x(t^*)) - V(x(t_1))]} = e^{-\beta E_A}. \quad (1.23)$$

A more accurate estimate of the transition probability can be obtained by performing a Taylor expansion of the Langevin action around the MEP. In particular, we let $x(t) = x^*(t) + \sqrt{\eta} y(t)$, where $\eta = K_B T$ and the perturbation $y(t)$ satisfies the boundaries $y(t_1) = 0$ and $y(t_2) = 0$. Then, at first order in the temperature η , we have:

$$\begin{aligned} S[x(t)] &= \int_{t_1}^{t_2} \left| \dot{x} + V'(x) \right|^2 dt \\ &= \int_{t_1}^{t_2} \left| \dot{x}^* + \sqrt{\eta} \dot{y} + V'(x^* + \sqrt{\eta} y) \right|^2 dt \\ &= \int_{t_1}^{t_2} \left| \dot{x}^* + V'(x^*) + \sqrt{\eta} \left(\dot{y} + V''(x^*) y \right) + \frac{\eta}{2} y V'''(x^*) y \right|^2 dt \\ &= S[x^*(t)] + \\ &\quad \eta \int_{t_1}^{t_2} \left[\left| \dot{y} + V''(x^*) y \right|^2 + \left(\dot{y} + V''(x^*) y \right) \cdot \left(y V'''(x^*) y \right) \right] dt, \end{aligned} \quad (1.24)$$

where we have used a Taylor expansion for the gradient of the potential energy function :

$$V'(x^* + \sqrt{\eta} y) = V'(x^*) + \sqrt{\eta} V''(x^*) y + \frac{\eta}{2} y V'''(x^*) y. \quad (1.25)$$

In the limit of $t_1 \rightarrow -\infty$ and $t_2 \rightarrow +\infty$, the transition probability is thus given by:

$$w(x(t_1)|x(t_2)) = \mathcal{C}_{t_1, t_2} e^{-\beta E_A}, \quad (1.26)$$

where the temperature independent prefactor $\mathcal{C}_{\mathcal{T}}$ is given by:

$$\mathcal{C}_{t_1, t_2} = \int \mathcal{D}[y] e^{-\frac{1}{2} \int_{t_1}^{t_2} \left[\left| \dot{y} + V''(x^*) y \right|^2 + \left(\dot{y} + V''(x^*) y \right) \cdot \left(y V'''(x^*) y \right) \right] dt}. \quad (1.27)$$

Chapter 2

Numerical methods

In this chapter I describe two techniques, the nudged elastic band method (H. Jónsson, G. Mills, K. W. Jacobsen, G. Henkelman and B. P. Uberuaga [3, 10, 11]) and the string method (W. E, W. Ren and E. Vanden-Eijnden [4]), that are currently used to identify the minimum energy path connecting stable states of the potential energy surface. I also describe some extensions to these approaches that I have developed with the aim of improving their performance and usability.

In the previous chapter the minimum energy path has been defined as the particular configuration-space path, connecting reactants and products, characterised by the property that the components of the forces orthogonal to the path are zero:¹

$$\nabla V(\mathbf{x}(s)) - \boldsymbol{\tau}(s) (\boldsymbol{\tau}(s) | \nabla V(\mathbf{x}(s))) = 0. \quad (2.1)$$

Here and in the following $\boldsymbol{\tau}(s)$ represents the normalised tangent vector and the MEP is parametrised by an arbitrary reaction coordinate $s \in [0, 1]$. It has also been shown that, within the framework of a stochastic description of the systems' dynamics of, the MEP is, in the low temperature limit, the most probable path that connects two minima in the PES. Equation (2.1) states that the potential energy is stationary on each hyperplane orthogonal to the MEP. However, only those path in which the energy is minimised on the orthogonal hyperplanes are physically relevant, the others having zero probability of being reaction paths.

The identification of the MEP and of the saddle point separating reactants and products can be achieved by solving numerically the equation (2.1).

¹In the following I indicate with $(\mathbf{a}|\mathbf{b})$ the dot product between two configuration space vectors \mathbf{a} and \mathbf{b} .

The first step consists in representing the path $\mathbf{x}(s)$, which is a continuous function, in a form suitable to be handled numerically. This is done by discretising the reaction coordinate s and by representing the path on this discretised mesh. The continuous path $\mathbf{x}(s)$ is thus represented by a “chain of images”:

$$\begin{aligned} s &\longrightarrow i \cdot \delta s \\ \mathbf{x}(s) &\longrightarrow \mathbf{x}_i \\ \boldsymbol{\tau}(s) &\longrightarrow \boldsymbol{\tau}_i = \frac{\mathbf{x}_{i+1} - \mathbf{x}_{i-1}}{|\mathbf{x}_{i+1} - \mathbf{x}_{i-1}|}. \end{aligned} \tag{2.2}$$

The discretised version of equation (2.1) is given by:

$$\nabla V(\mathbf{x}_i) - \boldsymbol{\tau}_i (\boldsymbol{\tau}_i | \nabla V(\mathbf{x}_i)) = 0. \tag{2.3}$$

The solution of this set (one for each point used to represent the path) of coupled non-linear equations represents the discretised MEP. Equations (2.3) are solved when, for each image, the energy is minimised on the hyperplane orthogonal to the discretised path. Such minimisation can be carried out iteratively using a sort of steepest-descent dynamics in the space of paths. The procedure is started by constructing the initial path as a chain of equispaced images. Then each image evolves following the fictitious dynamics given by the projected force:

$$\begin{aligned} F(\mathbf{x}_i)_\perp &= -[\nabla V(\mathbf{x}_i) - \boldsymbol{\tau}_i (\boldsymbol{\tau}_i | \nabla V(\mathbf{x}_i))] \\ &\Downarrow \\ \mathbf{x}_i(t + \delta t) &= \mathbf{x}_i(t) + \delta t F(\mathbf{x}_i(t))_\perp. \end{aligned} \tag{2.4}$$

The path is converged to the MEP when $\mathbf{F}(\mathbf{x}_i)_\perp = 0$ for all the images (\mathbf{x}_i) in the chain.²

The main limit of this approach is that this dynamics does not preserve the inter-image distance and, in general, does not prevent images to slide down in the two minima. Indeed, since the path is represented with limited accuracy, also the estimate of the tangent (and thus of the projections) is approximatively known and a residual component of the force parallel to the path acts on the images. This effect is more relevant when the number of images used in chain is small. The result is that the images start sliding down along the path, further reducing the accuracy of the projections. If this behaviour is not opposed, all the images of the chain can eventually collapse in the two minima. This effect is described in Figure 2.1 where,

²In practical calculations we require the $\|\mathbf{F}(\mathbf{x}_i)_\perp\|_\infty$ to be smaller ($\forall x_i$) than a given input threshold (`path_thr`).

however, it is also shown that, as a positive consequence of the projection of the forces, the variation of the inter-image distance is of order Δx^2 , where Δx is the image displacement:³ the inter-image distance is thus preserved at first order in the time step δt . From these observation it is clear that the

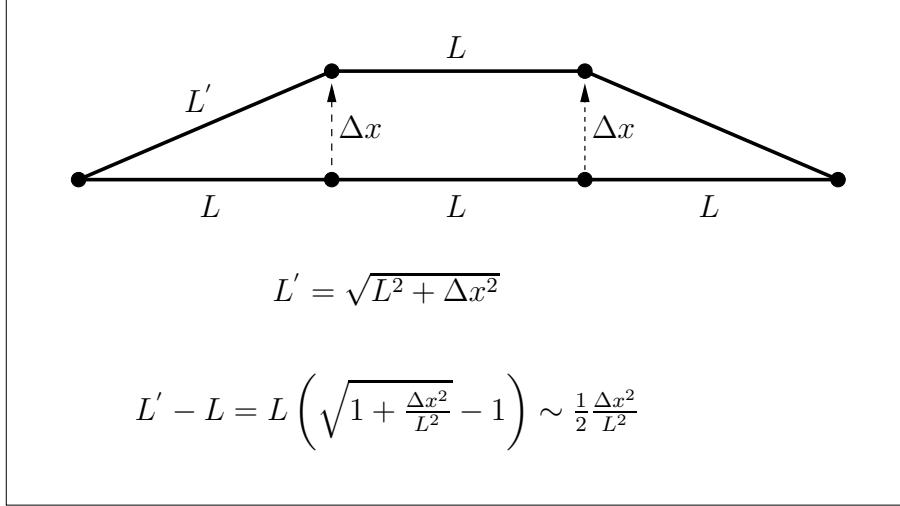


Figure 2.1: An illustration of the evolution of an equispaced path. It is shown that the variation in the inter-image distance is second order in the displacement Δx .

strategy used to discretise the path and the constraints imposed to preserve the parametrisation (i.e. the inter-image distance) are both of fundamental importance in the numerical solution of equation (2.3). In the following I shall describe two alternative approaches (the nudged elastic band and the string method) that differ in the way the parametrisation of the path is preserved.

2.1 The Nudged Elastic Band method

In the nudged elastic band method (NEB) [3, 10, 11] the path parametrisation is enforced by connecting each image of the chain to its neighbours by “virtual” springs of zero rest-length. The images feel both the forces due to the external potential (the true projected forces, $\mathbf{F}(\mathbf{x}_i)_\perp$) and those due to the “virtual” springs $\mathbf{F}(\mathbf{x}_i)^{elastic}$. The discretised path is thus described as an elastic band. Unfortunately, when the path bends the springs can introduce an artificial component of the force orthogonal to the path that prevents

³For simplicity, the displacement is supposed to be the same for all the images.

the chain to converge to the true MEP. As shown in Figure 2.2, this effect, which is generally referred to as “corner cutting”, is more relevant where the curvature of the path is larger. To reduce these spurious effects, in the NEB method the elastic forces are projected along the path’s tangent:

$$\mathbf{F}(\mathbf{x}_i)_{\parallel}^{elastic} = -k \boldsymbol{\tau}_i (\boldsymbol{\tau}_i | (2\mathbf{x}_i - \mathbf{x}_{i+1} - \mathbf{x}_{i-1})). \quad (2.5)$$

The procedure of projecting the spring forces is called *nudging* of the elastic

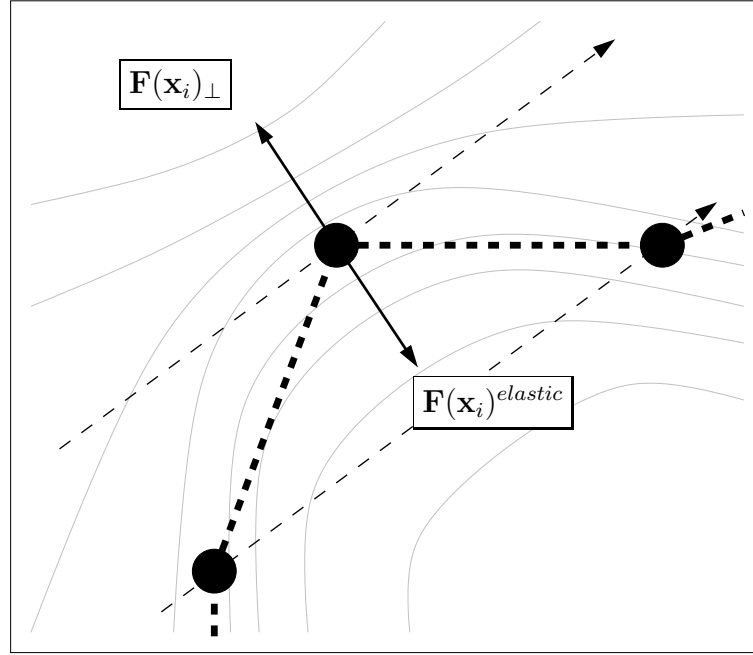


Figure 2.2: Illustration of the “corner cutting” problem.

band and represents the principal improvement offered by the NEB method against its predecessors (a review of these methods is contained in [3]): it is essential to decouple the effect of the “virtual” springs from the external potential. The chain that satisfies equation (2.3) in presence of the springs is found by evolving each image with the steepest-descent algorithm, where the overall force vector acting on the image \mathbf{x}_i at time t (hereafter indicated as $\mathbf{F}(\mathbf{x}_i(t)) = \mathbf{F}(\mathbf{x}_i(t))_{\perp} + \mathbf{F}(\mathbf{x}_i(t))_{\parallel}^{elastic}$) is used:

$$\mathbf{x}_i(t + \delta t) = \mathbf{x}_i(t) + \delta t \mathbf{F}(\mathbf{x}_i(t)). \quad (2.6)$$

In the NEB method the “virtual” springs act as a penalty function that, when all the elastic constants have the same value, favours the configuration of the chain where all images are equispaced. At convergence all the

inter-image distances are equal. As a consequence of the projections, this behaviour does not depend on the specific choice of the elastic constant, provided that they are larger than zero.⁴

2.1.1 Variable-elastic-constants NEB

In the NEB method the elastic forces act exclusively along the path; one is thus free to choose different spring constants between different pair of images without affecting the convergence of the chain to the MEP (this because the geometrical definition of MEP given by equation (2.1) is invariant for any reparametrisation of the path). Clearly, the saddle point is the most important configuration along the MEP and one would typically prefer to have higher resolution close to this point than near the end points. This can be accomplished within the variable-elastic-constants scheme, where stiffer springs are used near the point of highest energy. In particular, this is done by specifying a minimum and a maximum value for the elastic constants (k_{\min} and k_{\max}) and interpolating between these two values:⁵

$$k_i = \frac{1}{2} \left(k_{\max} + k_{\min} - (k_{\max} - k_{\min}) \cos \left(\pi \frac{(V(\mathbf{x}_i) - V_{\min})}{(V_{\max} - V_{\min})} \right) \right). \quad (2.7)$$

The variable-elastic-constant scheme thus provides a natural way of choosing the parametrisation of the path so that a minimum number of images is required to have a good estimate of the saddle point position. In the case described above the resolution is risen around points of high potential energy, which is a reasonable choice because the saddle point has the highest energy along the path. An alternative choice can be that of rising the path resolution (stiffer springs) around points of largest local curvature $\omega(s) = \frac{d\tau(s)}{ds}$. Indeed, the number of images required to represent a path depends on the global curvature of the path

$$\Omega = \int_0^1 |\omega(s)| ds. \quad (2.8)$$

A straight path can be represented by only two images, but a path that bends on itself many times can require a large number of images, even if the energy barrier is very small. I have observed that, by defining the discretised local curvature as $\omega_i = \frac{\mathbf{x}_{i+1} - \mathbf{x}_i}{|\mathbf{x}_{i+1} - \mathbf{x}_i|} - \frac{\mathbf{x}_i - \mathbf{x}_{i-1}}{|\mathbf{x}_i - \mathbf{x}_{i-1}|}$, “curvature-weighted” elastic constants can be used, obtaining an optimal parametrisation of the path. As in the

⁴Indeed, the effect of the external forces along the path is removed by the projections.

⁵The expression used here has been found to work better than the linear interpolation used in [10].

original recipe, the elastic constants are obtained interpolating between a minimum and a maximum value:

$$k_i = \frac{1}{2} \left(k_{max} + k_{min} - (k_{max} - k_{min}) \cos \left(\pi \frac{(\omega_i - \omega_{min})}{(\omega_{max} - \omega_{min})} \right) \right). \quad (2.9)$$

Within the variable elastic constants scheme the projected elastic forces are given by:

$$\begin{aligned} k_{i,i+1} &= \frac{1}{2} (k_i + k_{i+1}) \\ \mathbf{F}(\mathbf{x}_i)_{\parallel}^{elastic} &= -\boldsymbol{\tau}_i (\boldsymbol{\tau}_i | (k_{i,i+1} (\mathbf{x}_{i+1} - \mathbf{x}_i) - k_{i-1,i} (\mathbf{x}_i - \mathbf{x}_{i-1}))) \end{aligned} \quad (2.10)$$

As previously pointed out, the choice of the elastic constants (\mathbf{k}_{min} and \mathbf{k}_{max}) is not essential for the convergence of the path to the MEP because of the projection of the forces described above. Anyway, a wrong choice of the elastic constants can seriously affect the convergence rate of the chain of images to the MEP because it can introduce longitudinal modes of frequency much higher than the “physical” modes of the potential energy surface, resulting in a hill-conditioned optimisation problem. In this case the time step used to evolve the chain of images will be dictated by the artificial longitudinal modes. This is one of the more severe limitations to the usability of the NEB method. On the other hand It is known that the largest frequency supported by the elastic band is given by $\nu = \frac{1}{\pi} \sqrt{k_{max}}$. The optimal value of k_{max} can thus be obtained requiring that the time step, chosen small enough to well represent all the frequencies characterising the potential energy surface, is also smaller than ν^{-1} . In practice, given the time step as an input, k_{max} is automatically set to $k_{max} = \frac{\pi^2}{n^2 \delta t^2}$ (where n is some integer larger than one) so that also the elastic frequencies are well described. This implementation of NEB thus removes the duty of choosing the correct value for the elastic constants. Of course, the soft longitudinal modes of the elastic band are still present, thus influencing the convergence rate to the MEP. In the following it will be shown how this problem is solved by the string method.

2.1.2 Climbing Image NEB

The climbing image NEB (CI-NEB) method, introduced by G. Henkelman, B. P. Uberuaga and H. Jónsson in [10], is a slight, but important, improvement of the NEB method originally described in [3]. Information about the shape of the MEP is retained, but a rigorous convergence of an image to the saddle point is also obtained. This additional feature does not add any

significant computational effort. The climbing image scheme consists in the following procedure: after a few iterations with the regular NEB, the image with the highest energy i_{max} is identified. The force on this image is set to be the full force due to the potential with the component along the path inverted:

$$\mathbf{F}(\mathbf{x}_{i_{max}}) = -\nabla V(\mathbf{x}_{i_{max}}) + 2 \boldsymbol{\tau}_{i_{max}} (\boldsymbol{\tau}_{i_{max}} | \nabla V(\mathbf{x}_{i_{max}})). \quad (2.11)$$

Qualitatively, in the climbing-image scheme the maximum-energy image is forced to move up-hill along the path tangent and down-hill along all the directions perpendicular to the path tangent; moreover it is not affected by the spring forces at all. The other images of the chain serve the purpose of defining the one degree of freedom for which a maximisation (rather than a minimisation) of the energy is carried out. Since the images in the chain eventually converge to MEP, they give a good approximation to the reaction coordinate around the saddle point.

CI-NEB has proved to be extremely useful because it directly provides an accurate identification of the saddle point without any additional effort so that, at the end of a path optimisation, the activation energy and the saddle point coordinates are immediately available.

2.1.3 Improved tangent estimate

The stability and the efficiency of the NEB method strongly depend on the accuracy of the estimate for the local tangent $\boldsymbol{\tau}_i$. The simplest estimate is given by the normalised line segment between the two images used in equation (2.3), but a slightly better way is to bisect the two unit vectors

$$\boldsymbol{\tau}_i = \frac{\mathbf{x}_{i+1} - \mathbf{x}_i}{|\mathbf{x}_{i+1} - \mathbf{x}_i|} + \frac{\mathbf{x}_i - \mathbf{x}_{i-1}}{|\mathbf{x}_i - \mathbf{x}_{i-1}|}, \quad (2.12)$$

and then normalise $\boldsymbol{\tau} = \frac{\boldsymbol{\tau}}{|\boldsymbol{\tau}|}$. This latter way of defining the tangent ensures that the images are equispaced (when the elastic constants are the same), even in regions of large curvature. Unfortunately, this scheme may lead to the formation of kinks in the path in regions where the component of the potential force parallel to the MEP is large compared with the perpendicular components (a detailed description of this behaviour can be found in [11]). The numerical instability can be avoided by using an alternative definition of the local tangent, proposed by G. Henkelman and H. Jónsson in [11]. Instead of estimating $\boldsymbol{\tau}_i$ using both the adjacent images, $i+1$ and $i-1$, only the image with higher energy and the image i are employed, resulting in a

tangent defined as

$$\boldsymbol{\tau}_i = \begin{cases} \boldsymbol{\tau}_i^+ & \text{if } V_{i+1} > V_i > V_{i-1} \\ \boldsymbol{\tau}_i^- & \text{if } V_{i+1} < V_i < V_{i-1}, \end{cases} \quad (2.13)$$

where

$$\boldsymbol{\tau}_i^+ = \frac{\mathbf{x}_{i+1} - \mathbf{x}_i}{|\mathbf{x}_{i+1} - \mathbf{x}_i|} \quad \text{and} \quad \boldsymbol{\tau}_i^- = \frac{\mathbf{x}_i - \mathbf{x}_{i-1}}{|\mathbf{x}_i - \mathbf{x}_{i-1}|}, \quad (2.14)$$

and $V_i = V(\mathbf{x}_i)$. If both the adjacent images are either higher or lower in energy than image i , the tangent is taken to be a weighted average of the two tangent vectors $\boldsymbol{\tau}_i^+$ and $\boldsymbol{\tau}_i^-$. The weighted average is determined by the energy and only plays a role at extrema along the MEP. In these cases ($V_{i+1} > V_i < V_{i-1}$ or $V_{i+1} < V_i > V_{i-1}$) the tangent is defined as

$$\boldsymbol{\tau}_i = \begin{cases} \boldsymbol{\tau}_i^+ \delta V_i^{\max} + \boldsymbol{\tau}_i^- \delta V_i^{\min} & \text{if } V_{i+1} > V_{i-1} \\ \boldsymbol{\tau}_i^+ \delta V_i^{\min} + \boldsymbol{\tau}_i^- \delta V_i^{\max} & \text{if } V_{i+1} < V_{i-1}, \end{cases} \quad (2.15)$$

where

$$\delta V_i^{\max} = \max(|V_{i+1} - V_i|, |V_{i-1} - V_i|), \quad (2.16)$$

and

$$\delta V_i^{\min} = \min(|V_{i+1} - V_i|, |V_{i-1} - V_i|). \quad (2.17)$$

Finally, all the tangent vectors need to be normalised. With this modified tangent, the path is well behaved and converges rigorously to the MEP if a sufficient number of images is included.

2.2 The String Method

The string method⁶ constitutes a particularly elegant way of implementing the ideas outlined in the previous sections. It has been proposed by W. E, W. Ren and E. Vanden-Eijnden [4] and has been recently implemented by Y. Kanai and coworkers in the framework of Car-Parrinello first-principles molecular dynamics [15].

In the original implementation of the string method [4] the parametrisation of the path is enforced by redistributing the images whenever their

⁶In their work, Weinan E and coworkers call *string* what in this thesis has been called path.

reciprocal distance does not satisfy the required parametrisation. This procedure is performed by using a standard polynomial (cubic) interpolation scheme, based on the positions of the images at the previous step. The local tangent vectors are defined using the scheme described in 2.1.3. The main advantage of this approach with respect to NEB is that springs are no longer needed and their negative impact on the convergence rate of the optimisation procedure is removed.⁷ Moreover, the chosen parametrisation of the path is satisfied at each step. Since the dynamics given by equation (2.4) preserves the inter-image distance at first order in the time step (see Figure 2.1), the reparametrisation does not seriously interfere with the optimisation procedure.

This approach, based on interpolation and reparametrisation, is not suited to be used in conjunction with the Car-Parrinello first-principles molecular dynamics. The reason is that the resulting trajectory is not differentiable, thus conflicting with the fictitious dynamics of the Khon-Sham wavefunctions [1]. The approach followed in this case by Y. Kanai and coworkers [15] is to impose Lagrangian constraints on the inter-image distances so that all the images are equispaced at each step. The MEP is identified using a damped-dynamics procedure and the Lagrange constraints are enforced using the SHAKE algorithm [16].

An alternative way of enforcing the path parametrisation, based on the Fourier interpolation scheme, has been recently developed by the author. This approach is described in the next section.

2.2.1 Fourier representation

A continuous path can be described numerically in various ways. The simplest is probably the one given by the chain of images (2.3) that has been used up to now. An alternative approach is based on the natural correspondence that exists between a periodic function sampled on a discrete mesh (\mathbf{x}_i) and its discrete Fourier transform. To exploit this correspondence we start subtracting from the path $\mathbf{x}(s)$ the linear interpolation between the two end points:

$$\mathbf{y}(s) = \mathbf{x}(s) - \mathbf{x}(0) - s (\mathbf{x}(1) - \mathbf{x}(0)). \quad (2.18)$$

Each Cartesian component $y^\alpha(s)$ is a continuous function of the arc-length parametrisation, s , with boundary conditions given by $y^\alpha(0) = 0$ and $y^\alpha(1) = 0$. If we discretise the path using $N + 1$ images, the Cartesian component y_i^α becomes a function of the discrete index $i = 0, \dots, N$. The definition of

⁷The soft longitudinal modes of the elastic band have been eliminated.

each Cartesian component y_i^α can be extended so that the resulting function is periodic of period $2N$ (see Figure 2.3):

$$y_i^\alpha = \begin{cases} y_i^\alpha & \text{if } i < N \\ y_{2N-i}^\alpha & \text{if } N < i < 2N \end{cases} . \quad (2.19)$$

As explained in Appendix B, each periodic function y_i^α of period $2N$ such

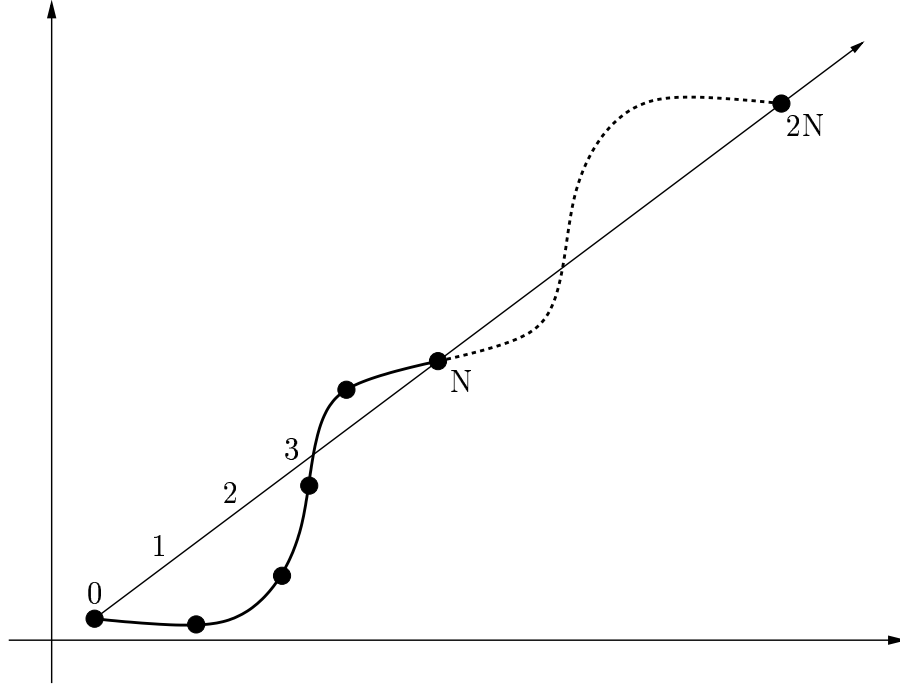


Figure 2.3: Schematic representation of the procedure used to extend the definition of a path. The resulting function is periodic and is zero at $i = 0$, $i = N$, $i = 2N$ so that it can be written as a sum of sines only.

that $y_0^\alpha = y_N^\alpha = y_{2N}^\alpha$ can be written as a sum of sines only:

$$y_i^\alpha = \sum_{n=1}^{N-1} \tilde{y}_n^\alpha \sin \left(2\pi n \frac{i}{2N} \right), \quad (2.20)$$

where the Fourier components \tilde{y}_n^α are defined as

$$\begin{aligned}
 \tilde{y}_n^\alpha &= \frac{1}{N} \sum_{i=1}^{2N-1} y_i^\alpha \sin\left(2\pi n \frac{i}{2N}\right) \\
 &= \frac{1}{N} \left[\sum_{i=1}^{N-1} y_i^\alpha \sin\left(2\pi n \frac{i}{2N}\right) - \sum_{i=N+1}^{2N-1} y_{2N-i}^\alpha \sin\left(2\pi n \frac{i}{2N}\right) \right] \\
 &= \frac{1}{N} \sum_{i=1}^{N-1} y_i^\alpha \left[\sin\left(2\pi n \frac{i}{2N}\right) - \sin\left(2\pi n \frac{2N-i}{2N}\right) \right] \\
 &= \frac{2}{N} \sum_{i=1}^{N-1} y_i^\alpha \sin\left(\pi n \frac{i}{N}\right).
 \end{aligned} \tag{2.21}$$

The initial path \mathbf{x}_i , discretised with $N + 1$ images, can thus be described using the two end points and $N - 1$ Fourier modes $\tilde{\mathbf{y}}_n$:

$$\mathbf{x}_i = \mathbf{x}_0 + \frac{i}{N} (\mathbf{x}_N - \mathbf{x}_0) + \sum_{n=1}^{N-1} \tilde{\mathbf{y}}_n \sin\left(\pi n \frac{i}{N}\right). \tag{2.22}$$

The same Fourier modes can also be used to define the tangent

$$\boldsymbol{\tau}_i = \frac{1}{N} (\mathbf{x}_N - \mathbf{x}_0) + \frac{\pi}{N} \sum_{n=1}^{N-1} n \tilde{\mathbf{y}}_n \cos\left(\pi n \frac{i}{N}\right), \tag{2.23}$$

and the curvature

$$\boldsymbol{\omega}_i = -\frac{\pi^2}{N^2} \sum_{n=1}^{N-1} n^2 \tilde{\mathbf{y}}_n \sin\left(\pi n \frac{i}{N}\right). \tag{2.24}$$

This Fourier representation is particularly useful because it provides an accurate and straightforward interpolation scheme that can be used, during the optimisation procedure, to redistribute the images along the path, changing the inter-image distance. Indeed, the configuration of the system corresponding to an arbitrary value of the reaction coordinate $s \in [0, 1]$ is given by:

$$\mathbf{x}(s) = \mathbf{x}_0 + s (\mathbf{x}_N - \mathbf{x}_0) + \sum_{n=1}^{N-1} \tilde{\mathbf{y}}_n \sin(\pi n s). \tag{2.25}$$

Given the Fourier modes $\tilde{\mathbf{y}}_n$, equation (2.25) can be used to construct a new representation of the path where the images are disposed as preferred, for instance equispaced.

A possible advantage of this approach compared to that of W. E and coworkers is that the tangent is obtained from a global representation of the path. It is thus reasonable to expect the projection of the of the forces to be more accurate than with the local definition of the tangent given by the equations described in 2.1.3. Moreover, within this Fourier reparametrisation scheme, it is quite easy to change the number of images “on the fly” during the optimisation.⁸ This suggests that it can be convenient to start the optimisation from a path defined by a single image (plus the two end points), adding other images as soon as the error drops under a predefined threshold. With this strategy the number of force evaluations needed to converge to the MEP is considerably reduced.

2.3 Quick-min optimisation scheme

As explained at the beginning of this chapter, the path optimisation can be performed using a standard steepest-descent algorithm. A more efficient method is based on the velocity Verlet algorithm which is routinely used for simulating classical dynamics.⁹ At each time step the coordinates and velocities of each image are updated according to the forces evaluated at the current coordinates, following the Newton’s equation of motion. In this section I shall use a bra-ket notation to represent configuration space vectors. If the kinetic energy is completely removed from the system at each time step (this can be done by setting the velocity to zero) the algorithm reduces to the steepest-descent optimisation. A more efficient procedure is to keep the component of the velocity parallel to the force at the current step, unless it

⁸Images can be added or removed in reciprocal space.

⁹In the velocity Verlet algorithm the Newton’s equations of motion are integrated using the following scheme [16]:

- step I :

$$\begin{aligned} x(t + \delta t) &= x(t) + \delta t \dot{x}(t) + \frac{\delta t^2}{2} \ddot{x}(t) \\ \dot{x}(t + \frac{\delta t}{2}) &= \dot{x}(t) + \frac{\delta t}{2} \ddot{x}(t) \end{aligned}$$

- step II :

$$\ddot{x}(t + \delta t) = -\nabla V(x(t + \delta t))$$

- step III :

$$\dot{x}(t + \delta t) = \dot{x}(t + \frac{\delta t}{2}) + \frac{\delta t}{2} \ddot{x}(t + \delta t)$$

is pointing in a direction opposite to the force

$$|\dot{x}_i(t)\rangle = \begin{cases} |\hat{F}_i(t)\rangle \langle \dot{x}_i(t) | \hat{F}_i(t) \rangle & \text{if } \langle \dot{x}_i(t) | \hat{F}_i(t) \rangle > 0 \\ 0 & \text{if } \langle \dot{x}_i(t) | \hat{F}_i(t) \rangle < 0, \end{cases}$$

where i is the image index and $|\hat{F}_i(t)\rangle$ is the normalised force vector. When the system overshoots the minimum, the velocity is zeroed. A further improvement of this method can be achieved by assuming that the force vector $|F_i(t)\rangle$ is the (minus) gradient of a potential function and exploiting the fact that, when the velocity is zeroed (case $\langle \dot{x}_i(t) | \hat{F}_i(t) \rangle < 0$), a root of the force vector ($\langle \hat{F} | \hat{F} \rangle = 0$) should exist between $|x_i(t - \delta t)\rangle$ and $|x_i(t)\rangle$. The next integration step can thus be performed using an “optimal” time-step, obtained estimating the local Hessian matrix. Let’s define the following vectors (the image index is understood) :

$$\begin{aligned} |g(t)\rangle &= -|F(t)\rangle \\ |y(t)\rangle &= (|g(t)\rangle - |g(t - \delta t)\rangle) \\ |s(t)\rangle &= (|x(t)\rangle - |x(t - \delta t)\rangle). \end{aligned} \tag{2.26}$$

The local curvature of the potential energy surface along the $|y(t)\rangle$ direction is thus approximatively given by:

$$\omega = \sqrt{\frac{\langle y(t) | s(t) \rangle}{\langle s(t) | s(t) \rangle}}, \tag{2.27}$$

and the approximate inverse Hessian matrix is given by:

$$H^{-1} \simeq \omega^{-2} \frac{|s(t)\rangle \langle s(t)|}{\langle s(t) | s(t) \rangle}. \tag{2.28}$$

In this approximation the minimum is supposed to be found in:

$$\begin{aligned} |x_{min}\rangle &\simeq |x(t)\rangle - H^{-1}|g(t)\rangle \\ &\simeq |x(t)\rangle - \omega^{-2} \frac{|s(t)\rangle \langle s(t)|}{\langle s(t) | s(t) \rangle} |g(t)\rangle \\ &\simeq |x(t)\rangle - \frac{|s(t)\rangle \langle s(t)|}{\langle y(t) | s(t) \rangle} |g(t)\rangle. \end{aligned} \tag{2.29}$$

Since $|\dot{x}(t)\rangle = 0$, from the velocity Verlet algorithm we have that:

$$|x(t + \delta t)\rangle = |x(t)\rangle + \frac{1}{2} \delta t^2 |F(t)\rangle. \tag{2.30}$$

Setting $\delta t = 1$, the best approximation for the minimum position is obtained by using the following force vector:

$$|F^{best}(t)\rangle = 2 \frac{|s(t)\rangle\langle s(t)|}{\langle y(t)|s(t)\rangle} |g(t)\rangle. \quad (2.31)$$

All these approximations are reasonable provided that the force vector $|F(t)\rangle$ is the (minus) gradient of a potential. In the case of path optimisations this is not true. Anyway, in the author’s experience this scheme, referred as “smart-step”, has often been able to speed-up the convergence of the chain of images to the MEP (see Table 2.1).

The optimisation procedure depicted above is performed on all the images separately. During the first stages of the optimisation it often happens that the force acting on a given image is much larger than the forces acting on all the others. In this case it is worth optimising only those images with the larger force, keeping the others frozen. After some tests I have realised that it is convenient to keep frozen a given image whenever $|F(x_i)|$ is smaller than half of the largest one, $|F|_{max}$. As shown in Table 2.1, this procedure, referred to as “freezing”, permits a considerable saving in the number of force evaluations needed to converge and, at the same time, makes the optimisation procedure much more robust.

Method	N° of force evaluations
plain NEB	426
plus “freezing”	255
plus “smart-step”	244
plus “Fourier parametrisation”	221

Table 2.1: Comparative of the number of force evaluations needed to identify the MEP on the two dimensional Mueller PES. The path is described by a chain of 10 images and the quick-min algorithm is used. The chain is optimised until the force acting on each image is smaller than 0.01.

2.4 Implementation

The NEB and the string methods, as outlined in the previous sections, have been implemented by the author in the open-source Quantum-ESPRESSO package [17]. In this implementation the path optimisation is performed on the electronic ground state (the Born-Oppenheimer surface), so that a full

self-consistency is required for each image at each step. This is by far the most demanding part of the whole calculation, in terms of both memory and cpu time. The optimisation scheme outlined above permits a very efficient parallelisation in which different pools of cpus work on different images; the communication between pools is negligible. The load balancing is optimised by adopting the strategy depicted in Figure 2.4, where, as an example, 2 pools (pool 1 and pool 2) are used on a path discretised by N images. Pool 1 starts working on image 1 and pool 2 on image 2. The first pool that reaches the self-consistency starts working on image 3, communicating to the other one that the next image available is 4. For particular systems, it may occur that the self-consistency on image 2 takes so long to be completed that all the other images are done by pool 1.

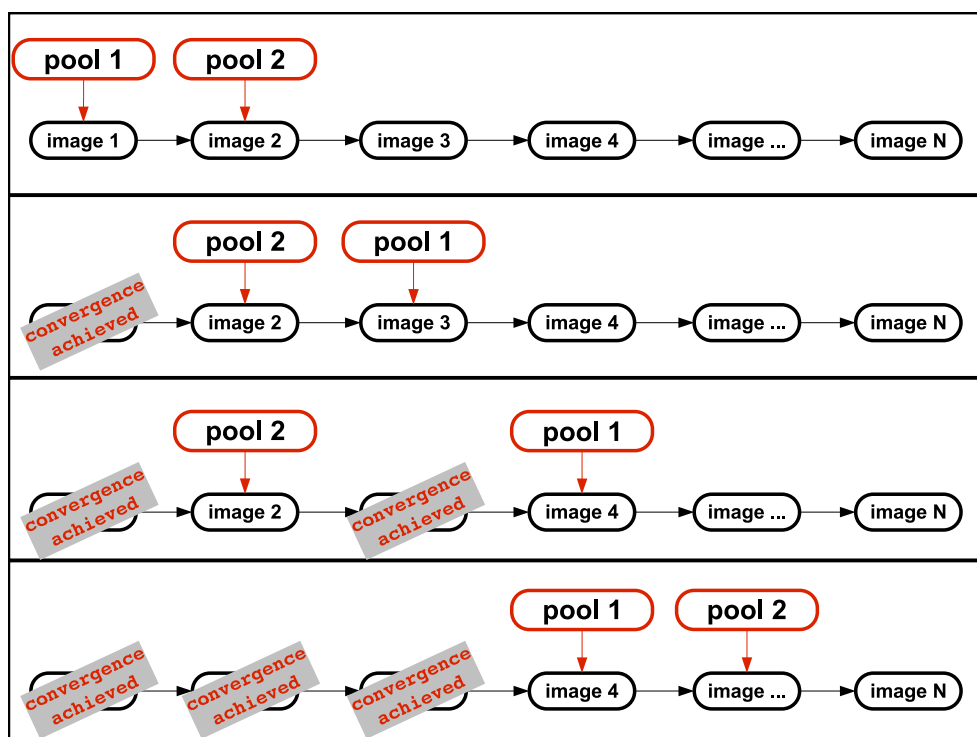


Figure 2.4: Parallelisation scheme used for NEB calculations. Here it is assumed that 2 pools (pool 1 and pool 2) are used on a path discretised by N images. Pool 1 starts working on image 1 and pool 2 on image 2. The first pool that reaches the self-consistency (pool 1) starts working on image 3, and so on.

A similar implementation of NEB has also been included in gNEB [18], a stand-alone program that can be easily interfaced to other molecular mod-

elling codes, independently of the approach used to compute the forces. At present gNEB has been interfaced to the Car-Parrinello CPMD code [19] and to a classical molecular dynamics code, developed by the author, which implements the extended Brenner potential [20].

All these computational tools have been used by the author, in collaboration with others, to investigate the kinetics of different chemical reactions occurring at surfaces of semiconductors and transition metals. In the following chapters I shall present in detail three works selected as representative of different ways of using the methodology described here. A short description of all the works, that I have contributed, in which the implementations of NEB have been used is presented in Chapter 6.

Chapter 3

Acetylene chemisorption on Si(111)-(7×7)

In this chapter I present a first application of the techniques previously described. The problem considered here is the study of the interaction of acetylene with the Si(111)-(7×7) surface; a traditional ab initio investigation of the many possible chemisorption configurations is supplemented by the identification of low energy reaction pathways leading to such structures. These results have been obtained in collaboration with C. A. Pignedoli, A. Catellani, R. Di Felice, P. L. Silvestrelli, F. Toigo, F. Ancilotto, C. M. Bertoni and published in [21].

In recent years the interaction of hydrocarbons with silicon surfaces has become the subject of many experimental and theoretical studies due to its fundamental and technological relevance. The largest amount of theoretical and experimental work has been devoted to the study of the growth of silicon carbide (SiC) films on the Si(100) surface. Nevertheless, a number of experimental and theoretical papers recently appeared [22, 23, 24] discussing the interaction of simple unsaturated organic molecules, like acetylene, with the Si(111)-(7×7) surface as possible routes for the low-temperature production of SiC films.

The first proposal for a chemisorbed state of acetylene on Si(111)-(7×7) was made by Yoshinobu and co-workers [25], based on high-resolution electron energy loss spectroscopy experiments performed at room temperature. They found that at such temperature acetylene is predominantly adsorbed non-dissociatively, and its bonding with the Si substrate results in a state of hybridisation intermediate between sp^2 and sp^3 . An adsorbed structure was proposed in which acetylene is di- σ bonded to the Si surface, bridging

adjacent adatom/restatom dangling bonds (“bridge” structure).

More recently, the electronic structure and bonding geometry of acetylene adsorbed at room temperature on the Si(111)-(7×7) surface was studied by a combination of synchrotron radiation x-ray photoemission spectroscopy and of near-edge x-ray absorption fine structure spectroscopy [22]. The spectroscopic data confirmed that the molecule chemisorbs non dissociatively, with conspicuous changes in its electronic structure and in the silicon surface states. This evidence again supports a di- σ “bridge” configuration between adatom/restatom pairs. A quantitative estimate of the (presumably small) tilt angle of the adsorbed molecule with respect to the surface plane was not possible.

The room temperature adsorption and the thermal reaction of acetylene on the Si(111)-(7×7) surface has been later investigated by means of ultraviolet-photoemission spectroscopy and high-resolution electron-energy-loss spectroscopy (HREELS) [23]. The evolution of the restatom— and adatom—related electronic states as a function of acetylene exposure was found to be well described by a modified di- σ bonding model, in agreement with previous measurements [22]. For higher exposure, however, when all the restatom dangling bonds are saturated by di- σ bonded molecules, the adsorption process can continue through saturation of the remaining adatoms, which are twice as the number of restatoms. In this new phase of the adsorbed acetylene, a substantial molecular tilting is inferred [23], leading to the speculation that a “vertical” configuration of the adsorbed molecule is also present. No microscopic model for such a state, however, exists.

Not surprisingly, given the complexity of the Si(111)-(7×7) surface, theoretical calculations of molecule adsorption on this surface are scarce, often based on simplified models of the actual surface structure. DFT calculations of the interaction of unsaturated hydrocarbons with the Si(111)-(7×7) surface have been recently reported, based on a cluster model of the (7×7) surface [24]. The basic mechanism underlying the chemisorption of acetylene is found to be a cycloaddition reaction between the C-C bond of the molecule and an adatom/restatom dangling bond pair. It is found however that the adsorption of acetylene on the Si(111) surface follows a stepwise, diradical pathway. The rate-determining step is the first one, *i.e.* the formation of a singlet-diradical intermediate, with an overall barrier height of 0.16 eV for the complete chemisorption reaction from the unbound molecule in the vicinity of the surface to the lowest-energy “bridge” structure. As we demonstrate in the following, the results of Ref. [24] are however biased by spurious effects due to the cluster geometry used in the calculations, which induces an unrealistic surface distortion in the formation of the “bridge” structure.

In the following sections we shall present a detailed study of the interac-

tion between the Si(111)-(7×7) surface and acetylene by using both *ab initio* and semi-empirical methods, where the surface is modelled by means of periodically repeated slabs. To confirm the preliminary proposal suggested in a previous study on the same topic [26], we perform accurate *ab initio* calculations for the chemisorption of C₂H₂ on a model Si(111) surface. Our *ab initio* investigation is preceded and complemented by a thorough analysis of the configuration space for the adsorbed molecule via empirical simulations on a full (7×7) surface. This allows us to identify the most relevant chemisorption sites and also to describe the possible paths for molecular adsorption.

3.1 Theoretical model

According to the widely accepted model of the (7×7) reconstruction of the Si(111) surface, there are 19 dangling bonds per (7×7) cell: among these, 12 belong to the adatoms, 6 to the restatoms (i.e. the surface Si atoms not saturated by the adatoms) and 1 to the Si atom at the bottom of each corner hole [27]. Due to the very complex reconstruction of this surface, several adsorption sites are thus possible even for relatively simple molecules like C₂H₂, and many reaction paths may occur leading to molecular dissociation and eventually to incorporation of the dissociated C atoms into the Si substrate.

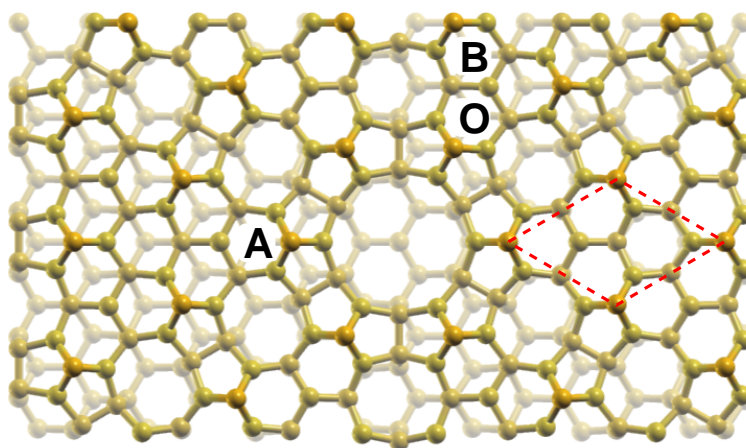


Figure 3.1: Top view of the Si(111)-(7×7) reconstructed surface. A rectangular cut of the surface, containing 2 unit cells is shown. The labels indicate the sites considered for the adsorption of a single C₂H₂ molecule. The dashed lines represent the (2×2) cut investigated by *ab initio* calculations. Dark yellow balls indicate the surface adatoms.

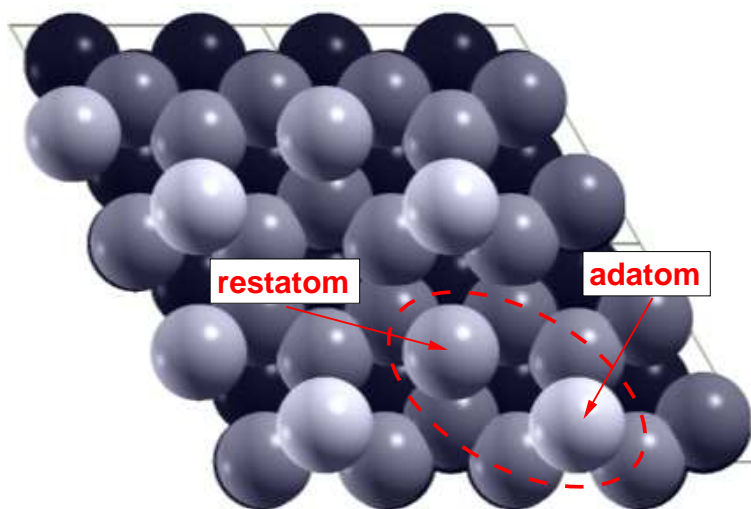


Figure 3.2: Top view of the Si(111)-(2×2) surface used in the *ab initio* calculations, with the adatom/restatom couple highlighted.

The (7×7) unit cell is too demanding to be used in a full *ab initio* simulation that includes also organic molecules. However *ab initio* calculations are still feasible for a smaller system. We have used (2×2) supercell with a Si adatom in the “T4” site, that mimics the most relevant part of the original (7×7) reconstruction, *i.e.* the adatom/restatom pair [26]. In Figure 3.1 we show a top view of the Si(111)-(7×7) surface: the dashed cell represents the (2×2) portion considered in our *ab initio* calculations. This cell is also shown in finer detail in Figure 3.2, where the adatom/restatom couple is highlighted. In the chosen (2×2) unit cell we included six double-layers plus a vacuum region, 12 Å wide, separating the repeated images of the slab: the bottom layer dangling bonds are saturated with hydrogen atoms. The 5 top double layers are allowed to relax. Brillouin Zone (BZ) integration is performed using a (2×2×1) Monkhorst-Pack mesh. We find that in the (2×2) cell the equilibrium adatom/restatom distance is 4.57 Å (compared to the LDA value of 4.48 Å obtained for the (7×7) reconstruction [27]) and the distance between similar adatom sites is also in close agreement with the original value given for the (7×7) surface since it corresponds to the cell parameter of the Si(111)-(2×2). The distance between the adatom and the corresponding atom of the second layer (on the vertical of the adatom) is 2.44 Å, in agreement with the value 2.40 Å obtained within LDA for the (7×7) reconstruction [27]. All the details of our *ab initio* calculations are reported in Appendix A.

In order to obtain a more complete scenario of chemisorption geometries

for the C_2H_2 molecule, we have also performed semi-empirical calculations on a slab containing two (7×7) unit cells (see Figure 3.1) and 7 Si double-layers (for a total of 1380 Si atoms), the bottom double-layer being kept fixed in the bulk positions. We have used the extended Brenner (XB) empirical potential for carbon-hydrogen-silicon systems [28], that takes into account the chemical environment of the atoms as well as their geometrical relationships with one another. In particular, this potential is able to describe important aspects of carbon chemistry, such as “bond conjugation” and “bond order”. Moreover, unlike traditional molecular mechanics force fields, this potential is able to describe processes involving bond breaking and forming (i.e. chemical reactions). We used here a recently proposed variant of the XB potential [20], which we found to better describe the adsorption and chemical reactions of organic molecules on Si surfaces. Semi-empirical potentials have been used in the past to compute the properties of the $\text{Si}(111)-(7\times7)$ surface [28, 29]: the results were found to reproduce the stability of this reconstruction and to provide a qualitatively good description of chemisorption configurations of simple molecules.

3.2 Semi-empirical calculations: chemisorption sites of C_2H_2 on $\text{Si}(111)-(7\times7)$

The $\text{Si}(111)-(7\times7)$ surface presents a number of inequivalent adatom/restatom pairs (both in the faulted and unfaulted halves). We thus exploited the optimised semi-empirical potential outlined in the previous section, and used in recent works [20] to study the chemisorption of organic molecules on the $\text{Si}(100)$ surface: the use of the semi-empirical potential allowed us to simulate the complete (7×7) reconstructed cell. Chemisorption sites were identified using the damped-dynamics algorithm. In this section we describe the set of semi-empirical calculations carried out on the $\text{Si}(111)-(7\times7)$ surface, whereas the *ab initio* results are reported in the next section.

Our calculations based on the semi-empirical potential predict differences in the acetylene binding energies of 0.1-0.2 eV at most on similar sites of the faulted and unfaulted halves of the (7×7) cell, respectively (the sites on the faulted half being always energetically favoured). Thus we will consider hereafter only chemisorption of acetylene on the faulted half of the (7×7) surface. We have compared chemisorption geometries and binding energies for configurations where the C_2H_2 molecules chemisorb in a “bridge”-like state where the C atoms in the molecule saturate the dangling bonds of an adjacent adatom/restatom pair (i.e. in the di- σ bonded configuration suggested by

the experimental results previously described). We distinguish between two possible such states, i.e. “bridge” and “broken-bridge” configurations: while in the former the Si adatom maintains its bonding structure with the underlying Si atoms, in the latter one of the adatom-substrate bonds is broken upon chemisorption. We consider several “bridge”-like structures, i.e. where the acetylene molecule is bonded to the adatom/restatom couples in the non-equivalent “A”, “O” and “B” sites (see Figure 3.1). The resulting binding energies (see Table 3.1) on the A sites are ~ 0.4 eV higher than those on the B ones, the O sites having somewhat intermediate values: in all the cases, however, the “broken-bridge” configurations are always favoured with respect to the corresponding “bridge” ones. In order to compare our semi-empirical results with the more accurate *ab initio* results reported in the next section, which are performed in a (2×2) supercell, we have also calculated the binding energies for the “broken-bridge” configuration computed on the same (2×2) cell used in the *ab initio* calculations, by using the semi-empirical potential (see Table 1). A comparison with the resulting binding energies for the same configurations on the Si(111)-(7×7) surface shows that the value obtained with the (2×2) cell is roughly equal to the average value of the binding energies on the three non-equivalent A, O and B sites on the full Si(111)-(7×7) surface (the average is 3.93 eV). This result supports the expectation that the smaller (2×2) cell represents a reasonable model for the full Si(111)-(7×7) surface.

In agreement with previous *ab initio* studies [26], the present calculations based on the semi-empirical XB potential confirm that the “broken-bridge” structure shown in Figure 3.3 is indeed the most stable chemisorption configuration of acetylene on Si(111): the geometry is characterised by a binding energy in the range $[3.70 \div 4.15]$ eV (depending on the chemisorption site, see Table 3.1) and by a C-C distance of 1.31 Å. A “bridge” configuration (i.e. where the adatom maintains its backbonds intact), shown in Figure (3.4), is also identified as an equilibrium state, with a binding energy in the range $[3.36 \div 3.77]$ eV (*i.e.* ~ 0.4 eV lower than that of the “broken-bridge” one) and a carbon/adatom distance increased by $\sim 4\%$ with respect to the “broken-bridge”, suggesting that this configuration induces a considerable stress on the surface. Moreover the adatom/surface distance is increased by 3% with respect to the clean surface, indicating some stretching of the adatom backbonds as well: from the above results one could envisage the possibility of a facile “bridge” to “broken-bridge” conversion. Indeed, our *ab initio* calculations reported below do not even predict the stability of a “bridge” structure, giving instead the “broken-bridge” one as the only stable configuration bridging an adatom/restatom pair.

A distinctive feature of the Si(111)-(7×7) surface is the presence of 9 non-

Configuration	binding energy (eV)
“bridge” A	3.77
“broken-bridge” A	4.15
“bridge” O	3.53
“broken-bridge” O	3.93
“bridge” B	3.36
“broken-bridge” B	3.70
“broken-dimer”	2.08
“top” A	1.09
“top broken-adatom” A	1.71
“upright” A	1.41
“quasi-upright” A	2.56
“coupled-bridge” A	3.93
“tetra- σ ”	2.12
“broken-bridge” on $\text{Si}111-(2\times 2)$	3.88

Table 3.1: Binding energies (eV per chemisorbed C_2H_2 molecule) obtained with the XB semi-empirical potential.

equivalent Si surface dimers. They differ from those characterising, e.g., the $\text{Si}(100)-(2\times 1)$ surface for the absence of dangling bonds and are thus non reactive sites. Nevertheless, the chemisorption of an acetylene molecule may induce the breaking of dimers. The resulting “broken-dimer” configuration is shown in Figure 3.4 and is characterised by a double C-C bond (1.30 \AA) parallel to the surface. Although this structure, with a binding energy of 2.08 eV, is less stable than all the “bridge” ones, it represents a well defined minimum of the potential energy surface that does not involve the adatom/restatom couple and can thus coexist with the “bridge”-like configurations.

Besides the “bridge” configurations involving pairs of restatoms and adatoms, we have also considered other structures, described in the following, in which the acetylene molecule is bound to the adatom only (labelled “top”, “upright” and “quasi-upright” configurations). These configurations are supposed to play a role in the high coverage regime of acetylene adsorption on the $\text{Si}(111)-(7\times 7)$ surface: in fact, when all the adatom/restatom pairs are saturated by acetylene molecules chemisorbed in “bridge”/“broken-bridge” configurations, there still remain unsaturated adatoms (6 per surface (7×7) unit cell) available for further chemisorption. At high acetylene coverage, on the basis of the observed HREELS spectra, the authors of Ref. [23] suggest that another chemisorption structure may occur, which is characterised by

a more “vertical” geometry than that of “bridge”-like configurations. One possibility is represented by the “top” configuration shown in Figure 3.4: in this case an acetylene molecule can bind to an adatom (the restatoms are supposed to be all saturated by molecules in the “bridge”-like configurations) forming a single C-Si bond, or to an adatom characterised by a broken bond with the substrate (hereafter labelled “top broken-adatom”), thus forming two C-Si bonds as shown in Figure 3.3. In both cases these configurations are considerably less stable (by 3 eV) than the “broken-bridge” structure. Moreover the angle that the C-C bond forms with the Si(111) surface plane is comparable with the one realised in the “broken-bridge” structure. In order to explain the experimental evidence of a quasi-vertical adsorbed molecule, one would need a configuration characterised by a double C-C bond (the stretching frequency must be close to that of the “broken-bridge” structure since no significant shift of the HREELS peak has been observed at higher coverage [23]) and at a larger angle with the surface than that occurring in the “broken-bridge” configuration. Moreover this configuration should not involve restatoms since at high coverage they are supposed to be all saturated by acetylene molecules in “broken-bridge” sites. A possible candidate for such a vertical structure is the “upright” configuration shown in Figure 3.3, characterised by a C-C bond length of 1.32 Å and by a binding energy of 1.14 eV.

Another interesting state is represented by the “quasi-upright” structure of Figure 3.3: it is less stable than the “broken-bridge” structure, but significantly more stable than the “top” and “upright” ones. A similar configuration has been proposed for the chemisorption of acetylene on the Si(100)-(2×2) surface (configuration 1,2-hydrogen transfer described in Ref. [30]). However, in that case the C atom of the molecule is bonded to two Si atoms of the same dimer and the resulting conjugated C-C bond is longer (1.43 Å) than the corresponding C-C bond in the configuration computed here. The realisation of the “quasi-upright” and “upright” configurations implies the transfer of a H atom from the C atom bonded to the surface to the other C atom in the molecule during the chemisorption process. We shall show in the following that a reaction pathway for such a reaction does indeed exist, and it is characterised by a relatively small energy barrier.

One consequence of the formation of a “broken-bridge” structure is that it creates a new dangling bond on the surface (in fact the Si atom that was previously bonded to the adatom is now three-fold coordinated); moreover the adatom, although bound to the acetylene molecule, is still reactive. Thus, a further adsorption site with a chemical environment similar to the adatom/restatom couple is realised on the surface and another acetylene molecule can stick to the same adatom resulting in a “coupled-bridge” con-

figuration (see Figure 3.3). The binding energy of this structure, computed with the semi-empirical XB potential, is 3.93 eV per C₂H₂ molecule (only the site A is considered), i.e. higher than the binding energy of the “broken-bridge” structure in sites different from “A”. We shall show in the following that chemisorption of the second molecule can proceed with an energy barrier similar to that encountered for the chemisorption of acetylene in the “broken-bridge” configuration.

We have finally considered a configuration in which the acetylene molecule induces the breaking of two adatom backbonds, sticking to the two resulting surface dangling bonds and to the adatom itself. The resulting configuration, hereafter called “tetra- σ ” (see Figure 3.3), has a binding energy of 2.12 eV, lower than that of “bridge” configurations, but comparable with that of the “broken-dimer” or “quasi-upright” ones. The configuration is characterised by single C-C bond, parallel to the surface (the bond length is 1.56 Å) and considerably weaker than all other C-C bonds taken into account.

The above picture leads naturally to conjecture a saturation coverage of 28 acetylene molecules per (7×7) unit cell: 12 bound to “coupled-bridge” configurations (all the 6 restatoms are thus saturated), 6 in vertical “quasi-upright” configurations saturating the remaining 6 adatoms, 9 in the “broken-dimer” state and one bonded to the adatom in the corner-hole. The actual occurrence of a given chemisorption reaction is, however, largely determined by kinetic effects, *i.e.* one should consider the overall reaction pathways involved in the realisation of the various structure described above: this important issue will be address in a following section.

3.3 Ab initio calculations: chemisorption sites of C₂H₂ on Si(111)-(2×2)

Our *ab initio* study of the chemisorbed states of acetylene on the (2×2) Si(111) surface confirms that the “broken-bridge” configuration is the most stable one, with a binding energy of 2.09 eV (see Table 3.2); note that the XB potential overestimates this value by a factor 2. In this structure the carbon atoms of the acetylene molecule respectively bind to the adatom and to a neighbouring restatom of the Si surface in a di- σ configuration characterised by a double C-C bond (in fact, after chemisorption in this structure the C-C bond-length, which in the isolated acetylene molecule is 1.21 Å, is increased to 1.36 Å, i.e. a double C-C bond results). As we have already observed in the previous section, one of the three bonds that the adatom forms with the surface is broken after acetylene chemisorption so that the strain induced on

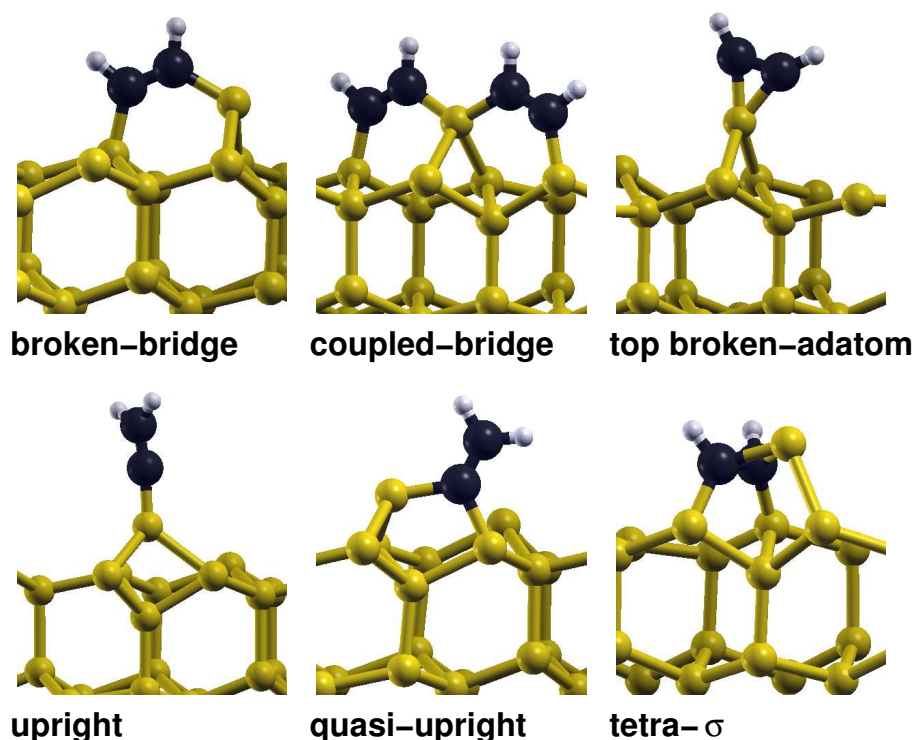


Figure 3.3: Stable configurations for the chemisorption of acetylene on the Si(111)-(7×7) surface as obtained by means of *ab initio* calculations. White, black and yellow balls indicate H, C, Si atoms, respectively.

the surface by attachment of acetylene can be largely reduced.

On the clean Si surface, a Löwdin population analysis [31] shows that an electronic charge transfer takes place from the adatoms ($-0.15 e^-$) to the restatoms ($+0.15 e^-$), so that the corresponding dangling bonds are almost completely empty and filled, respectively (see the left panel of Figure 3.5). At the same time, the restatom (adatom) undergoes a strong outward (inward) relaxation with respect to its ideal position, such that its dangling bond becomes more *s*- (*p_z*-) like. When an atom is adsorbed, a counter-relaxation takes place, indicating a reverse restatom/adatom charge transfer. For an atom at the adatom site, this counter-relaxation is such to increase the strain in the adatom backbonds, and even break the bond between the adatom and the second layer atom just below. A discussion of this effect is contained in Ref. [26], where the stability of such a configuration is related to the electronic bonding charge redistribution between the adatom/restatom pair. Indeed, the adatom empty state and bonding states are strongly modified upon acetylene chemisorption, resulting in the breaking of a Si-Si bond (as

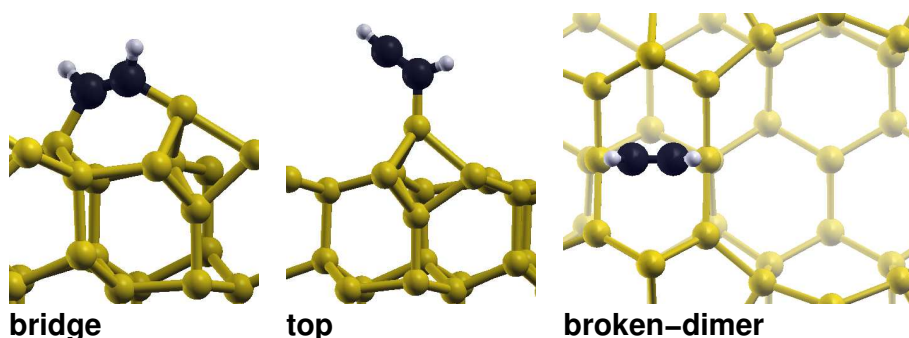


Figure 3.4: Stable configurations for the chemisorption of acetylene on the Si(111)-(7×7) surface that do not have an *ab initio* counterpart. White, black and yellow balls indicate H, C, Si atoms, respectively. In the case of the “broken-dimer” structure a top view is shown.

Configuration	binding energy (eV)	d_{C-C} (Å)
“broken-bridge”	2.09	1.36
“bridge”	—	—
“top”	—	—
“top broken-atom”	0.67	1.34
“upright”	0.26	1.31
“quasi-upright”	2.06	1.35
“coupled-bridge”	2.85	1.35
“tetra-σ”	1.77	1.56

Table 3.2: *Ab initio* binding energies (eV per chemisorbed C₂H₂ molecule) and structural parameters (Å).

evidenced in Figure 2 of Ref. [26]). Again a Löwdin population analysis [31] confirms this picture for the “broken-bridge” configuration, showing that a reverse charge transfer takes place from the restatom ($-0.32 e^-$) to the carbon atoms ($+0.37 e^-$) of the chemisorbed acetylene molecule (see right panel of Figure 3.5).

At variance with the results of the semi-empirical XB calculations reported in the previous subsection, we find no evidence of equilibrium *ab initio* “bridge” structures: in fact, despite many attempts aimed at its stabilisation, this structure invariably converts during the relaxation procedure into the “broken-bridge” one. The fact that the XB calculations do predict this structure may be due to the inability of the empirical potential to describe subtle electronic effects as those involved in “bridge”-like geometries.

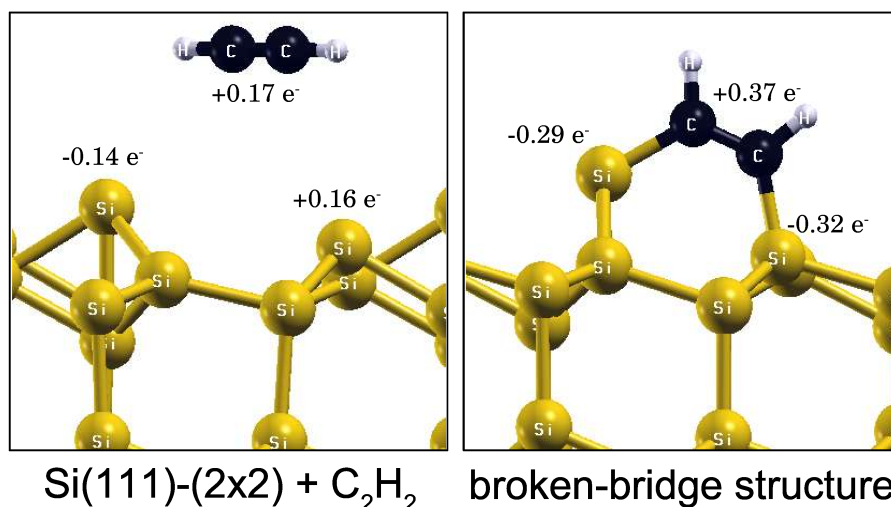


Figure 3.5: Charges obtained from Löwdin population analysis. In the left panel the charge transfer that occurs on the bare Si(111)-(2×2) surface from the adatom to the restatom is shown. It is also shown that in the isolated acetylene molecule a considerable charge transfer occurs from the hydrogens to the carbon atoms. In the right panel it is shown the charge redistribution occurring upon acetylene chemisorption.

The scenario is similar for the “top” configurations: *ab initio* calculations predict the stability of the “top broken-adatom” configuration only, whose binding energy is 0.67 eV. Again the XB potential overestimates the binding energy by a factor 3 and predicts configurations that result to be unstable in *ab initio* calculations.

The prediction of a stable “upright” configuration, where the acetylene molecule binds in a vertical state, is instead confirmed by our *ab initio* calculations. Nevertheless, with a binding energy of only 0.26 eV, this state results to be at the verge of instability. On the contrary the “quasi-upright” structure has a binding energy of 2.06 eV, almost degenerate with that of the “broken-bridge” structure and the geometry is consistent with the hypothesis that this is the configuration which is observed at high coverage in the HREELS experiments of Ref. [23]. The C-C bond length of 1.35 Å (1.36 Å in the “broken bridge”) suggests that gross vibrational properties of the C-C bond should be the same as those that characterise the “broken bridge” configuration. Moreover, the angle formed by the C-C bond with the surface plane is 24° for the “broken-bridge” and 64° in the case of the “quasi-upright” structure (see Figure 3.6). This scenario confirms that a chemisorption configuration involving only adatoms, considerably more vertical than the “broken bridge”

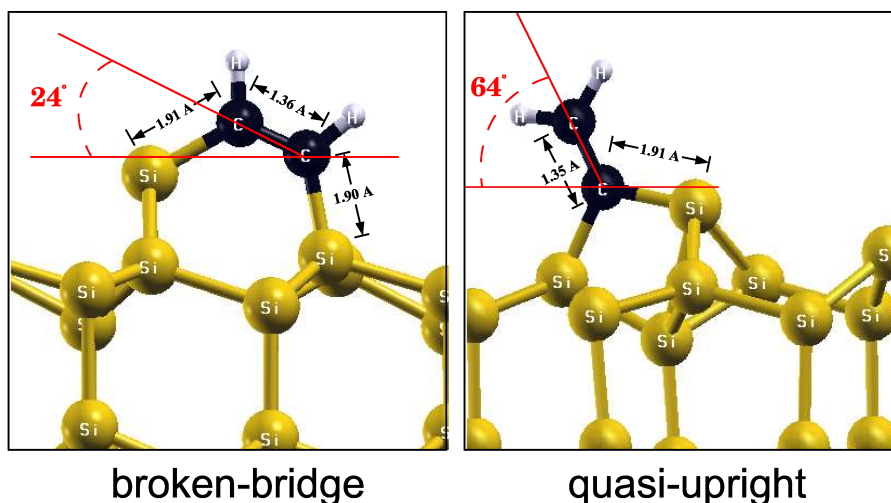


Figure 3.6: The tilt angles described in the text are shown for the “broken-bridge” and “quasi-upright” structures.

one and with roughly the same binding energy is possible.

The interesting prediction of a “coupled-bridge” configuration which is able to accommodate two acetylene molecules per adatom/restatom pair is also confirmed by our *ab initio* calculations. This configuration is the most stable among those possible on a (2×2) unit cell, having a binding energy of 2.85 eV per C_2H_2 molecule, i.e. 36% higher than that of the “broken-bridge” configuration. The two acetylene molecules display the same structural parameters of the “broken-bridge” configuration and are symmetrically arranged with respect to the plane defined by the adatom and by the two backbonds with the surface (see Figure 3.3).

Finally, the prediction of a “tetra- σ ” configuration, characterised by a single C-C bond, is also confirmed; the binding energy of this structure is 1.77 eV whereas the structural parameters are the same obtained with the XB potential. We observe that the highly stable, double-bonded, C-C dimers in “bridge”-like configurations at the $Si(111)$ surface, obtained through C_2H_2 deposition, prevents the formation of SiC at low temperatures and are therefore in contrast with the evidence of SiC growth. On the contrary the “tetra- σ ” configuration can be considered an example of a stable chemisorption structure in which the weaker C-C bond can break, thus suggesting the possibility of the formation of SiC clusters.

From these results we conclude that, although the semi-empirical XB potential provides a qualitative description of the adsorption geometries of acetylene on the $Si(111)-(7\times 7)$ surface, the *ab initio* study is mandatory to

confirm the effective stability of the identified structures and to obtain a quantitative analysis of the energetics.

We have to stress that none of the identified configurations is capable of explaining the formation of SiC clusters by acetylene chemisorption. Indeed the growth of SiC takes place at relatively high temperatures (900-1000 K); at such temperatures diffusion of adatoms on the surface plays a fundamental role and the structures identified in our study are probably already dissociated.

3.4 Reaction pathways and energy barriers

We have explored the chemisorption kinetics of acetylene on Si(111)-(7×7) by estimating various possible reaction pathways and energy barriers characterising the reaction of single molecules on the surface.

Although our calculations indicate that the “broken-bridge” is the most stable chemisorption configuration for the intact molecule, the mechanism for chemisorption at room temperature is still an open issue. We have identified a possible mechanism leading to this stable geometry, in which the energy barrier that the system has to overcome is 0.53 eV (see Figure 3.7). This activation energy suggests an easy saturation (at room temperature) of all adatom/restatom couples. In the process thus identified the energy cost for breaking the adatom backbond is partially reduced by the simultaneous formation of a new Si-C bond. In the starting configuration the acetylene molecule is parallel to the surface and randomly rotated with respect to the adatom/restatom axis. During the chemisorption, the molecule can freely orient itself parallel to the adatom/restatom axis before converting to the “broken-bridge” structure.

Once the first acetylene molecule is chemisorbed in the “broken-bridge” configuration, the energy barrier that a second molecule has to overcome to attach to the surface in the “coupled-bridge” structure is 0.42 eV, i.e. of the same order of magnitude as the energy barrier characterising the formation of a “broken-bridge” structure. We can thus expect that, when the temperature is high enough for the formation of the “broken-bridge” structure to occur with significant probability, a second molecule can easily stick to the same site in the “coupled-bridge” configuration with a similar probability. *Ab initio* calculations thus confirm the picture which emerged from semi-empirical calculations, i.e. that adatom/restatom couples are saturated by acetylene molecules in the “coupled-bridge” structure.

We have also identified a path that drives the acetylene molecule from the gas phase to the “quasi-upright” configuration, overcoming two energy

barriers and going through the “upright” stable intermediate configuration. Surprisingly, while in this complex chemisorption mechanism the energy barrier that the system has to overcome to reach the “upright” configuration is 0.89 eV, only 0.16 eV are required to give rise to the more stable “quasi-upright” structure (see Figure 3.8). This result confirms the conjecture that at low temperature the most favourable chemisorption structure is a “bridge”-like one. Nevertheless at higher acetylene exposures the energy barrier that hinders the formation of the “quasi-upright” configuration can be overcome, giving rise to a more vertical C-C bond stretching signal, as suggested in Ref. [23].

Among other possible chemisorption configurations, the “broken-dimer” one is particularly interesting since it does not involve adatom/restatom pairs. Since such a structure cannot be represented in our (2×2) unit cell, we have used the XB potential that allows us to study this reaction on the full (7×7) unit cell. Although this structure is less stable than both the “broken-bridge” and the “quasi-upright” (see subsection 3.1), the energy barrier that a molecule in the gas phase has to overcome to chemisorb on the surface is only 0.50 eV. Given the rough approximations used in this last calculation (only a semi-empirical calculation has been possible) no much emphasis should be put on this result. Nevertheless we expect that this picture could be qualitatively correct so that also the “broken-dimer” structure is expected to be already present on the surface at room temperatures, thus supporting the conjecture of a saturation coverage of 28 acetylene molecules per (7×7) unit cell.

Let us finally comment on recent theoretical results for acetylene chemisorption on a model (2×2) adatom/restatom geometry, within *ab initio* calculations and adopting a cluster geometry to describe the surface structure [24]. The authors of Ref. [24] found that the adsorption of acetylene on the Si(111) surface follows a two-step pathway, in which the rate-determining step is the first one, i.e. the formation of an intermediate state, with an overall barrier height of 0.16 eV for the complete chemisorption reaction into a “bridge” structure. No such intermediate state is found in our calculations, which is probably a consequence of the more realistic description of the surface when a slab geometry is adopted, rather than a finite cluster. In particular, the small cluster of Ref. [24] does not allow for a proper description of the breaking of the adatom bond and thus the intermediate state should be considered as an artifact of the cluster geometry. Indeed in their final “bridge” configuration the adatom is fourfold coordinated, whereas in our calculations it results to be threefold coordinated since only the “broken-bridge” configuration is found to be stable.

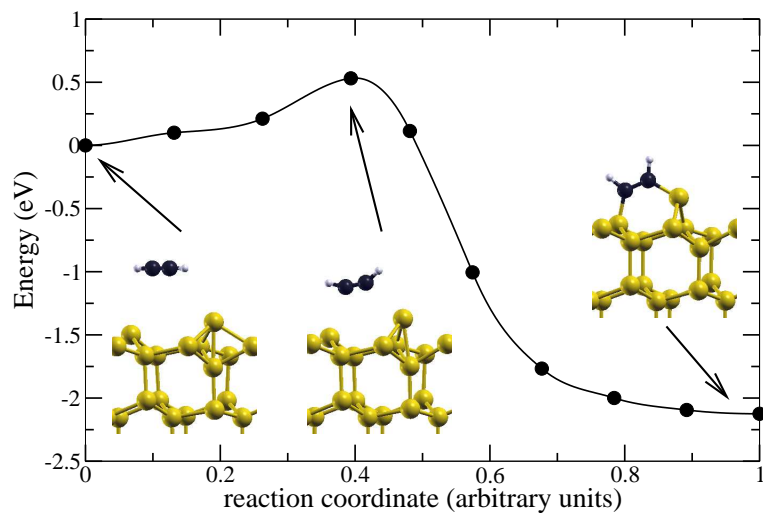


Figure 3.7: Energy profile for the chemisorption of the acetylene molecule in the “broken-bridge” configuration. The zero of the energy is the vacuum level and corresponds to a free C_2H_2 molecule and a clean Si(111)-(2×2) surface.

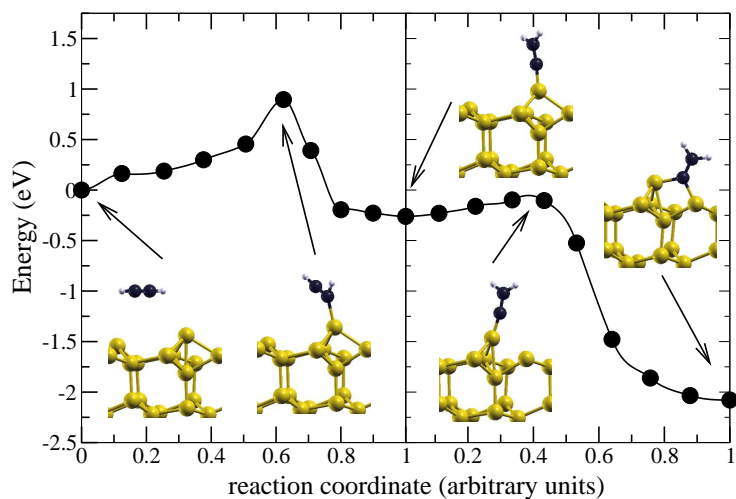


Figure 3.8: Energy profile for the chemisorption of the acetylene molecule in the “quasi-upright” configuration via the “upright” intermediate state. The zero of the energy is the vacuum level and corresponds to a free C_2H_2 molecule and a clean Si(111)-(2×2) surface.

Chapter 4

Deconstruction kinetics of the Rh(110)-1×2 missing row surface

In this chapter I present the results of the study of the deconstruction process of the Rh(110)-1×2 missing-row surface. This work, motivated by a collaboration with an experimental group working at ELETTRA (Trieste), has been done in collaboration with N. Bonini, A. Dal Corso, and S. Baroni. In this case, the methodology developed to identify reaction pathways described in Chapter 2 has been of fundamental importance to discern, among others, that particular microscopic mechanism responsible of the deconstruction process.

The (110) surface is the most “open” among the low-index faces of the fcc metals because it has the lowest surface density. In a few fcc metals of the 5d-series, such as gold, platinum and iridium, the most stable form of the (110) surface is a (1×2) missing row reconstruction, where every second close-packed atomic row is missing. For most other fcc metals, however, there is no stable missing-row state, and the surface ground state has a simple (1×1) geometry. Rhodium belongs to this latter group. However, it is known that the (110) surface of rhodium undergoes this (1×2) missing row reconstruction upon oxygen adsorption at a coverage of half a monolayer (0.5 ML), forming a structure with (2×2)-p2mg periodicity [32]. The driving force of this reconstruction process is the strong electrostatic repulsion between the adsorbed oxygen atoms. By titration with hydrogen the surface can be reduced, forming water molecules that immediately desorb, leaving a clean (1×2) missing-row reconstructed surface. At temperatures below 400 K this metastable state can be maintained for several hours, while the evolution toward the equilibrium (1×1) phase is very fast above 500 K.

The deconstruction process of this surface has been investigated in the

past by means of Helium Atom Scattering (HAS) [33] and Scanning Tunnelling Microscopy (STM) [34]. Results from HAS [33] suggest that adjacent $[1\bar{1}0]$ rhodium rows pair-up coherently, forming long islands with (1×4) symmetry. Subsequent STM studies [34] confirmed this picture, indicating that this coherent mechanism is ignited at steps or at other defect sites. These studies also showed that diffusion of Rh adatoms along the missing rows contributes to the deconstruction of the surface and that, once again, this process is originated at steps. These results suggest that the thermal stability of the (1×2) structure is closely related to the activation barrier of atomic diffusion at the surface which is expected to occur via simple processes, such as hopping or vacancy migration [35, 36] or by more complex mechanisms involving a larger number of atoms, such as exchange processes [37].

Recently, the possibility of investigating the kinetics of the deconstruction process using real-time high-resolution core level photoelectron spectroscopy has motivated a collaboration with an experimental group working at the *ELETTRA* synchrotron radiation facility in Trieste.¹ Because of the high surface sensitivity and very local character of the surface core level components, the population of differently coordinated atoms at the surface can be quantitatively monitored as a function of time at different substrate temperatures. This has allowed to detect the existence of activated processes involving a change in the local atomic structure and to determine an activation energy of 0.95 ± 0.13 eV for the overall deconstruction process. On the basis of this result, we have performed first-principles calculations aimed at providing a detailed description of the microscopic mechanisms responsible for the observed kinetic behaviour, which is not directly accessible to the experiment.

4.1 Properties of the Rh(110) and Rh(110)-1×2 surfaces

A detailed description of the methodology used in our first-principles calculations is reported in Appendix A. All the rhodium surfaces considered in this work have been modelled by 6-layer slabs; the bottom two layers were fixed at the bulk truncated structure and the others were left free to relax so as to minimise the surface energy. The different stages of the deconstruction process have been modelled using (1×2) , (1×4) , (2×2) , (3×2) , and (4×2) surface unit cells. Brillouin Zone integrations have been performed using, respectively, $(8\times 4\times 1)$, $(8\times 2\times 1)$, $(4\times 4\times 1)$, $(3\times 4\times 1)$, and $(2\times 4\times 1)$

¹A. Baraldi, S. Lizzit, F. Bondino, G. Comelli, and R. Rosei.

Monkhorst-Pack meshes.

The equilibrium lattice constant, a_0 , and bulk modulus, B_0 , of rhodium have been determined by computing the total energy as a function of the unit cell volume and by fitting the results with a Murnaghan's equation of state.² The results, reported in Table 4.1, are in reasonable agreement with experimental estimates and with other first principles results. A side view of

	This work	Ref.[38]	experiment [39]
a_0 (bohr)	7.29	7.20	7.19
B_0 (Mbar)	2.56	3.17	2.69

Table 4.1: Equilibrium lattice constant a_0 and bulk modulus B_0 of rhodium.

both the relaxed (110) surface and the (1×2) reconstructed surface is shown in Figure 4.1. The interplanar relaxations obtained for the two structures are reported in Table 4.2 and are again in good agreement with other first principles calculations (see, for instance, those reported in [40]).

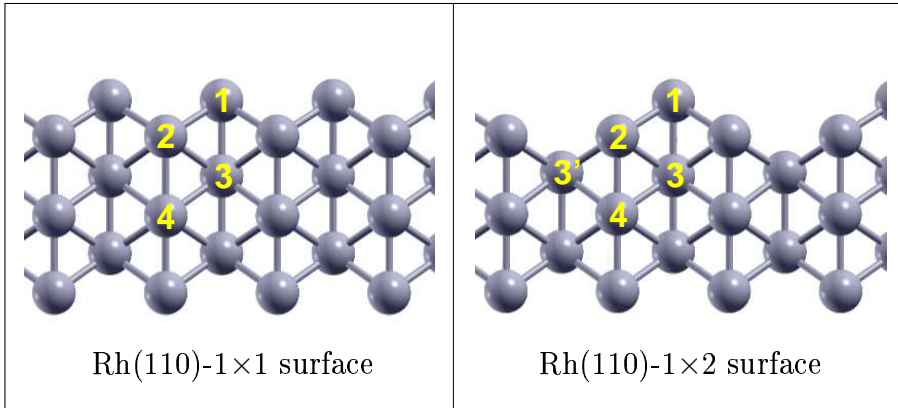


Figure 4.1: Side view of the pristine Rh(110)-1×1 surface (on the left) and of the Rh(110)-1×2 missing row reconstructed surface (on the right).

²In the Murnaghan's equation of state the crystal energy is expressed as

$$E(V) = \frac{V_0 B_0}{B'_0} \left[\frac{1}{B'_0 - 1} \left(\frac{V_0}{V} \right)^{B'_0 - 1} + \frac{V}{V_0} \right]$$

where B'_0 is the derivative of B_0 with respect to the pressure and $V_0 = \frac{a_0^3}{4}$ is the equilibrium volume

	Δz_{1-2}	Δz_{2-3}	$\Delta z_{2-3'}$	Δz_{3-4}	$\Delta z_{3'-4}$
perfect Rh(110)	- 9.60 %	0.06 %	—	0.57 %	—
Rh(110)-1×2	-10.72 %	-0.16 %	-7.97 %	-2.58 %	5.22 %

Table 4.2: Interplanar relaxations of both the perfect and missing-row reconstructed Rh(110) surfaces expressed as percentage of the bulk interplanar spacing (2.58 bohr). Refer to Figure 4.1 for the labelling.

The stability of the two phases of Rh(110), namely the (1×1) unreconstructed and the (1×2) missing-row reconstructed surfaces, has been compared by computing their surface energies, σ , defined by:

$$E_{tot} = N \cdot E_{bulk} + 2 \cdot S \cdot \sigma. \quad (4.1)$$

Here it is assumed that a slab with inversion symmetry is used to model the surface; E_{tot} is the total energy of the slab, N is the number of atoms in the slab and S is the number of surface unit cells. σ and E_{bulk} are obtained by computing the total energies of the slabs for increasing number of layers and doing a least-squares fit of the results. We have obtained $\sigma = 1.64$ eV for the (1×1) unreconstructed phase and $\sigma = 1.66$ for the (1×2) missing row reconstructed. These results confirm that the unreconstructed surface is more stable (it has a lower surface energy), the difference being however quite small.

4.2 Lattice-gas Hamiltonian

The missing-row reconstructed surface can be viewed as a periodic sequence of $[1\bar{1}0]$ chains of Rh adatoms adsorbed on the perfect (110) surface. A schematic top view of the fcc (110) surface is depicted in Figure 4.2, where the four possible adsorption sites for the single adatom are also indicated. In order to investigate the stability of this structure we have computed the binding energy of adatoms adsorbed on a (2×2) unit cell at different coverages and in different geometries. We have verified that Rh adatoms bind exclusively in the hollow site, the top, long-bridge and short-bridge sites being unstable (these latter two are saddle points). The results, reported in Table 4.3, have been mapped onto a lattice-gas Hamiltonian which accounts for interactions up to third neighbours:

$$E = J_1 \sum_i \sigma_i + \frac{1}{2} \sum_i \left[J_2^S \sum_j^S \sigma_i \sigma_j + J_2^L \sum_j^L \sigma_i \sigma_j + J_2^D \sum_j^D \sigma_i \sigma_j \right], \quad (4.2)$$

where $\sigma_i = 1$ if the site i is occupied, $\sigma_i = 0$ otherwise. As shown in Figure 4.2, J_1 represents the energy of an isolated adatom and $J_2^{S,L,D}$ give the corrections to the energy due to pair-interactions for first, second, and third neighbours. A negative value of the couplings denotes an decrease of the energy and describe an attractive interaction. Assuming that the interactions

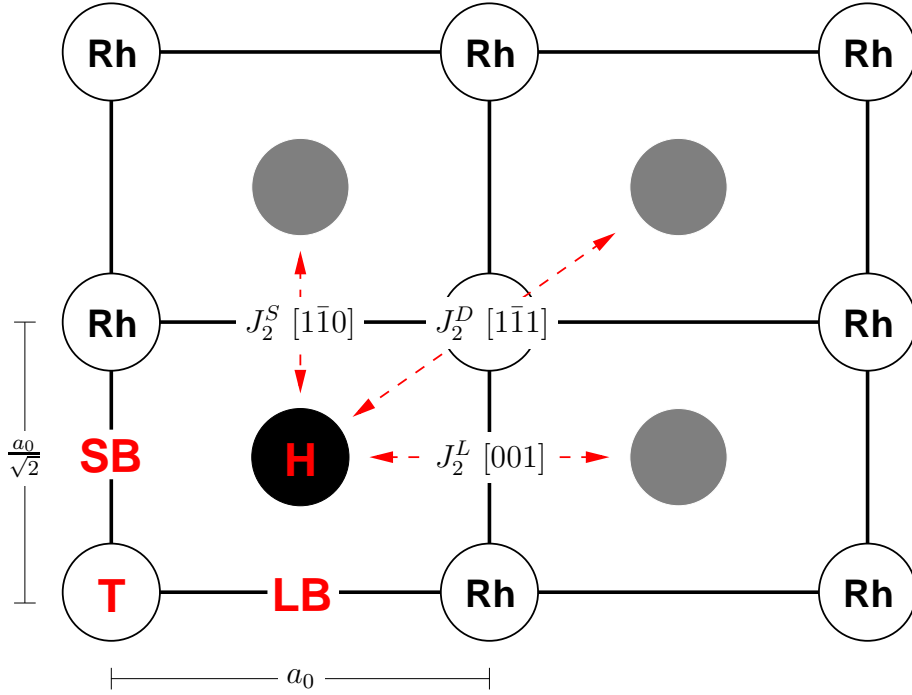


Figure 4.2: Schematic top view of the (110) surface. Red labels indicate the hollow site (H), the top site (T) the short-bridge (SB) and the long bridge (LB) sites. The three couplings $J_2^{S,L,D}$ between coadsorbed Rh adatoms used in the equation (4.2) are also shown.

between adatoms coadsorbed at a distance larger than third neighbours are negligible,³ the parameters of the Hamiltonian can be obtained by fitting equation (4.2) with the binding energies computed at coverages of 0.25, 0.50, 0.75, and 1.00 ML. The results of a least-squares fit are reported in Table 4.4. It results that there is a strong attractive interaction between adatoms coadsorbed along the $[1\bar{1}0]$ direction, whereas the interaction is much weaker, but still attractive, along the $[001]$ and $[1\bar{1}1]$ directions. This model thus suggests that coadsorbed adatoms cluster preferentially along the $[1\bar{1}0]$ direction.

³This corresponds to assuming that the binding energy per adsorbed Rh adatom does not change by reducing the coverage below 0.25 ML.

geometry	coverage (ML)	E_{bind} (eV/atom)
(2 × 2)	0.25	4.64
(2 × 1)	0.50	5.39
(1 × 2)	0.50	4.78
(2 × 2)	0.50	4.77
(2 × 2)	0.75	5.25
(1 × 1)	1.00	5.47

Table 4.3: Binding energies of Rh@Rh(110) at different coverages and different adsorption geometries.

	(eV/atom)
J_1	-4.730
J_2^S	-0.659
J_2^L	-0.049
J_2^D	-0.021
error	0.013

Table 4.4: Couplings of the lattice gas Hamiltonian (equation (4.2)) as obtained by the least-squares fit of the binding energies reported in Table 4.3.

The process in which two neighbouring rows of adatoms pair up is shown in Figure 4.3, where a top view of the Rh(110)-1×2 surface before and after the row-pairing process is depicted. From the lattice-gas Hamiltonian we can estimate that the energy gain resulting from the coupling of two separate $[1\bar{1}0]$ rows is ~ 0.04 eV/adatom. The same information has also been obtained by comparing directly the total energies of the two slabs shown in Figure 4.3, thus obtaining a value of ~ 0.02 eV/adatom. These two estimates agree within the accuracy of our calculations (typical errors are in the range of ~ 0.01 eV), thus confirming the validity of the lattice-gas Hamiltonian.

4.3 Deconstruction process

The first step in the analysis of the deconstruction process consists in the study of the row-pairing process on a (1×2) unit cell. On such a small unit cell what can be studied is not really the row pairing process, but the coherent hop of all the $[1\bar{1}0]$ chains of adatoms. We have identified three non equivalent paths—described in Figure 4.4—leading to an equivalent final state,

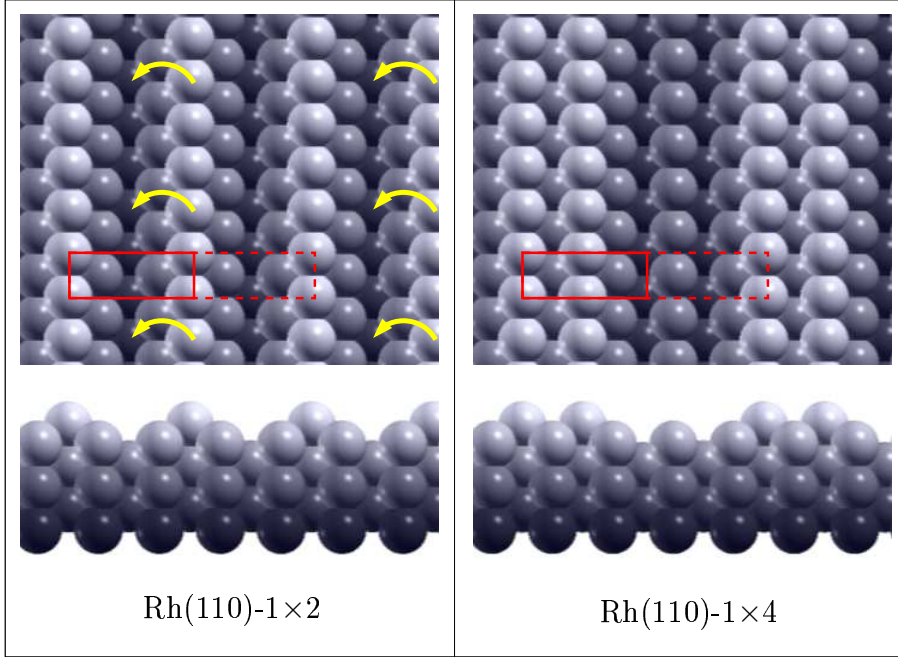


Figure 4.3: Top and side views of the Rh(110)-1 \times 2 surface before (left) and after (right) the row-pairing process. The red rectangles represent the (1 \times 2) and (1 \times 4) surface unit cells.

which we designate *hopping*, *direct-exchange* and *cross-exchange*. In the first case the adatom in the chain jumps from one hollow site to the other passing through the short-bridge saddle point. In the second and in the third cases the adatom exchanges its position with an atom of the second layer. For the *hopping* process we have computed an activation energy per diffusing atom $E_A = 1.66$ eV/cell, for the *direct-exchange* $E_A = 0.93$ eV/cell, while for the *cross-exchange* $E_A = 1.06$ eV/cell. The main result of these calculations is that *exchange*-like paths result to be favoured, a possible explanation being the higher average coordination of the system at the transition state. We point out that the processes considered here consist of a coherent hop of all the $[1\bar{1}0]$ chains of adatoms. Since the chains are infinitely long, however low the activation energy per atom might be, the overall energy barrier for this process will result to be infinitely high. For a row of finite length the energy barrier is proportional to the number adatoms that hop simultaneously. In the case of a row of N atoms, our calculations show that the overall activation energy cannot be lower than $N \cdot 0.93$ eV, this estimate being valid for $N \gg 1$. The experimental indication of an activation energy of 0.95 eV leads to exclude the processes in which many atoms of a row perform a coherent

hop, suggesting that point defects must be involved in the deconstruction process.

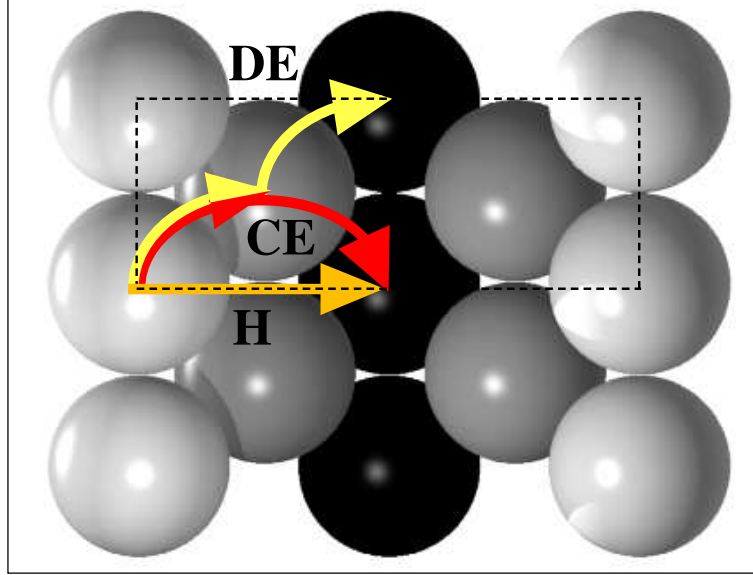


Figure 4.4: Top view of the three possible diffusion mechanisms described in the text: (DE) direct-exchange, (CE) cross-exchange and (H) hopping.

We have then considered the same row pairing process on a (1×4) unit cell. As shown in Figure 4.3, this represents the smaller system in which the row pairing can be studied, but again the results are activation energies per hopping atom and cannot be directly compared with the experimental estimate. In this case the three possible paths described above give, respectively, $E_A = 1.65$ eV/cell (*hopping*), $E_A = 0.87$ eV/cell (*direct-exchange*) and $E_A = 1.06$ eV/cell (*cross-exchange*). It is worth noticing that the differences in the activation energies with respect to the results obtained for the same paths on the (1×2) unit cell are within the accuracy of our calculations (0.1 eV for the activation energies). The relevance of these results stems from proving that the activation energy for the deconstruction process, which in principle should be computed on a $(n\times 4)$ unit cell, can instead be evaluated (within the uncertainty of 0.1 eV) on the smaller $(n\times 2)$ unit cell. Moreover, since *cross-exchange* path gives roughly the same activation energy as the *direct-exchange* one, in the following we shall consider only the *hopping* and the *direct-exchange* paths (hereafter simply called *exchange*).

As explained before, an important point to be addressed for understanding the thermal stability of the (1×2) phase is the thermodynamics and the kinetics of the creation of a defect that breaks a perfect row. This because

the coherent hop a large portion of row is characterised by an energy barrier much higher than the experimental estimate. For this purpose we consider a perfect (1×2) surface whose deconstruction proceeds through the formation of a vacancy in one of the $[1\bar{1}0]$ added rows and the corresponding creation of an adatom in one of the adjacent missing rows. This process has been modelled using a (3×2) unit cell, so that the interaction between defects in the periodically repeated images of our slab is expected to be negligible.

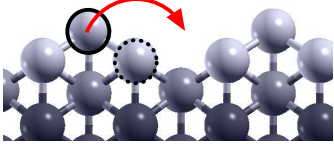
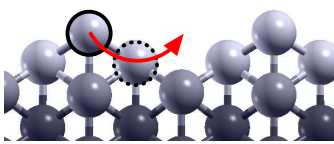
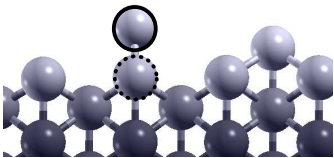
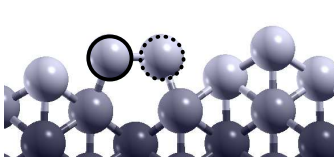
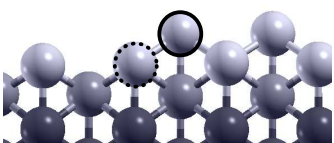
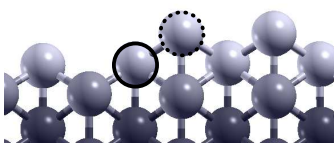
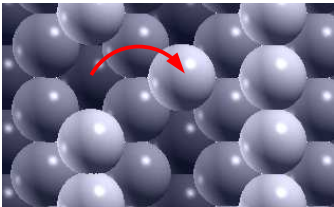
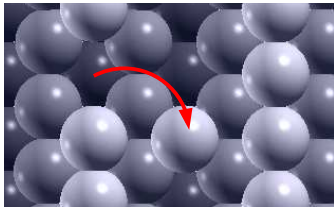
	hopping	ΔE	exchange	ΔE
I		0.00		0.00
TS		2.56		2.03
F		1.09		0.99
				

Figure 4.5: Schematic views of the hopping and exchange deconstruction processes: the initial state (I), the transition states (TS) and the final states (F) are described. ΔE is the energy difference (in eV) between each state and the initial state of the same process. The bottom panels show a top view of these processes.

The formation of a vacancy can again occur via the two distinct *hopping* and *exchange* paths described above and which are depicted in detail in Figure 4.5. The two processes are obviously endothermic: the final state of a single hop lies 1.09 eV above the initial state (with a forward transition barrier of 2.56 eV), while the final state of a single exchange lies 0.99 eV above the

perfect (1×2) surface (with a forward transition barrier of 2.03 eV). However, for both processes the activation energy is not compatible with the value of $E_A=0.95\pm0.13$ eV extracted from the Arrhenius fit to the experimental data. We conclude that, whatever the deconstruction mechanism might be, its ignition must occur in the neighbourhood of defects already present at the reconstructed surface.

In order to investigate the role of surface defects in the deconstruction process, we have considered the process in which a Rh atom, sitting at an added row next to an already existing vacancy, jumps to a neighbouring missing row (the process $S_1 \rightarrow S_2$ described in Figure 4.6). In this case,

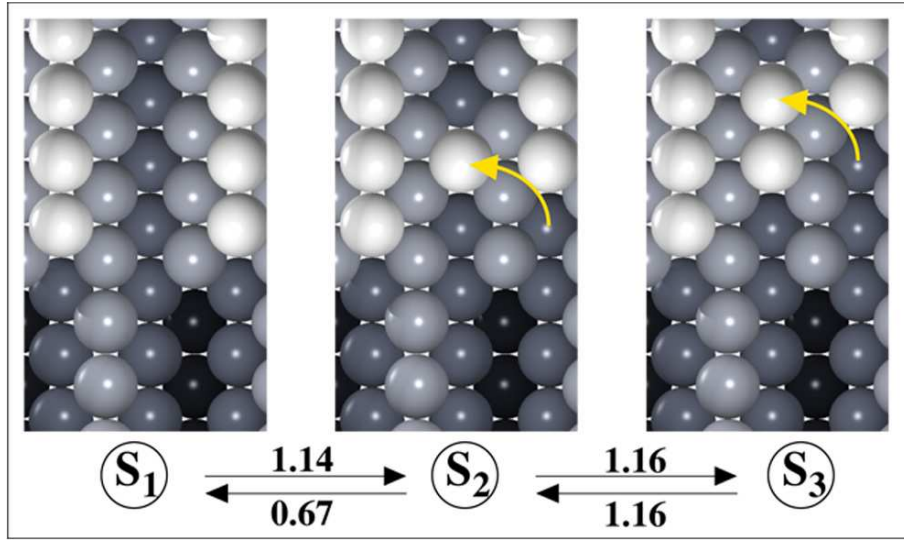


Figure 4.6: Individual defect-mediated deconstruction mechanism and resulting activation energies (eV).

only the *exchange* mechanism has been explicitly considered, for it is much favoured in the case of a perfect surface. The calculated forward activation energy is 1.14 eV, compatible with the experimental value of the activation energy for the surface deconstruction process. The final state of the process, S_2 , has an energy 0.47 eV higher than the initial state, resulting in a barrier for the reverse process $S_1 \leftarrow S_2$ of 0.67 eV. This is due to a larger strength of the bond between Rh atoms within the same row (J_2^S) than between atoms in adjacent rows ($J_2^{L,D}$). Once the deconstruction has been ignited by the process $S_1 \rightarrow S_2$, it will proceed either through the diffusion of the adatom in the missing-row, or through the direct pairing of two adjacent rows resulting by the incremental build-up of an atomic row in the missing row through. In the former case, the diffusion of the isolated adatom proceeds until it stops at

the foot of a step or it clusters with other adatoms found on its way through the missing-row.⁴ In the latter case, instead, row pairing would proceed via elementary steps such as the $S_2 \rightarrow S_3$ process depicted in Figure 4.6, in which an atom leaves the added row jumping next to a previously moved atom. The calculated diffusion barrier along the missing-row is 0.70 eV, very close to the backward activation energy for the $S_1 \rightarrow S_2$ process (0.67 eV), indicating that once an adatom has been shifted to the missing row, it will, with equal probability, either recombine with the vacancy left behind or diffuse away. The calculated activation energy for the $S_2 \rightarrow S_3$ process is 1.16 eV, comparable to that of the first jump, which ignites the deconstruction ($S_1 \rightarrow S_2$, 1.14 eV), and much larger than the diffusion barrier (0.7 eV) or the backward $S_1 \rightarrow S_2$ barrier (0.67 eV) discussed above.⁵ We thus infer that the direct pairing of adjacent added rows is unfavoured with respect to a deconstruction mechanism in which added rows would crumble starting from surface defects (*e.g.* steps) and the isolated adatoms thus produced would diffuse along missing-rows until they cluster or are blocked at the foot of a step. When either these final states are reached, the number of in-row bonds increases by one, thus lowering the surface energy slightly below the initial value corresponding to the S_1 state.

This first-principles study of the microscopic mechanisms characterising the initial stages of the deconstruction process confirms that the perfect (1×2) phase of Rh(110) is extremely stable, but it also indicates that the presence of surface defects opens new low-barrier deconstruction pathways which significantly decrease the thermal stability of the surface. This is compatible with STM results according to which the first steps of the structural rearrangement involve the presence of surface defects [34]. This scenario is further supported by the good agreement between the theoretical (1.14 ± 0.1 eV) and the experimental results (0.95 ± 0.13 eV) for the activation energy of defect mediated deconstruction.

⁴In this case our lattice-gas Hamiltonian indicates that the energy gain is ~ 0.65 eV.

⁵Note that the barrier for the backward $S_2 \leftarrow S_3$ process is equal to that for the forward one because the number of in-row bonds is the same in the initial and in the final states.

Chapter 5

Early stages of graphitisation of the Ni(111) surface

In this chapter I present some preliminary results of the study of the adsorption and diffusion of carbon atoms and small clusters on the Ni(111) surface. This work, done in collaboration with D. Alf   and S. Baroni, is aimed at understanding the early stages of graphitisation of the Ni(111) surface.

Many catalytic processes suffer from unwanted side reactions leading to low selectivity or poisoning of the catalyst. A very important example is the catalytic dehydrogenation of hydrocarbons. Nickel is a catalyst widely used for the dissociation of hydrocarbons because of the favourable efficiency/price ratio. For instance, in the steam reforming process, methane (CH_4) is dissociated on the surface of nickel nanoparticles. Molecular hydrogen (H_2) is formed and the remaining carbon reacts with water to form additional molecular hydrogen and carbon monoxide (CO). Carbon may be present on the nickel surface in two forms: a *carbide* phase, characterised by unsaturated C $2p_z$ orbitals, and a *graphitic* phase. The presence of the two species can be experimentally distinguished on the basis of the KVV Auger-line shape. Carbide carbon forms at temperatures below ~ 600 K and is the active carbon species participating in the catalytic process. In the carbide phase at coverages higher than 0.2 ML, the surface atoms are found to rearrange into an almost square surface mesh with a $(\sqrt{39} \times \sqrt{39})R16.1^\circ$ “clock” reconstruction [41] which is quite similar to that observed on the Ni(001) surface [42]. At temperatures beyond 700 K, graphitic carbon forms, which results in a loss of reactivity and therefore leads to a poisoning of the catalyst. A recent scanning tunnelling microscopy (STM) study of the decomposition of ethylene (C_2H_4) on the Ni(111) surface at temperatures below that required for the

formation of graphitic carbon [43] has shown that the carbon is dispersed on the surface as an isolated state or as a string-like structure without forming islands of reconstructed single domains of the $(\sqrt{39} \times \sqrt{39})R16.1^\circ$ structure.

The temperature dependence of the reactivity of carbon present on the surface of the nickel catalyst has important consequences. Indeed, the industrial processes that involve the dissociation of hydrocarbons run at high temperature and are most convenient if the carbon-to-oxygen ratio is as close to stoichiometric as possible. Under such severe conditions graphitic carbon forms. The carbon buildup on the nickel surface blocks the active sites, thus lowering the efficiency and eventually leading to a total breakdown of the catalyst. A partial solution of the problem has been proposed by F. Besenbacher *et al.* [44], consisting in the addition of a small amount of gold (0.5 wt %) to the nickel surface. High-activity sites are blocked by coordination with gold atoms, retarding carbon nucleation and, to a lesser extent, the reformation process. This procedure, however is not sufficient to eliminate the formation of graphitic carbon.

The efficiency of nickel in the dissociation of hydrocarbons has also been recently exploited for the growth of carbon nanofibres [45]. Carbon nanofibres have been observed to develop through a reaction-induced reshaping of the nickel nanoparticles. DFT calculations performed on the (111) and (211) surfaces [45] have suggested that the rate limiting step for the nanofibre growth is the surface transport of C atoms away from steps, where the dissociation of methane is more favourable, to the graphene/Ni(111) interface. The overall activation energy for adding a carbon atom to a pre-existing graphene overlayer has been estimated to be 1.6 eV, in agreement with the experimental estimates (1.5-1.7 eV). In spite of these advances, the understanding of the microscopic growth mechanism of a graphene layer on nickel surfaces is still incomplete. In particular, the early stages of the nucleation process leading to the formation of graphene islands are not yet clear.

In order to shed light on this topic, we have performed first principles calculations of the adsorption of carbon at the (111) surface of nickel. In particular we have studied the formation and diffusion of small carbon clusters (such as dimers, trimers, up to the hexamer) that are expected to play an important role in the nucleation process. Our preliminary results seem to suggest that, in agreement with the experimental findings of Nakano *et al.* [43], the formation on a graphene island is unfavoured with the respect to growth of carbon filaments.

5.1 Nickel (111) surface

A detailed description of the methodology used in our first-principles calculations is reported in Appendix A. The (111) nickel surface has been modelled by four layer slabs; the bottom layer was kept fixed at the bulk truncated structure and the others were left free to relax so as to minimise the surface energy. Brillouin zone integration has been performed using a $(9 \times 9 \times 1)$ Monkhorst-Pack mesh for the (1×1) surface unit cell and equivalent meshes for the larger unit cells. The bulk and the surfaces of nickel are known to be magnetic. For this reason we have performed all the calculations in the local spin density approximation (LSDA-GGA). The equilibrium lattice constant, a_0 , and the bulk modulus, B_0 , of nickel have been determined as explained in the previous chapter in the case of rhodium. For a_0 we have obtained a value of 6.66 bohr, in excellent agreement with the experimental result (6.66 bohr [46]). For the bulk modulus B_0 and for the magnetic moment μ we have obtained, respectively, 2.02 Mbar and $0.64 \mu_B/\text{cell}$, in good agreement with the experimental values of 1.86 Mbar and $0.61 \mu_B/\text{cell}$ [47, 48]. In Figure 5.1 a schematic top view of the (111) surface of a fcc crystal is depicted. Blue and red circles represent, respectively, the hcp and fcc three-fold hollow sites, while the vertexes of the lattice represent the top sites. Hcp hollow sites differ from the fcc ones for the presence of a Ni atom in the underlying layer. The (1×1) , (2×2) and (3×3) surface unit cells used in this work are depicted with dashed lines. Figure 5.1 shows that the hollow sites are located on a triangular lattice of side 1.44 \AA , very close to the lattice constant of a graphene sheet (1.43 \AA).

5.2 Carbon adsorption: the carbidic phase

We have first considered the properties of the carbidic phase, i.e. the binding of isolated carbon atoms on the (111) surface of nickel. Carbon atoms are assumed to result from the complete dehydrogenation of hydrocarbons (methane, for instance). Possible adsorption sites are the top, the bridge, the fcc and the hcp threefold-hollow. Our calculations indicate that only the two hollow sites are stable, with the carbon slightly more bound at the hcp (0.04 eV at a coverage of $1/9 \text{ ML}$). The results are reported in Table 5.1. It is evident that there is sizable reduction of the binding energy in going from low ($1/9 \text{ ML}$) to high coverage (1 ML), with an energy difference of $\sim 1.7 \text{ eV}$. We have also verified that the effects of spin polarisation are relevant. The estimated error in the binding energy resulting from neglecting such effects is $\sim 0.1 \text{ eV}$. The modification of the magnetic structure of the

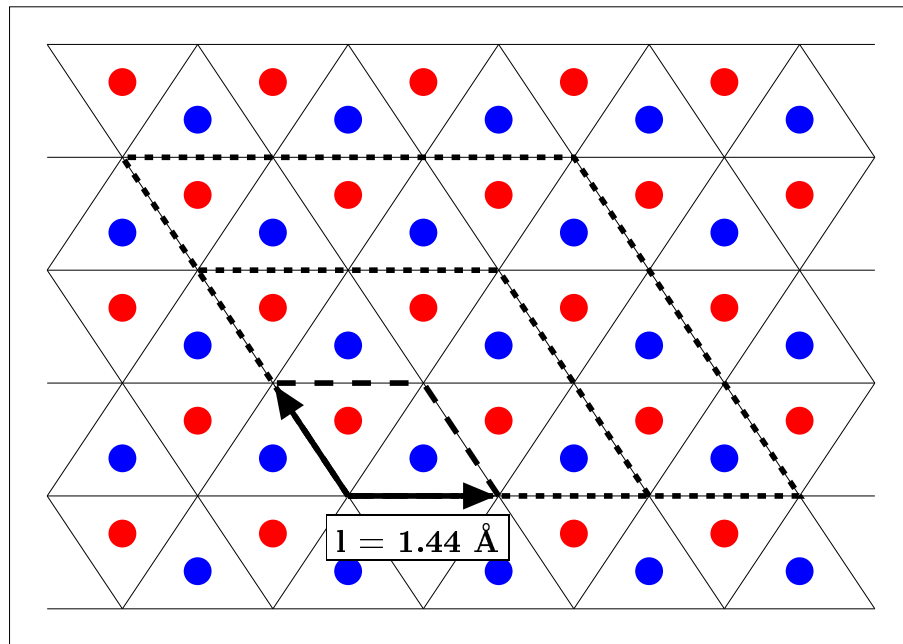


Figure 5.1: Top view of the (111) surface of a fcc crystal. Red and blue dots represent, respectively, the fcc and hcp three-fold hollow sites. The (1×1) , (2×2) , and (3×3) surface unit cells used in this work are depicted with dashed lines.

	1/9 ML	1 ML	1 ML (non magnetic)
hcp hollow	6.67 (eV/C)	4.92 (eV/C)	—
fcc hollow	6.63 (eV/C)	4.92 (eV/C)	5.01 (eV/C)

Table 5.1: Binding energies of the carbon atom on the two adsorption sites (hcp and fcc hollow sites) at different coverages. The binding energy of a carbon atom adsorbed at the fcc hollow site (1 ML), obtained neglecting the spin polarisation, is reported as a reference.

Ni(111) surface resulting from the adsorption of carbon at high coverage (1 ML) is shown in Figure 5.2, where the planar average of the spin polarisation ($\zeta(z) = \int \frac{\rho_{\uparrow} - \rho_{\downarrow}}{\rho_{\uparrow} + \rho_{\downarrow}} dx dy$) is plotted as a function of z . The black line represents the polarisation of the clean Ni(111) surface; the red and the green lines refer to carbon adsorption at the hcp and fcc sites. The orientation of the carbon magnetic moment is opposite to that of the Ni surface, resulting from an anti-ferromagnetic coupling; the magnetisation of the first Ni layer is reduced to zero.

The carbon diffusion has been studied by searching the MEP that connects the hcp and the fcc sites in the limit of low coverage (1/9 ML). The resulting energy profile is depicted in Figure 5.3, together with a top view of the two end states and of the transition state. In general, the diffusion of adsorbates on the (111) surface occurs by crossing the bridge site without a considerable deformation of the substrate. This is not the case of carbon. Indeed, as can be seen from Figure 5.3, the propensity of carbon to increase its coordination induces a strong deformation of the substrate, resulting in an increase of the Ni²-Ni⁴ distance by 0.37 Å and a contraction of the Ni¹-Ni³ distance by 0.44 Å. At the transition state the carbon stays in a sort of fourfold hollow site and the surface geometry closely resembles the clock reconstruction induced by C adsorption on the (001) facet of nickel [42]. The red dashed curve in Figure 5.3 represents the elastic contribution to the energy barrier. In order to estimate the elastic energy (E_{elastic}) we have removed the carbon atom from the surface and computed the total energy of this structure with the metal atoms kept frozen at the positions they would have in presence of a carbon impurity. E_{elastic} is thus given by the difference between the total energies of this “frozen” slab and that of the clean surface:

$$E_{\text{elastic}} = E_{\text{frozen surface}} - E_{\text{clean surface}} \quad (5.1)$$

This procedure has been followed for all the images of the path. The elastic energy thus defined corresponds to the work required to deform the nickel

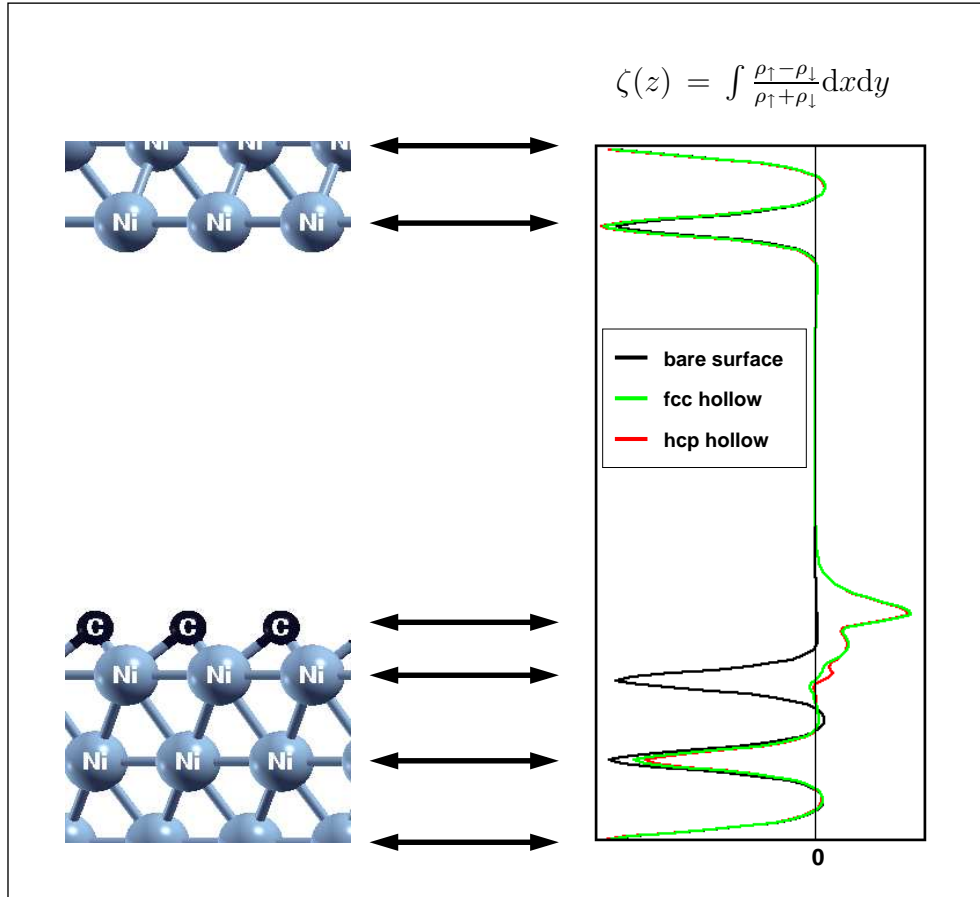


Figure 5.2: Planar average of the spin polarisation plotted as function of z . The black line represents the polarisation of the bare Ni(111) surface; the red and the green lines describe the effect of the carbon adsorption in the hcp and fcc sites.

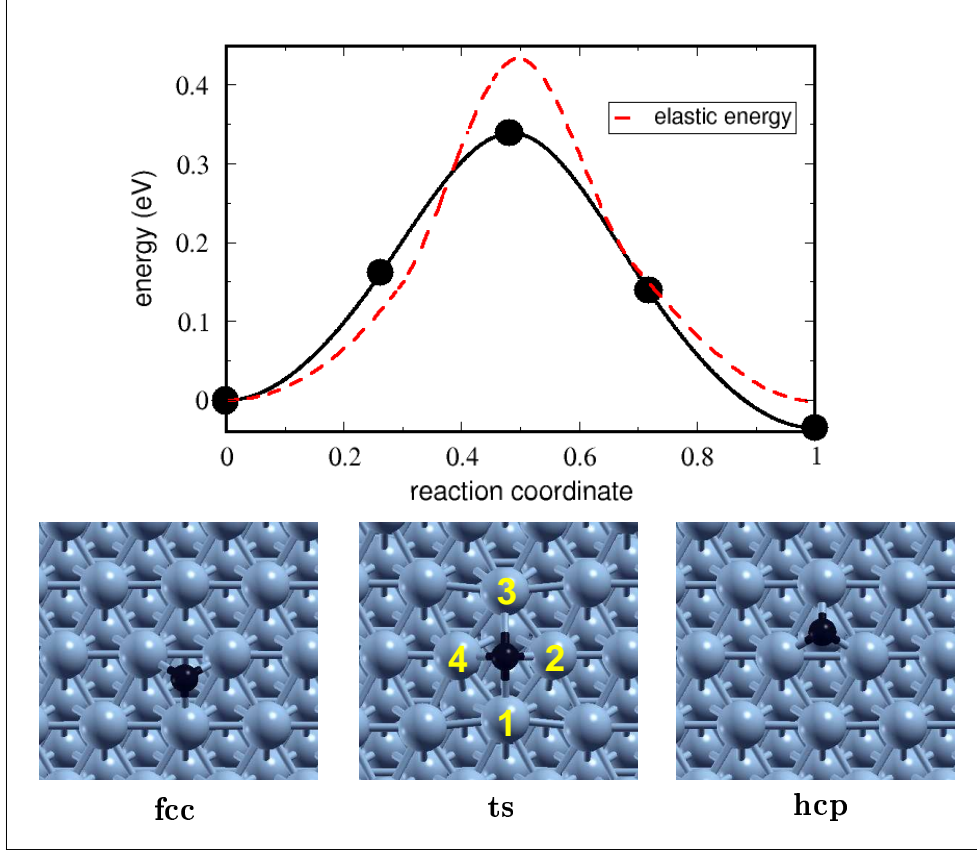


Figure 5.3: Energy profile for the carbon diffusion on the Ni(111) surface. The red curve corresponds to the contribution given by the elastic deformation of the substrate to the energy barrier (see text). In the lower panels a top view of the two end states and of the transition state is shown.

substrate; by definition, it is always positive. In Figure 5.3 is evident that the elastic energy at the transition state is even larger (by 0.1 eV) than the overall energy barrier. We can thus conclude that the bonding of carbon with the substrate is stronger at the transition state than at the two end states, but not enough to compensate the energy paid for the large substrate deformation. This result is in agreement with the experimental observation that, in the carbidic phase at coverage above 0.2 ML, the surface atoms are found to rearrange into an almost square surface mesh with a $(\sqrt{39} \times \sqrt{39})R16.1^\circ$ “clock” reconstruction [41]. Indeed, at high coverage, the cost for the elastic deformation of the nickel substrate is compensated by the energy gain due to the stronger binding of carbon. Unfortunately, because of the large unit cell required to describe the $(\sqrt{39} \times \sqrt{39})R16.1^\circ$ structure, we cannot verify

directly the correctness of this model. Our estimate of the energy barrier for carbon diffusion is ~ 0.35 eV, in good agreement with the experimental value of 0.3 eV obtained for polycrystalline Ni [49]. The slightly larger value (~ 0.5 eV) computed by Helveg *et al.* [45] is probably the result of the smaller supercell and thinner slab used in their calculation. Indeed, using a 3-layer slab and a (2×2) surface unit cell,¹ we have obtained an energy barrier of 0.5 eV, in agreement with the value obtained by Helveg *et al.*

5.3 Graphene nucleation: the graphitic phase

The rather low energy barrier for carbon diffusion suggests that this process is extremely rapid, especially at the high temperatures required for the formation of graphene (~ 700 K). It is thus reasonable to expect the frequent occurrence of two body processes in which adsorbed carbon atoms collide, giving rise to a dimer. A top view of this reaction and of the corresponding energy profile are depicted in Figure 5.4. The C atoms are initially placed in fcc hollow sites at a distance of 4.32 \AA and the process proceeds in three hops. After each hop the energy increases as a consequence of the substrate-mediated interaction between the C atoms. The bottleneck for the whole reaction is given by the last energy barrier and the overall activation energy is estimated to be 1.02 eV.² With a binding energy of 6.93 eV/C, the dimer is 0.26 eV/C more stable than the isolated C atom; the formation of a dimer is thus an exothermic process (0.52 eV per carbon dimer). The C-C distance is 1.35 \AA , to be compared with 1.31 \AA for the C-dimer in the vacuum and much shorter than the distance between neighbouring hollow sites (1.44 \AA). We have also calculated that the dimer diffusion is hindered by an energy barrier of 0.59 eV, much lower than the barrier that has to be overcome to create it. This suggests that, when the temperature is high enough to allow the dimer formation, the dimer diffusion is facile.

In the perspective of understanding the nucleation of a graphene layer it is natural to consider the stability of trimers, tetramers, pentamers and, finally, of a carbon ring (an hexamer). Since carbon atoms have to lie on the triangular lattice shown in Figure 5.1, there is just one possible configuration

¹The same system considered by Helveg *et al.* in [45].

²The exact value of the forward activation energy depends on the energy of the configuration chosen as starting point. Here we want to calculate the energy barrier as seen from a pair of C atoms placed at infinite distance. The energy of the initial configuration used in our calculations is 0.12 eV higher than the energy computed for C atoms at coverage of $1/9$ ML and has thus been corrected. This correction reflects on the forward activation energy for the dimer formation, resulting in an increase of 0.12 eV.

for the trimer. On the contrary, three different tetramer structures are possible. Again, for the pentamer a number of different structures is possible, but we have considered only the one that can lead to the formation of the carbon ring. A top view of all these structures is depicted in Figure 5.5 and the relative binding energies are summarised in Table 5.2. It is worth noticing that

	E_B (eV/C)	N_C	N_{Ni}	N_{C-C}	N_{C-Ni}
monomer	6.67	1	3	0	3
dimer	6.93	2	4	1	6
trimer	6.92	3	5	2	7
tetramer “moon”	6.82	4	6	3	12
tetramer “star”	6.72	4	6	3	12
tetramer “snake”	6.97	4	6	3	8
pentamer	6.75	5	7	4	15
hexamer	6.76	6	7	6	18

Table 5.2: Binding energies of all the carbon clusters considered in this work. N_C represents the number carbons that form the cluster and N_{Ni} is the number of nickel surface atoms involved. N_{C-C} and N_{C-Ni} are, respectively, the numbers of carbon-carbon and carbon-nickel bonds.

the binding energy per carbon atom is roughly the same for dimers, trimers and elongated tetramers (the “snake” configuration depicted in Figure 5.5). This can be explained on the basis of the data reported in Table 5.2. Indeed, all these elongated structures share the property that the ratio between the number of carbon-nickel bonds (N_{C-Ni}) and the number of surface nickel atoms involved in the bonding (N_{Ni}) is minimum, becoming closer to 1 as the length of the cluster increases. This means that the average coordination of the surface nickel atoms is lower than for the other structures so that each carbon-nickel bond is stronger. The tetramer “star” is the less stable structure; it has a rather peculiar tetrahedral geometry in which the central carbon atom is detached from the surface, being 0.43 Å higher than the other carbon atoms. The “moon” tetramer, the pentamer and the hexamer are all considerably less stable than the corresponding elongated clusters. This behaviour is probably due to the presence of an over-coordinated central nickel atom, shared by all the carbon atoms. On the basis of these results carbon is expected to grow in the form of elongated filaments, any new ramification having an energy cost of ~ 0.55 eV.

The analysis of many possible reaction pathways that may lead to the formation of these structures confirms this picture. The activation energy that hinders the addition of a carbon atom to an elongated cluster (the formation

of trimer and tetramer “snake” structures) is ~ 1.1 eV, comparable with the activation energy for the dimer formation. On the contrary, the overall energy barrier for the formation of the hexamer is 1.85 eV, considerably larger than all the other barriers taken into account. The diffusion of trimers and of larger clusters has not been taken into account because the energy barriers for these process are expected to be large and thus they are supposed to be of secondary importance in the growth process. These results indicate that the two structures that, in principle, should be the building blocks of the graphene layer (*i.e.* the tertamer “star” and the carbon ring) are both thermodynamically unfavoured with respect to dimers, trimers and other elongated filaments. Moreover the formation of the carbon ring is hindered by a considerable energy barrier. The energetics of the processes studied in this work is summarised in Figure 5.6, where the case of the formation of an hexamer, starting from six carbon monomers, is considered.

This scenario is in agreement with the experimental findings of Nakano and coworkers [43] who have observed the formation of string-like structures on the nickel surface after exposure to 0.2 L of C_2H_4 at 614 K (see Figure 5.7). The filaments form angles of $\sim 120^\circ$ and are thus commensurate with the (111) substrate.

5.4 Perspectives

The results presented in the previous section seem to indicate that the nucleation of a graphene island is, at least at low temperature, unfavoured with respect to the growth of elongated carbon filaments. However it is not clear what the impact of entropic effects might be. Indeed, the fact that the formation of graphitic carbon is observed at temperatures beyond 700 K indicates that the effects of temperature on the thermal stability of the structures considered cannot be neglected. The possibility of studying the evolution of the system as a function of the temperature and on macroscopic time scales would allow for a deeper understanding of the growth mechanism.

For these reasons, we are considering the possibility of using the information obtained from first-principles calculations to perform kinetic Monte-Carlo (KMC) simulations. Indeed, once a database of all the possible configurations and energy barriers is available, the reaction rates can be computed using the harmonic TST described in the first chapter. With these ingredients, a simulation of the long-time evolution of the system based on the KMC scheme should be straightforward.

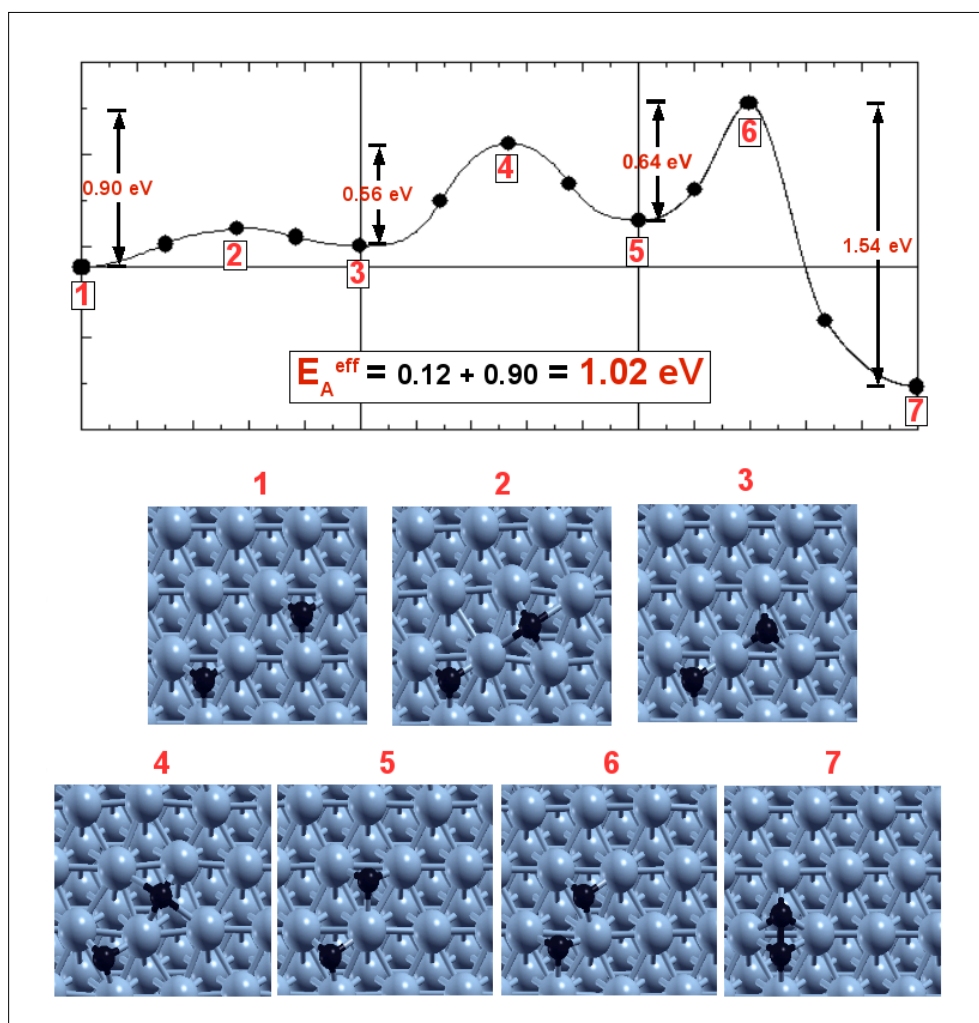


Figure 5.4: Energy profile of the multi-step pathway that leads to the dimer formation. The lower panels describe a top view of the stable configurations and transition states along the reaction pathway.

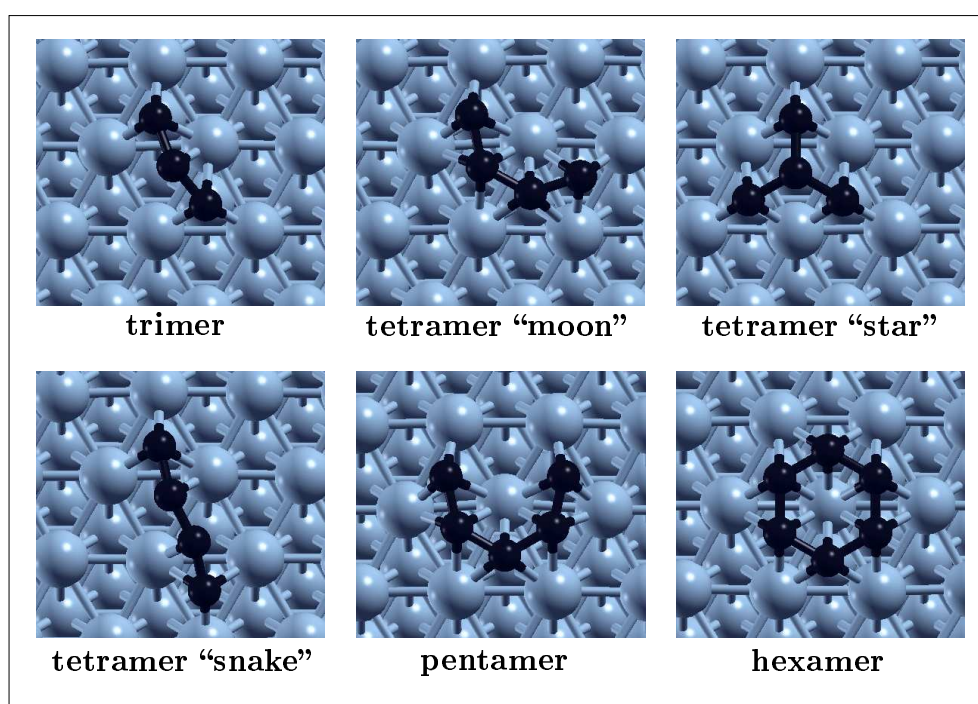


Figure 5.5: Top view of the structures described in the text.

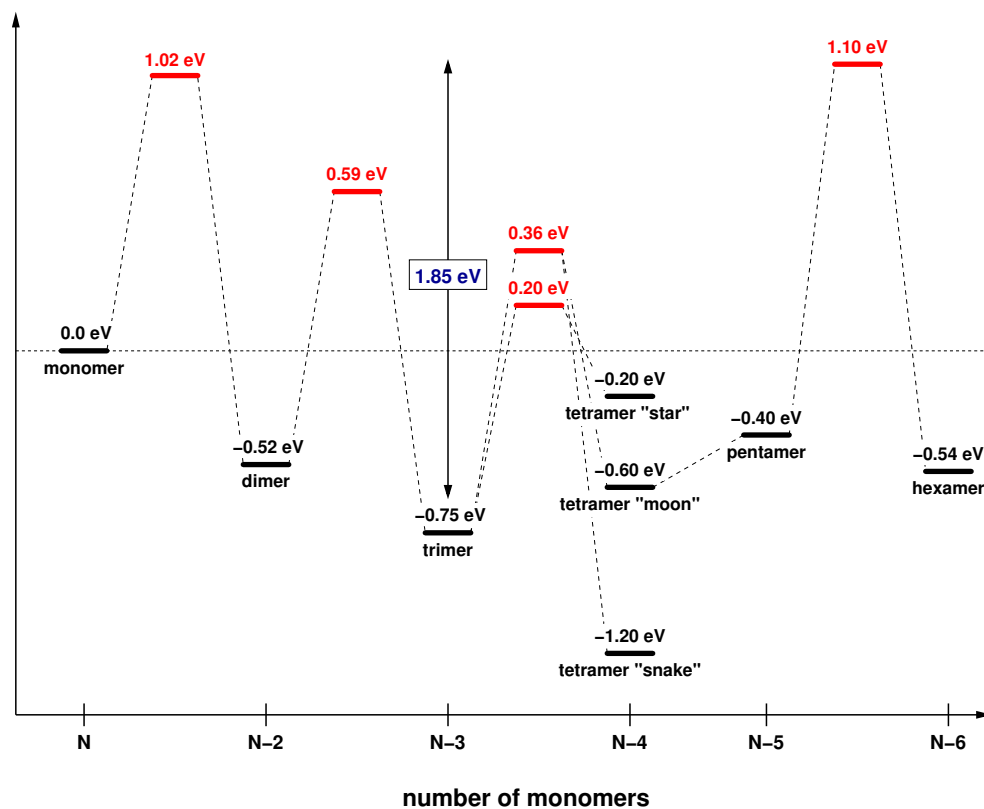


Figure 5.6: Energetics for the formation of a carbon ring (hexamer) starting from six carbon monomers.

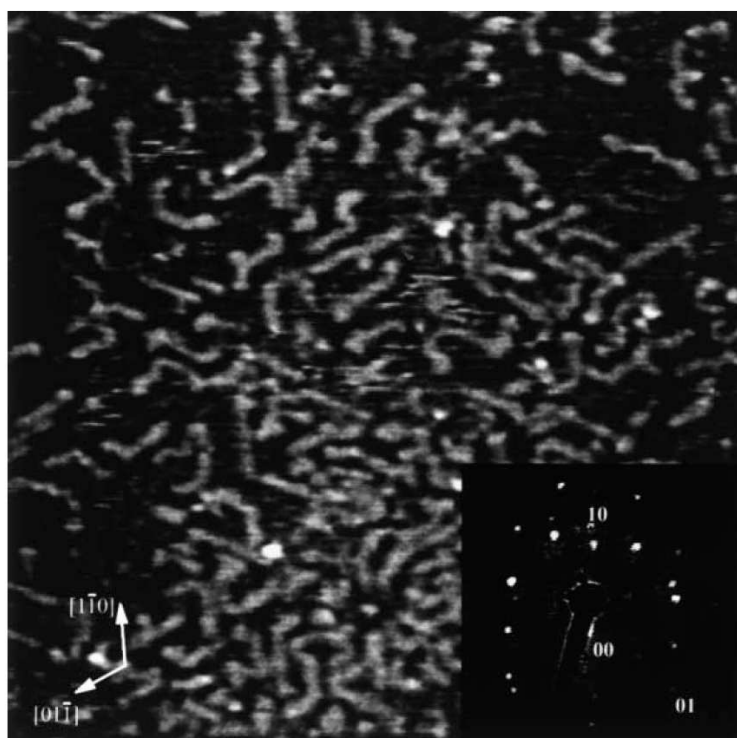


Figure 5.7: STM image of C/Ni(111) surface after exposure to 0.2 L of C_2H_4 at 614 K ($158 \times 158 \text{ \AA}^2$). Inserted is a LEED pattern of the surface. It is evident the presence of string-like structures [43].

Chapter 6

Overview of other works from the author

In this chapter I present a short description of all the works, that I have contributed, in which the various implementations of NEB, presented in Chapter 2, have been used.

- **Adsorption of methylchloride on Si(100) from first principles,**

A. H. Romero, C. Sbraccia, P. L. Silvestrelli, and F. Ancilotto;
published in J. Chem. Phys. 1085, **119** (2003).

Abstract:

The chemisorption of methylchloride (CH_3Cl) on Si(100) is studied from first principles. We find that, among a number of possible adsorption configurations, the lowest-energy structure is one in which the methylchloride molecule is dissociated into CH_3 and Cl fragments which are bound to the two Si atoms of the same surface dimer. Our calculations show that dissociative chemisorption of methylchloride on Si(100) may proceed along different reaction paths characterised by different energy barriers that the system must overcome: some dissociation processes are mediated by a molecular precursor state and, at least in one case, we find that the dissociation process is non activated, in agreement with recent experimental findings. We have also generated, for many possible adsorption structures, theoretical scanning tunnelling microscopy images which could facilitate the interpretation of experimental measurements.

- **Theoretical Study of Toluene Chemisorption on Si(100),**

F. Costanzo, C. Sbraccia, P. L. Silvestrelli, and F. Ancilotto;

published in J. Phys. Chem. B 10209, **107** (2003).

Abstract:

The chemisorption of toluene (C_7H_8) on the Si(100) surface is studied using first-principles and semiempirical methods. We find that the most stable configuration is a dissociated one, in which a C-H bond of the methyl group is cleaved and the loose hydrogen is bonded to the silicon surface; a detailed analysis based on the use of the maximally localised Wannier functions indicates that this process can be described as a proton abstraction reaction. Several other stable geometries involving both undissociated and dissociated toluene molecules have been found and studied. Although most of them resemble those of benzene on Si(100), some differences have been detected, which mainly reflect the role of the electron-donating, substituent methyl group of toluene. Possible reaction pathways leading from one stable adsorption configuration to another and to the dissociation of the toluene molecule on the Si surface have been investigated; in particular the one involving the abstraction of a proton from the methyl group has been found to be activated, with an energy barrier of about 1.4 eV. Our results are compared with recent experimental measurements.

- **Adsorption of 3-pyrroline on Si(100) from first principles,**

A. H. Romero, C. Sbraccia, and P. L. Silvestrelli;

published in J. Chem. Phys. 9745, **120** (2004).

Abstract:

The chemisorption of 3-pyrroline (C_4H_7N) on Si(100) is studied from first principles. Three different structures can be realized for which, depending on the temperature, the chemisorption process is facile (for two of them it is essentially barrierless). Among these configurations the most favoured one, from a thermodynamical point of view, is a dissociated structure obtained through an exothermic reaction characterised by the formation of a N-Si bond and a H-Si bond in which the H atom is detached from the molecule. Several other chemisorption structures are possible which, however, require overcoming a significant energy barrier and often breaking multiple bonds. A number of reaction paths going from one stable structure to another have been investigated. We have also generated, for the two basic adsorption structures, theoretical scanning tunnelling microscopy images which could facilitate the inter-

pretation of experimental measurements, and we propose a possible reaction mechanism for nitrogen incorporation.

- **Chemisorption sites and reaction pathways for acetylene on Si(111)-(7×7),**

C. Sbraccia, C. A. Pignedoli, A. Catellani, R. Di Felice, P. L. Silvestrelli, F. Toigo, F. Ancilotto, and C. M. Bertoni;

published in Surf. Science 80, **557** (2004).

Abstract:

The interaction between the acetylene molecule (C_2H_2) and the Si(111)-(7×7) surface is studied using both first principles and semi-empirical methods. Several possible chemisorption configurations are explored, which may be helpful to rationalise recent experimental results. The kinetics of the chemisorption process is also studied by means of accurate ab initio calculations, and low-energy paths leading to stable configurations are identified. It is shown that large-scale calculations based on the use of semi-empirical potentials, in tight cooperation with ab initio calculations, can be an efficient tool to achieve a broad overview of the chemisorption reactions of molecules occurring on complex semiconductor surfaces.

- **Engineering the Reactivity of Metal Catalysts: A Model Study of Methane Dehydrogenation on Rh(111),**

A. Kokalj, N. Bonini, C. Sbraccia, S. de Gironcoli, and S. Baroni;

published in JACS 16732, **126** (2004)

Abstract:

The first two steps of methane (CH_4) dissociation on Rh(111) have been investigated using density-functional theory, focusing on the dependence of the catalyst's reactivity on the atomic coordination of the active metal site. We find that, although the barrier for the dehydrogenation of methane ($CH_4 \rightarrow CH_3 + H$) decreases, as expected, with the coordination of the binding site, the dehydrogenation of methyl ($CH_3 \rightarrow CH_2 + H$) is hindered at an adatom defect, where the first reaction is instead most favoured. Our findings indicate that, if it were possible to let the dissociation occur selectively at adatom defects, the reaction could be blocked after the first dehydrogenation step, a result of high potential interest for many dream reactions such as, for example, the direct conversion of methane to methanol.

- **Thermal stability of atomic chains on a metal surface: real-time core-level spectroscopy and ab initio modeling of Rh(110),**

A. Baraldi, S. Lizzit, F. Bondino, G. Comelli, R. Rosei, C. Sbraccia, N. Bonini, S. Baroni, A. Kikkelsen, and J. N. Andersen;

submitted to PRB.

Abstract:

The thermal stability of the (1×2) missing-row phase of Rh(110), whose first layer is an ordered array of one-dimensional atomic chains, is investigated using high-resolution core-level spectroscopy and density functional calculations. The time evolution of the spectra indicates that this phase is metastable towards the deconstruction into a (1×1) phase. Our calculations unveil the mechanism of this process, which is shown to be ignited by surface defects and provide a value for the activation energy in good agreement with experimental findings.

- **Energetically Driven Reorganization of a Modified Catalytic Surface under Reaction Conditions,**

A. Locatelli, C. Sbraccia, S. Heun, S. Baroni, and M. Kiskinova;

accepted for publication in JACS.

Abstract:

The compositional and structural rearrangements at the catalyst surface during chemical reactions are issues of great importance for understanding and modelling the catalytic processes. Low-energy electron microscopy and photoelectron spectromicroscopy studies of the real-space structure and composition of a Au-modified Rh(110) surface during water formation reveal reorganisation processes due to Au mass transport triggered by the propagating reaction fronts. The temporal evolution of the surface reaction results in a patterned surface consisting of separated Au-rich and Au-poor phases with different oxygen coverage, Rh surface structure, and reactivity. The experimental results are complemented by ab initio electronic structure calculations of the O and Au adsorption phases, which demonstrate that the reorganisation of the Au adlayer by the propagating reaction fronts is an energetically driven process. Our findings suggest that reaction-induced spatial inhomogeneity in the surface composition and structure is a common feature of metal catalysts modified with adatoms which become mobile under reaction conditions.

Chapter 7

Conclusions

The last few years have seen an intense development of new methods aimed at the study of rare events. Some of them are specifically suited to study systems characterised by a smooth potential energy surface, where the identification of the saddle point separating stable states is sufficient to achieve a good estimate of the transition rate. Among these methods the nudged elastic band [3] and of the string method [4] have received a particular attention because their moderate computational cost make them well suited to be used in conjunction with first-principles methods. Other approaches, as the transition-path sampling or the metadynamics, are more ambitious because they are designed to cope with the difficulties introduced by a rugged potential energy surface, taking into account the important entropic effects that arise at finite temperature. The price to pay for such generality is an extremely high computational cost for the transition-path sampling or the need to identify a coarse-grained space of reduced dimensionality for the metadynamics.

The research I have performed is focused on the first class of methods. The choice is motivated by the requirement of having at our disposal an efficient tool for the *ab initio* study of the activated processes that occur in solid-state systems, such as diffusion and chemical reactivity at crystal surfaces. The PES of these systems is rather smooth and characterised by a small number of relevant minima and saddle points. Moreover a reliable description of the entropic effects that, at finite temperature, can be important to determine the relative stability of different configurations can be obtained in the harmonic approximation. For this reasons, the minimum energy path provides good indications on the reaction mechanism and the saddle point contains most of the information required to evaluate the transition rate.

In this thesis I have described my original implementation of the nudged elastic band and of the string methods within the framework of *ab initio*

calculations. In principle these methods should have a computational cost comparable to that of a set of constrained minimisations (one for each image). In practice the situation is less rosy and their performance strongly depends on the number of images required to describe the reaction pathway. For this reason, I have devoted a particular effort to the study of algorithms that allow for an accurate description of the MEP, requiring the minimum number of images. The experience accumulated during this work has permitted the development of powerful optimisation schemes, sophisticated parallelisation approaches and user-friendly interfaces that make the identification of MEPs a rather straightforward task. This implementation is now part of the open-source Quantum-ESPRESSO project [17]. These methods are thus freely available to the scientific community and are currently employed worldwide for the study of a variety of different processes. These computational tools have been used by the author for the investigation of several surface phenomena. The applications range from the study of chemisorption of organic molecules at the semiconductors' surfaces to the description of the deconstruction process of transition metal surfaces. Particularly successful has been the application of this method to the investigation of the simple chemical reactions involved in the catalytic transformation of methane at the transition-metal surfaces.

No doubt my forthcoming research will encompass more complex systems, where entropic effects are fundamental to determine the reaction rate. In these cases the investigation of the kinetics requires, not just the knowledge of the energy barrier, but the computation of the free-energy profile for the reaction. This can be obtained using the MEP, identified by means of the NEB or the string methods, as a reaction coordinate and performing an umbrella sampling of the equilibrium distribution of the system on the hyperplanes orthogonal to the MEP [4]. However, the NEB method is of limited utility whenever the potential energy surface is rugged and dense of many possible reaction paths. This because the single MEP is no longer a good indicator of the reaction mechanism and a whole ensemble of reaction paths must be considered. For instance, chemical reactions in solution cannot be described using the same reaction coordinate used in the gas-phase, because the solvent plays, in many cases, an active role. In such systems the identification of a reliable reaction coordinate, that could take into account all the degrees of freedom, constitutes the first issue. Recently, Ren and E [14] have proposed a generalisation of the string method described in this thesis that, taking into account the thermal effects on the dynamics of the string, is able to smear the corrugation of the PES on the energy scale of $K_B T$. In this method, referred to as *finite-temperature string method*, each image of the string performs a sampling of the equilibrium distribution of the

system constrained on the hyperplane defined by the tangent to the string. The string is updated self-consistently until it approximates locally the correct reaction coordinate associated with the reaction process. The region in these planes where the equilibrium distribution is concentrated determines a transition tube in the configuration space in which reaction takes place with high probability. The method is particularly appealing because it allows for the identification of an effective reaction pathway with minimum requirement of a prior knowledge (mostly the location of the stable states is required). A variant of this method, based on the Fourier representation of the string discussed in this thesis, has been implemented by the author and tested on the two-dimensional Mueller PES. The preliminary results obtained on this toy model are encouraging because it seems possible to estimate the free-energy profile discretising the string with only few images. However it is not yet clear what the computational cost of this approach might be when applied to systems of practical interest, where the PES is enormously more complex.

Appendix A

Computational tools

The *ab initio* simulations presented in this thesis have been performed within Density Functional Theory, using the plane-wave pseudo-potential method, as implemented in the PWscf package [50]. For the exchange-correlation functional I have used the generalised gradient approximation (GGA) in the form proposed by Perdew Burke and Ernzerhof (PBE) [51] since it is typically more accurate than the local density functional in describing surface chemical processes. However, as happens for other gradient corrected exchange-correlation functionals, the weak interactions that are typical of van der Waals forces are poorly described. The surfaces have been modelled using periodically repeated slabs separated by a vacuum region of at least 10 Å (see Figure A.1). The bottom layers have been kept fixed in the bulk truncated structure and, in the case of insulating surfaces, the bottom-layer dangling bonds have been saturated with hydrogen atoms. Ultrasoft [52] pseudo potentials have been used for the atomic species and the electronic states have been expanded in plane waves. Kinetic-energy and charge-density cut-offs are reported in Table A.1 and have been chosen to ensure that the structural properties of our systems are well converged. The resulting overall accuracy is estimated to be better than 10 meV for the binding energies and better than 100 meV for the activation energies. The larger error assumed for energy barriers is the consequence of the possibly poor description of the weak bonds occurring at the transition states. The electron density has been determined self-consistently by iterative diagonalisation of the Kohn-Sham Hamiltonian and by the modified charge-density Broyden's mixing for accelerating convergence of the self-consistent procedure [53]. The accuracy of the Hellmann-Feynman forces, which are rather dependent on the level of self-consistency, has been improved by using the correction proposed by Chan *et al.* [54]. Brillouin-zone integrations have been performed with the special points technique [55], whereas the Fermi surface effects have been

system	ψ cut-off	ρ cut-off
$C_2H_2@Si(111) - 7 \times 7$	25 Ry	150 Ry
$Rh(110)$ surface	24 Ry	192 Ry
$C@Ni(111)$	25 Ry	200 Ry

Table A.1: Kinetic-energy and charge-density cut-offs for the three different systems studied.

treated by the smearing technique of Methfexel and Paxton [56], using a smearing parameter of 0.136 eV. This approach has been used also in the case of insulating surfaces (as in the case of $Si(111) - 2 \times 2$) because, even when the ground state is known to be an insulator, this might not be true for the initial state of a structural optimisation or for the intermediate images of a reaction path. Structural optimisations have been performed using a quasi-Newton algorithm and a recently proposed variant of the well known BFGS scheme for the update of the inverse Hessian matrix [57]. After every optimisation step, the charge density—used to generate the initial guess for the Khon-Sham potential—and the trial wavefunctions—used in the iterative diagonalisation of the Khon-Sham Hamiltonian—are extrapolated from those obtained at the previous steps. For this purpose I have used the second-order scheme proposed by Arias *et al.* for the wavefunctions [58] and the scheme proposed by Alfé for the charge density [59]. For both structural relaxations and path optimisations it has been checked that, at convergence, the L_∞ norm of the force vector was smaller than 50 meV/Å. All the molecular graphics presented in this thesis have been produced with the XCRYSDEN graphical package [60].

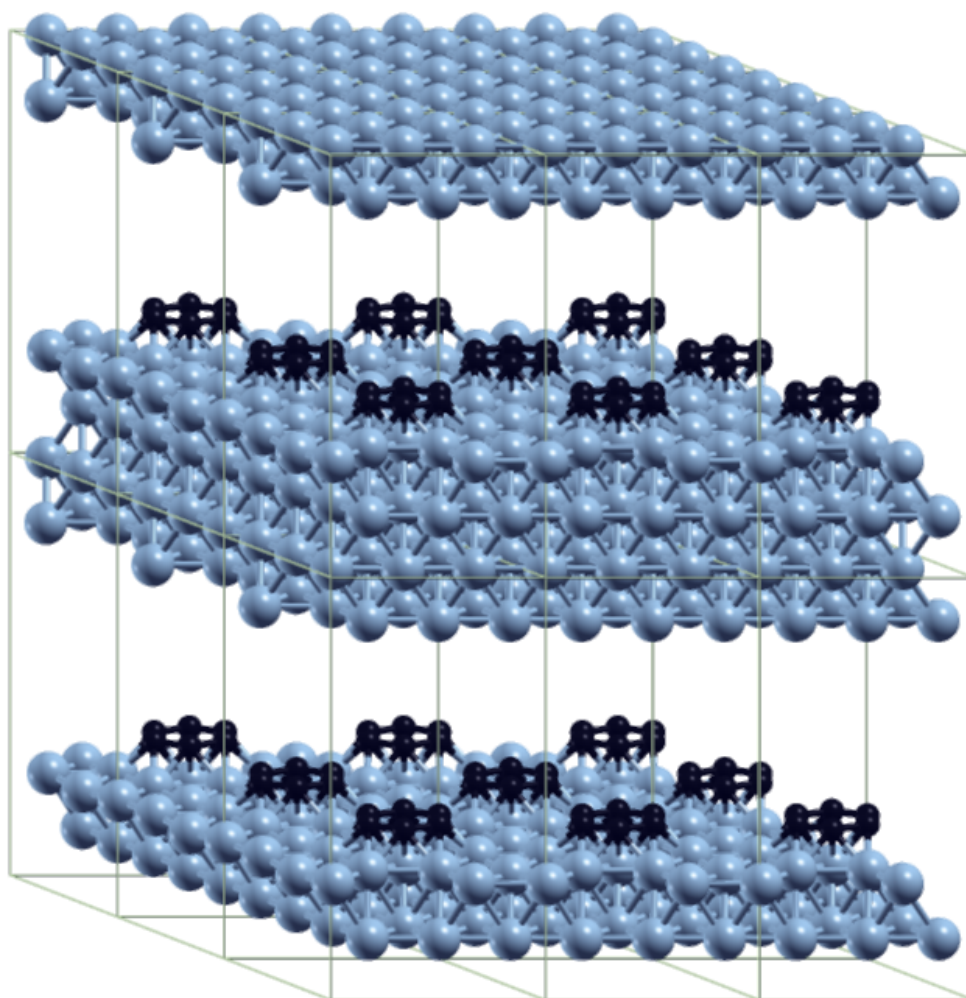


Figure A.1: Periodically repeated images of the supercell used for the calculations on the carbon adsorption at the Ni(111) surface.

Appendix B

Discrete Fourier Transform

Let's consider a one dimensional periodic function $f(x)$ defined on the interval $[0, L]$ and let's assume that $f(x)$ is sampled on a uniform mesh of N points:

$$\begin{aligned}\Delta x &= \frac{L}{N-1} \\ x_j &= j \Delta x \\ f(x) &\longrightarrow f(j \Delta x) = f_j \\ \frac{1}{L} \int_0^L f(x) dx &\longrightarrow \frac{1}{N} \sum_{j=0}^{N-1} f_j.\end{aligned}\tag{B.1}$$

In the following I adopt the convention of labelling real space indexes by j, k and reciprocal space indexes by n, m . On the discretised mesh the orthogonality between plane waves is given by the relation:

$$\sum_{j=0}^{N-1} e^{i \frac{2\pi}{N} (m-n)j} = N \delta_{n,m}\tag{B.2}$$

This is immediately verified by simple calculations:

$$\begin{aligned}\sum_{j=0}^{N-1} e^{i \frac{2\pi}{N} (m-n)j} &= \frac{e^{-i2\pi n} (e^{i2\pi m} - e^{i2\pi n})}{e^{-i \frac{2\pi}{N} (m-n)} - 1} \\ &= \frac{e^{i2\pi(m-n)} - 1}{e^{i \frac{2\pi}{N} (m-n)} - 1} \\ &= \frac{e^{i\pi(m-n)} 2i \sin(\pi(m-n))}{e^{i \frac{\pi}{N} (m-n)} 2i \sin(\frac{\pi}{N}(m-n))} \\ &= \begin{cases} 0 & \text{if } m \neq n \\ \frac{\sin(\pi(m-n))}{\sin(\frac{\pi}{N}(m-n))} = N & \text{if } m = n \end{cases}.\end{aligned}\tag{B.3}$$

Here I want to show that a one to one correspondence exists between the function f_j and its Fourier coefficients \tilde{f}_n :

$$\begin{aligned} f_j &= \sum_{n=0}^{N-1} \tilde{f}_n e^{i\frac{2\pi}{N}nj} \\ &\Updownarrow \\ \tilde{f}_n &= \frac{1}{N} \sum_{j=0}^{N-1} f_j e^{-i\frac{2\pi}{N}nj} \end{aligned} \quad (\text{B.4})$$

I first show that, assumed the function f_j can be written as:

$$f_j = \sum_{n=0}^{N-1} \tilde{f}_n e^{i\frac{2\pi}{N}nj} \quad (\text{B.5})$$

then its Fourier coefficients are given by:

$$\tilde{f}_n = \frac{1}{N} \sum_{j=0}^{N-1} f_j e^{-i\frac{2\pi}{N}nj} \quad (\text{B.6})$$

Indeed :

$$\begin{aligned} f_j &= \sum_{n=0}^{N-1} \tilde{f}_n e^{i\frac{2\pi}{N}nj} \\ &= \sum_{n=0}^{N-1} \left(\frac{1}{N} \sum_{k=0}^{N-1} f_k e^{-i\frac{2\pi}{N}nk} \right) e^{i\frac{2\pi}{N}nj} \\ &= \frac{1}{N} \sum_{k=0}^{N-1} f_k \sum_{n=0}^{N-1} e^{i\frac{2\pi}{N}n(j-k)} \\ &= \frac{1}{N} \sum_{k=0}^{N-1} f_k N \delta_{j,k} \\ &= f_j. \end{aligned} \quad (\text{B.7})$$

The other implication is shown with similar calculations:

$$\begin{aligned}\tilde{f}_n &= \frac{1}{N} \sum_{j=0}^{N-1} f_j e^{-i \frac{2\pi}{N} n j} \\ &= \frac{1}{N} \sum_{j=0}^{N-1} \left(\sum_{m=0}^{N-1} \tilde{f}_m e^{i \frac{2\pi}{N} m j} \right) e^{-i \frac{2\pi}{N} n j} \\ &= \frac{1}{N} \sum_{m=0}^{N-1} \tilde{f}_m \sum_{j=0}^{N-1} e^{i \frac{2\pi}{N} (n-m) j} \\ &= \frac{1}{N} \sum_{m=0}^{N-1} \tilde{f}_m N \delta_{n,m} \\ &= \tilde{f}_n.\end{aligned}\tag{B.8}$$

Bibliography

- [1] R. Car and M. Parrinello, Phys. Rev. Lett. **55**, 2471 (1985).
- [2] R. Elber and M. Karplus, Chem. Phys. Lett. **139**, 375 (1987).
- [3] H. Jónsson, G. Mills, and K. W. Jacobsen, in *Classical and Quantum Dynamics in Condensed Phase Simulations*, edited by B. J. Berne, G. Ciccotti, and D. F. Coker (World Scientific, Singapore, 1998), Chap. 16, pp. 385–404.
- [4] W. E, W. Ren, and E. Vanden-Eijnden, Phys. Rev. B **66**, 052301 (2002).
- [5] M. Sprik and G. Ciccotti, J. Chem. Phys. **109**, 7737 (1998).
- [6] C. Dellago, P. G. Bolhuis, F. S. Csajka, and D. Chandler, J. Chem. Phys. **108**, 1964 (1997).
- [7] D. Passerone and M. Parrinello, Phys. Rev. Lett. **87**, 108302 (2001).
- [8] A. Laio and M. Parrinello, Proc. Nat. Acad. Sci. U.S.A. **99**, 12562 (2002).
- [9] C. W. Gear, I. G. Kevrekidis, and C. Theodoropoulos, Comput. Chem. Eng. **6**, 941 (2002).
- [10] G. Henkelman, B. P. Uberuaga, and H. Jónsson, J. Chem. Phys. **113**, 9901 (2000).
- [11] G. Henkelman and H. Jónsson, J. Chem. Phys. **113**, 9978 (2000).
- [12] R. Zwanzig, Phys. Rev. **124**, 983 (1961).
- [13] H. Mori, Prog. Theor. Phys. **33**, 423 (1965).
- [14] W. Ren, Ph.D. thesis, New York University, 2002.

-
- [15] Y. Kanai, A. Tilocca, A. Selloni, and R. Car, *J. Chem. Phys.* **121**, 3359 (2004).
- [16] M. P. Allen and D. J. Tildesley, *Computer Simulation of Liquids* (Clarendon, Oxford, 1987).
- [17] Quantum-ESPRESSO (*Quantum opEn-Source Package for Research in Electronic Structure, Simulation, and Optimisation*) is an open-source project shipped by DEMOCRITOS (DEMOCRITOS MOdeling Center for Research In aTOMistic Simulations, <http://www.democritos.it>; see also <http://www.pwscf.org>) in collaboration with other institutions (CINECA Bologna, Princeton University, MIT) and distributed under the General Public License (GPL, <http://www.gnu.org/copyleft/gpl.txt>). Quantum-ESPRESSO is a collection of software for the computer modelling of matter based on electronic structure: it uses density-functional theory (DFT), a plane waves (PW) basis set, and pseudopotentials (PP). This distribution is the result of the merge of pre-existing packages and offers access to several techniques whose wide-spread use has traditionally been limited by the lack of available software (linear response, ultrasoft PP, Car-Parrinello Molecular Dynamics). The codes have been made homogeneous and modular in order to favour the easy addition of new packages, developments, extensions, and new features.
- [18] C. Sbraccia, <http://www.sissa.it/sbraccia/gNEB.d> (2003-2005).
- [19] J. Hutter *et al.*, CPMD Copyright IBM Corp. 1990-2003, Copyright MPI fur Festkorperforschung, Stuttgart, 1997-2001. See also <http://www.cpmd.org>.
- [20] C. Sbraccia, P. L. Silvestrelli, and F. Ancilotto, *Surf. Science* **516**, 147 (2002).
- [21] C. Sbraccia *et al.*, *Surf. Science* **557**, 80 (2004).
- [22] F. Rochet *et al.*, *Phys. Rev. B* **57**, 6738 (1998).
- [23] V. D. Renzi, R. Biagi, and U. del Pennino, *Phys. Rev. B* **64**, 155305 (2001).
- [24] X. Lu, X. Wang, Q. Yuan, and Q. Zhang, *J. Am. Chem. Soc.* **125**, 7923 (2003).

-
- [25] J. Yoshinobu, H. Tsuda, M. Onchi, and M. Nishijima, Chem. Phys. Lett. **130**, 170 (1986).
- [26] R. D. Felice *et al.*, Surf. Science **532**, 982 (2003).
- [27] K. D. Brommer, M. Needels, B. E. Larson, and J. Joannopoulos, Phys. Rev. Lett. **68**, 1355 (1992).
- [28] A. J. Dyson and P. W. Smith, Mol. Phys. **96**, 1491 (1999).
- [29] J.-Z. Que, M. Radny, P. Smith, and A. Dyson, Surf. Science **444**, 123 (2000).
- [30] R. Miotto, A. C. Ferraz, and G. P. Srivastava, Phys. Rev. B **65**, 75401 (2002).
- [31] P.-O. Löwdin, Phys. Rev. **97**, 1474 (1954).
- [32] G. Comelli *et al.*, Surf. Science Rep. **32**, 165 (1998).
- [33] D. Cvetko *et al.*, Surf. Science **318**, L1193 (1994).
- [34] C. Africh, F. Esch, G. Comelli, and R. Rosei, J. Chem. Phys. **116**, 7200 (2002).
- [35] R. V. Gastel *et al.*, Phys. Rev. Lett. **86**, 1562 (2001).
- [36] M. L. Grant, B. S. Swartzentruber, N. C. Bartelt, and J. Hannon, Phys. Rev. Lett. **86**, 4588 (2001).
- [37] G. L. Kellogg and P. J. Feibelman, Phys. Rev. Lett. **64**, 3143 (1990).
- [38] D. Alfé, Ph.D. thesis, SISSA, Scuola Internazionale Superiore di Studi Avanzati, 1997.
- [39] <http://www.webelements.com/>, The University of Sheffield and Webelements Ltd, UK.
- [40] A. Filippetti and V. Fiorentini, Phys. Rev. B **60**, 14366 (1999).
- [41] C. Klink and *et al.*, Surf. Science **342**, 250 (1995).
- [42] D. Alfé, S. de Gironcoli, and S. Baroni, Surf. Science **437**, 18 (1999).
- [43] H. Nakano, J. Ogawa, and J. Nakamura, Surf. Science **514**, 256 (2002).
- [44] F. Besenbacher *et al.*, Science **279**, 1913 (1998).

- [45] S. Helveg *et al.*, Nature **427**, 426 (2004).
- [46] P. Villars and L. Calvert, *Pearson's Handbook of Crystallographic Data for Intermetallic Phases* (ASM International, Materials Park, OH, 1991).
- [47] Landolt-Börnstein, in *Elastic, Piezoelectric, and Related Constants of Crystals*, edited by K.H.Hellwege and A.M.Hellwege (Springer-Verlag, New York, 1979), bulk moduli are computed using the relation $B_0 = (C_{11} + 2C_{12})/3$.
- [48] C. Kittel, *Introduction to Solid State Physics*, 7th edition ed. (John Wiley and Sons, New York, 1995).
- [49] J. F. Mojica and L. L. Levenson, Surf. Science **59**, 447 (1976).
- [50] S. Baroni, A. D. Corso, S. de Gironcoli, and P. Giannozzi, <http://www.pwscf.org>.
- [51] J. P. Perdew, K. Burke, and M. Ernzerhof, Phys. Rev. Lett. **77**, 3865 (1996).
- [52] D. Vanderbilt, Phys. Rev. B **41**, 7892 (1990).
- [53] D. D. Johnson, Phys. Rev. B **38**, 12807 (1988).
- [54] C. T. Chan, K. P. Bohnen, and K. M. Ho, Phys. Rev. B **47**, 4771 (1992).
- [55] H. J. Monkhorst and J. D. Pack, Phys. Rev. B **13**, 5188 (1976).
- [56] M. Methfessel and A. T. Paxton, Phys. Rev. B **40**, 3616 (1989).
- [57] S. R. Billeter, A. J. Turner, and W. Thiel, Phys. Chem. Chem. Phys. **2**, 2177 (2000).
- [58] T. A. Arias, M. C. Payne, and J. D. Joannopoulos, Phys. Rev. B **45**, 1538 (1992).
- [59] D. Alfé, Comput. Phys. Commun. **118**, 31 (1999).
- [60] A. Kokalj, XCrySDen: (X-window) CRYstalline Structures and DENsities, <http://www.xcrysden.org> (2003).

Acknowledgements

I am extremely grateful to Stefano Baroni for giving me the opportunity of working on very interesting and fascinating topics and for transmitting me his enthusiasm in the study of physics. My deepest gratitude goes also to Pier Luigi Silvestrelli and Francesco Ancilotto who have guided me since I was an undergraduate student, prosecuting a stimulating scientific collaboration. This experience would not have been possible without their support. I am grateful to all the members of the Condensed Matter sector at SISSA, for their teaching and for the stimulating environment they create. In particular, I would like to thank Dario Alfé, Andrea Dal Corso, Stefano de Gironcoli, and Tone Kokalj for the many scientific discussions and useful advises. Additional special thanks go to Nicola Bonini, who has shared with me most of the time spent at SISSA, and to Lorenzo Brualla, who has contaminated me with his endless knowledge and introduced to the fascinating world of the heavy-weather sailing. Finally, I would like to greet all my colleagues, all the friends I have met during this period in SISSA and, last but not least, thanks to *Valentina* ...